

## **Master thesis and internship[BR]- Master's thesis : Computational method for whirl-flutter analysis of urban air mobility vehicles[BR]- Internship**

**Auteur :** Jacquet, Charles

**Promoteur(s) :** Salles, Loïc

**Faculté :** Faculté des Sciences appliquées

**Diplôme :** Master en ingénieur civil en aérospatiale, à finalité spécialisée en "aerospace engineering"

**Année académique :** 2023-2024

**URI/URL :** <http://hdl.handle.net/2268.2/20851>

---

### *Avertissement à l'attention des usagers :*

*Tous les documents placés en accès ouvert sur le site le site MatheO sont protégés par le droit d'auteur. Conformément aux principes énoncés par la "Budapest Open Access Initiative"(BOAI, 2002), l'utilisateur du site peut lire, télécharger, copier, transmettre, imprimer, chercher ou faire un lien vers le texte intégral de ces documents, les disséquer pour les indexer, s'en servir de données pour un logiciel, ou s'en servir à toute autre fin légale (ou prévue par la réglementation relative au droit d'auteur). Toute utilisation du document à des fins commerciales est strictement interdite.*

*Par ailleurs, l'utilisateur s'engage à respecter les droits moraux de l'auteur, principalement le droit à l'intégrité de l'oeuvre et le droit de paternité et ce dans toute utilisation que l'utilisateur entreprend. Ainsi, à titre d'exemple, lorsqu'il reproduira un document par extrait ou dans son intégralité, l'utilisateur citera de manière complète les sources telles que mentionnées ci-dessus. Toute utilisation non explicitement autorisée ci-avant (telle que par exemple, la modification du document ou son résumé) nécessite l'autorisation préalable et expresse des auteurs ou de leurs ayants droit.*

---

---

# Computational method for whirl-flutter analysis of urban air mobility vehicles

---

*Master's thesis submitted by*

**Charles Jacquet**

*in order to obtain the degree of  
Master of Science in Aerospace Engineering*

**Supervisor: Loïc Salles**

**Academic year 2023–2024**



**University of Liège  
Faculty of Applied  
Sciences**



This thesis examines the whirl-flutter phenomenon in urban air mobility vehicles, crucial for the safety and efficiency of next-generation aircraft. The rise of Electric Vertical Take-Off and Landing (E-VTOL) vehicles, driven by the demand for fast urban transport, emphasizes the need to understand and mitigate aeroelastic instabilities like whirl-flutter, particularly in designs with distributed electric propulsion systems. Historically, whirl-flutter has caused catastrophic failures, highlighting the need for comprehensive analysis in modern aircraft designs.

The objective of this work is to develop a comprehensive computational model using the Finite Element Method to fully capture the dynamics between rotating, expressed in a floating frame of reference, and stationary parts of a structure, enabling a more accurate study of the whirl-flutter phenomenon. This analysis is conducted using the Floquet theory to study the stability of the system, particularly in a fixed-rotating frame of reference. The model includes an innovative time dependent mechanical coupling strategy for the mass, gyroscopic, and centrifugal stiffness structural matrices therefore fully preserving the dynamics of the structure, a first in the literature.

The research methodology involves the validation of various finite element matrices and components derived from Euler-Bernoulli 3D beam elements, followed by the implementation of time-dependent coupling between rotating and stationary components. This coupling is validated through case studies, including a ground resonance model and a rotating shaft with blades. Finally, the developed model is applied to a wing-propeller structure, illustrating its capability to work on complex geometry structures.

The results show that the partial coupling, specifically the coupling between translational degrees of freedom of rotating structures and those of stationary structure at the hub, is successfully validated. However, it is demonstrated that the Newmark integration scheme does not provide consistent results, highlighting the need for alternative approaches such as Runge-Kutta scheme for accurate time integration. Although the full coupling is not entirely validated, the initial results suggest that the implementation is correctly performed and shows promise for future validation efforts. This partial success demonstrates the potential of the developed model as a tool for accurately capturing critical dynamics in whirl-flutter analysis, contributing to the design and certification of future urban air mobility vehicles.

**Keywords:** Floquet Theory, whirl-flutter, validation model, rotating structure, rotating/stationary time coupling, finite element modeling, floating frame of reference, Newmark, Runge-Kutta.





Cette thèse explore le phénomène de flottement gyroscopique dans les véhicules de mobilité aérienne urbaine, essentiel pour la sécurité des aéronefs de nouvelle génération. Avec l'essor des véhicules à décollage et atterrissage verticaux électriques, il devient crucial de comprendre et de contrôler les instabilités aéroélastiques telles que le flottement gyroscopique, particulièrement dans les conceptions utilisant des systèmes de propulsion électrique distribuée.

L'objectif de ce travail est de développer un modèle computationnel complet utilisant la méthode des éléments finis pour capturer entièrement les dynamiques entre les parties rotatives, exprimées dans un repère flottant, et les parties stationnaires d'une structure, permettant ainsi une étude plus précise du phénomène de flottement gyroscopique. Cette analyse est réalisée en utilisant la théorie de Floquet pour étudier la stabilité du système, en particulier dans un repère fixe-rotatif. Le modèle inclut une stratégie novatrice de couplage mécanique dépendant du temps pour les matrices structurelles de masse, gyroscopique et de raideur centrifuge, préservant ainsi pleinement les dynamiques de la structure, une première dans la littérature.

La méthodologie de recherche implique la validation de diverses matrices et composants d'éléments finis dérivés des éléments de poutre 3D d'Euler-Bernoulli, suivie par la mise en œuvre du couplage dépendant du temps entre les composants rotatifs et stationnaires. Ce couplage est validé à travers des études de cas, incluant un modèle de résonance de sol et un arbre rotatif avec des pales. Enfin, le modèle développé est appliqué à une structure aile-moteur à hélices, illustrant sa capacité à travailler sur des structures de géométrie complexe.

Les résultats montrent que le couplage partiel, en particulier le couplage entre les degrés de liberté de translation des structures rotatives et ceux des structures stationnaires au hub, est validé avec succès. Cependant, il est démontré que le schéma d'intégration de Newmark ne fournit pas de résultats cohérents, soulignant la nécessité d'approches alternatives telles que le schéma d'intégration de Runge-Kutta pour une intégration temporelle précise. Bien que le couplage complet ne soit pas entièrement validé, les résultats initiaux suggèrent que la mise en œuvre est correctement réalisée et montre un potentiel pour les futurs efforts de validation. Ce succès partiel démontre le potentiel du modèle développé en tant qu'outil pour capturer avec précision les dynamiques critiques dans l'analyse du flottement gyroscopique, contribuant à la conception et à la certification des futurs véhicules de mobilité aérienne urbaine.

**Mots-clés :** Théorie de Floquet, flottement gyroscopique, modèle de validation, structure rotative, couplage temporel rotatif/stationnaire, modélisation par éléments finis, repère flottant, Newmark, Runge-Kutta.



## ACKNOWLEDGMENTS

First of all, I would like to thanks Professor Loïc Salles, my supervisor, for giving me the opportunity to work on this subject, for his guidance through our meetings, the numerous hours helping me debug my code, and for taking the time to review this work.

I am also very grateful to all the members of the Aerospace and Mechanics department at the University of Liège who were able to contribute to this thesis by giving me feedback and support on some of the problems I encountered.

I would like to thank Colette and Mario, with whom I was able to share my office during the preparation of this work, for all the enriching moments we spent together and for your ongoing support.

I also wanted to thank all my friends that I was able to meet during my academic journey, without them I would never have become the person I have become. I would particularly like to thank Jeanne for her valuable help and constructive feedback during the proofreading of this manuscript.

I would also like to thank my girlfriend, Clotilde, for all her support during this work.

Finally, I wanted to thank my family and especially my parents and my sister. Their unconditional support and encouragement have been invaluable throughout my studies.



<b>List of Figures</b>	<b>iii</b>
<b>List of Tables</b>	<b>vii</b>
<b>List of acronyms</b>	<b>ix</b>
<b>Introduction</b>	<b>1</b>
<b>1 Stability Analysis</b>	<b>11</b>
1.1 Stability of linear time invariant system . . . . .	11
1.2 Coleman Transformation . . . . .	12
1.3 Floquet Theory - Stability analysis of linear time periodic system . . . . .	13
1.3.1 Mathematical derivation . . . . .	13
1.4 Numerical integration schemes . . . . .	16
1.4.1 Newmark time integration scheme . . . . .	16
1.4.1.1 Mathematical derivation of the monodromy matrix for Newmark integration scheme . . . . .	17
1.4.2 Generalised $\alpha$ scheme . . . . .	17
1.4.2.1 Mathematical derivation of the monodromy matrix for the Generalised $\alpha$ scheme . . . . .	18
1.4.3 Runge-Kutta integration scheme . . . . .	19
1.4.3.1 Derivation of the monodromy matrix . . . . .	19
1.5 Campbell diagram and the advantage of the periodic Campbell diagram . .	20
<b>2 Finite Element of Rotating Structure</b>	<b>23</b>
2.1 Finite element selection . . . . .	23
2.1.1 Validation of the centrifugal force . . . . .	26
2.1.2 Analytical model validation . . . . .	27
2.1.2.1 Eigenfrequencies computation and Campbell diagram . . .	28
2.2 Single clamped beam . . . . .	30
2.2.1 Validation of the model . . . . .	31
2.3 Conclusion . . . . .	32
<b>3 Coupling Between Stationary and Rotating parts</b>	<b>33</b>

3.1	Preamble . . . . .	33
3.2	Theoretical and mathematical background . . . . .	33
3.2.1	Full coupling of stationary and rotating parts . . . . .	33
3.2.1.1	Mathematical properties of the transformation matrix $H$ . . . . .	35
3.2.2	Finite element coupling of stationary and rotating parts . . . . .	36
3.2.2.1	Potential energy . . . . .	37
3.2.3	Kinetic energy . . . . .	38
3.2.3.1	Lagrange equation of motion . . . . .	39
3.3	Numerical implementation of the coupling between stationary and rotating parts . . . . .	39
3.3.1	General considerations . . . . .	39
3.3.2	Time coupling implementation and assembly strategy . . . . .	40
3.4	Validation of the coupling . . . . .	41
3.4.1	Coupling validation model: Ground resonance model . . . . .	42
3.4.1.1	Rigid model . . . . .	43
3.4.1.2	Validation of the different numerical schemes . . . . .	44
3.4.1.3	Finite element model . . . . .	47
3.4.2	Coupling validation model: Rotating shaft . . . . .	52
3.4.3	Unbalanced force validation . . . . .	55
3.5	Conclusion . . . . .	56
<b>4</b>	<b>Test Case of a wing propeller system</b>	<b>57</b>
4.1	Standalone wing . . . . .	57
4.1.0.1	Eigenfrequencies computation of the undamped wing . . . . .	58
4.1.1	Wing aerodynamics . . . . .	58
4.1.1.1	Theodorsen's theory . . . . .	58
4.1.1.2	Strip theory . . . . .	59
4.1.2	Flutter speed computation . . . . .	60
4.2	Propeller Aerodynamics . . . . .	61
4.3	Application to an aerospace structure . . . . .	62
4.4	Conclusion . . . . .	64
	<b>Conclusions and perspectives</b>	<b>65</b>
	<b>A Elementary Mass Matrix</b>	<b>69</b>
	<b>B Shape function matrix</b>	<b>71</b>
	<b>C Elementary stiffness matrix</b>	<b>73</b>
	<b>D Newmark Integration scheme</b>	<b>75</b>
	<b>E Gauss Legendre integration</b>	<b>77</b>
	<b>F Structural coupling between hub and rotating components</b>	<b>79</b>
	<b>Bibliography</b>	<b>81</b>

## LIST OF FIGURES

1	E-VTOL Midnight tilt-rotor configuration manufactured by Archer [6].	2
2	CityAirbus NextGen manufactured by Airbus [7]. . . . .	2
3	Lockheed Martin Electra 188 wind tunnel testing on a reduced size model [12]. . . . .	2
4	CFM Rise engine concept [14]. . . . .	3
5	Natural vibration modes of system with rigid propeller [18]. . . . .	4
6	Basic whirl-flutter model. Taken from [20]. . . . .	5
7	Whirl flutter boundary and dependencies on wing motion given in the literature [27]. . . . .	6
1.1	Complex-plane. Positions of the eigenvalue represented by different asterisks *. * - eigenvalue leading to a periodic stable system, * - eigenvalue leading to an asymptotically periodic stable system, * - eigenvalue leading to an unstable system, Unit circle. . . . .	15
1.2	Campbell diagram with LTI approximation. Reproduced from [45]. . .	20
1.3	Campbell diagram with Coleman transformation. Reproduced from [45].	20
1.4	Campbell diagram using LTP method. Reproduced from [45]. . . . .	21
2.1	Euler-Bernoulli beam element constitute of two nodes, each node containing 3 translational degrees of freedom and 3 rotational degrees of freedom. . . . .	23
2.2	Axial displacement $u_X$ in global frame of reference. The beam is directed along the direction vector $[1 \ 1 \ 1]$ with a rotation speed vector $\mathbf{\Omega} = [\Omega \ 0 \ -\Omega]$ with $\Omega = 3000$ rad/s. $u_X$ is the displacement along the X direction in the global frame of reference. . . . .	27
2.3	Axial displacement $u_X$ in a global frame of reference taking into account $K$ and $K_g$ . The beam is directed along the direction vector $[1 \ 1 \ 1]$ with a rotation speed vector $\mathbf{\Omega} = [\Omega \ 0 \ -\Omega]$ with $\Omega = 3000$ rad/s. $u_X$ being the displacement along the X direction in the global frame of reference.	28
2.4	Validation model: single clamped rotating beam. . . . .	29
2.5	Campbell diagram using Ansys model. . . . .	29
2.6	Campbell diagram using MATLAB model. . . . .	29
2.7	Validation model: single cantilever beam. . . . .	30



2.8	Out of plane mode of deformation. From left to right: first mode, third mode, and fifth mode of deformation. . . . .	31
3.1	Schematic of the full coupled stationary and rotating parts. Reproduced from [61]. . . . .	34
3.2	Schematic of the implementation to derive the equation of motion. Partially reproduced from Zuo et al [39]. . . . .	40
3.3	Representation of a structural matrix undergoing time coupling between the rotating structure and the hub. The different rows and columns (not represented) of the matrix represents the different degrees of freedom of the complete structure. . . . .	41
3.4	Validation case: Ground resonance model. Reproduced from Hammond et al [62]. . . . .	42
3.5	Relative modal damping ratio obtained using Newmark integration scheme using rigid model. . . . .	44
3.6	Relative modal damping ratio obtained using Runge-Kutta integration scheme using rigid model. . . . .	44
3.7	Relative modal damping ratio obtained using Newmark V2 integration scheme using rigid model. . . . .	44
3.8	Relative modal damping ratio obtained using $\alpha$ generalised integration scheme using rigid model. . . . .	44
3.9	Hub displacement over one period of revolution when rotor rotating at $\Omega = 3$ rad/s. . . . .	46
3.10	Hub displacement over ten periods of revolution when rotor rotating at $\Omega = 3$ rad/s . . . . .	46
3.11	Hub displacement over one period of revolution when rotor rotating at $\Omega = 30$ rad/s. . . . .	46
3.12	Hub displacement over ten periods of revolution when rotor rotating at $\Omega = 30$ rad/s . . . . .	46
3.13	Relative modal damping ratio obtained using Newmark integration scheme using rigid model with dampers acting on the hub and on the different blades. . . . .	47
3.14	Relative modal damping ratio obtained using Runge-Kutta integration scheme using rigid model with dampers acting on the hub and on the different blades. . . . .	47
3.15	Displacement of the hub in the $X$ direction for an initial displacement of 1m on the hub in the $X$ direction. Comparison between the Newmark integration scheme and Runge-Kutta integration scheme. . . . .	47
3.16	Relative modal damping for the undamped case using Newmark integration scheme. . . . .	49
3.17	Relative modal damping for the undamped case using the Runge-Kutta integration scheme. . . . .	49
3.18	Relative modal damping for the damped case using Newmark integration scheme. . . . .	49
3.19	Relative modal damping for the damped case using the Runge-Kutta integration scheme. . . . .	49

3.20	Evolution of the imaginary part of $\Gamma$ as a function of the rotor speed for the damped case using the rigid model. . . . .	50
3.21	Evolution of the imaginary part of $\Gamma$ as a function of the rotor speed for the damped case using the finite element model. . . . .	50
3.22	Relative error analysis using Runge-Kutta integration scheme for the undamped. Comparing the displacement in the $Y$ direction at the tip of blade n°1 at $\Omega = 27$ rad/s. . . . .	51
3.23	Relative error analysis using Runge-Kutta integration scheme for the undamped case. Comparing the displacement in the $Y$ direction at the tip of blade n°1 at $\Omega = 27$ rad/s for different relative error. . . . .	51
3.24	CPU time for the computation of the undamped case using Runge-Kutta integrartion scheme. . . . .	51
3.25	Displacement of the first blade after a unit initial displacement on the hub along $X$ direction for an undamped system. Comparison between different discretisation of the time interval. . . . .	52
3.26	Displacement of the first blade after a unit initial displacement on the hub along $X$ direction for a damped system. Comparison between different discretisation of the time interval. . . . .	52
3.27	Schematic of the rotating shaft. Left side - side view. Right side - front view. . . . .	52
3.28	Evolution of the modal damping with respect to the rotation speed of the shaft. . . . .	54
3.29	Evolution of the imaginary part of $\Gamma$ as a function of the rotor speed of the shaft. . . . .	54
3.30	Unbalanced force along $X$ direction. Comparison between analytical solution and finite element solution. . . . .	56
3.31	Unbalanced force along $Y$ direction. Comparison between analytical solution and finite element solution. . . . .	56
4.1	Wing Propeller structure. Propeller being flexibly attached to the wing via springs and dampers in pitch and yaw direction. Partially reproduced from [27]. . . . .	62
4.2	Evolution of the relative modal damping ratio with respect to the rotation speed of the propeller. . . . .	64
4.3	Evolution of the imaginary part of $\Gamma$ as a function of the rotor speed of the propeller. . . . .	64
D.1	Flowchart of the Newmark integration scheme for linear systems. Taken from [47]. . . . .	75



## LIST OF TABLES

2.1	Comparison of MATLAB and ANSYS results for different rotation speeds. BW = backward whirl and FW = forward whirl. . . . .	29
2.2	Material properties and geometrical properties of the constituting beam. . .	31
2.3	First six natural frequencies obtained using MATLAB with 10 elements discretising the beam, and comparison with the analytical model. Relative error computed assuming analytical solution frequency being the reference. . . . .	31
3.1	Ground resonance model parameters (Hammond et al [62]). . . . .	43
3.2	Ground resonance equivalent model parameters for finite element formulation of the problem. . . . .	48
3.3	Rotating shaft model parameters. . . . .	53
3.4	ANSYS results for different rotation speeds. BW = backward whirl, FW = forward whirl. . . . .	55
4.1	Mechanical Properties of the Goland wing. . . . .	57
4.2	First six natural frequencies obtained on MATLAB with 20 elements discretising the beam. Comparison with the FEM model developed by Akpınar [66]. Relative error computed assuming FEM model of Akpınar being the reference. . . . .	58
4.3	Mechanical properties of the wing. . . . .	63
4.4	Mechanical properties related to Pitch and Yaw Axes of the propeller. The position of the rotor CG and motor CG are expressed from the wing CG. . .	63
4.5	Inertial and structural properties of the propeller. . . . .	63
E.1	Roots and weights of nth Legendre polynomials for $n = 2, 3, 4$ and $5$ . . . .	78



## LIST OF ACRONYMS

CFD	Computational fluid dynamics
DEP	Distributed electrical propulsion
DLM	Doublet lattice method
E-VTOL	Electric vertical and take-off landing
FEM	Finite element method
LTI	Linear time invariant
LTP	Linear time periodic
MAC	Modal assurance criterion
RANS	Reynolds averaged Navier-Stokes
URANS	Unsteady Reynolds averaged Navier-Stokes
TDT	Transonic Dynamic Tunnel



## Context and motivation

Urban air mobility vehicles are emerging types of air transport systems used in cities and their surroundings in order to transport people or cargo. Urban air mobility vehicles experiment new types of aircraft design in the aim of transporting safely people in metropolitan areas [1]. This new type of means of transportation is often presented as capable of quickly responding to medical emergencies or to being able to reduce urban traffic congestion. However, a study made by McKinsey & Company [2] concludes that urban air mobility vehicles cannot be considered, nowadays, as a valid option to reduce traffic congestion in urban areas due to the expected high cost of operations of such solutions at the beginning of its operating life and the difficulties of providing door-to-door transport in most urban areas. These difficulties can be although overcome in certain megalopolises such as New York and Paris. Recently, the French government won its battle with the Paris City Council over the use of urban taxis during the 2024 Olympic Games [3]. The courts have authorized a maximum of 900 hours of urban taxi flights in the French capital until the end of the year 2024. The purpose of these 900 flight hours will be to demonstrate the ability to use urban taxis as a means of transport in a major city. Three different routes have been approved. These will be used to link the French capital with various airports on the outskirts of the city.

This new type of aircraft features innovative structures and complex levels of flight automation. These new features make civil certification of these aircraft even more complex [4]. In fact, most companies that offer such types of aircraft aim to market aircraft using Electrical Vertical take-off and landing (E-VTOL) technology (Figure 1). Major players in the industry, some of whom have been around for decades, such as Airbus with its CityAirbus NextGen (Figure 2), are developing urban air mobility aircraft. However, there are also new companies taking up the challenge of developing new types of aircraft that have never been designed and certified before, as is the case with Archer, which is currently developing and certifying its Midnight aircraft [5].



## INTRODUCTION



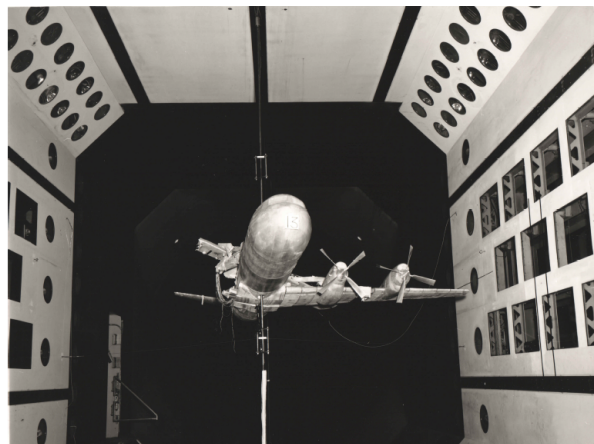
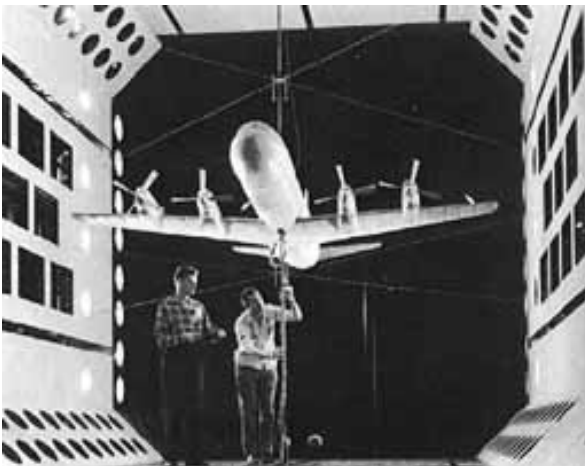
FIGURE 1 – E-VTOL Midnight tilt-rotor configuration manufactured by Archer [6].



FIGURE 2 – CityAirbus NextGen manufactured by Airbus [7].

Most of the current proposed configurations suggest the usage of tilt-rotor configuration or tilt wing-rotor configuration. The usage of electrical motors authorizes the exploitation of a distributed electrical propulsion (DEP) system, which involves the use of multiple rotors, each of them connected to an electrical motor [8]. Tilt-rotor configuration alters the rotor configuration to perform vertical take-off and landing along with forward flight [9]. This extra degree of freedom, along with a large-diameter rotor, can expose the structure of the aircraft to the widely recognized phenomenon known as whirl flutter [10].

First mathematically discovered in 1938 by Browne and Taylor [11], whirl flutter is an instability that occurs when the rotor aerodynamic loads couples with wing flexibility from the wing mounted pylon during the flight of propeller-driven aircraft. This phenomenon tended to be forgotten in the design process of aircraft until 1960 when two Electra aircraft manufactured by Lockheed Martin crashed. After those tragic events, tests were conducted, in the Nasa's Transonic Dynamic Tunnel (TDT), on a reduced model (Figure 3).



(a) Lockheed Electra 188 model in TDT before test. (b) Lockheed Electra 188 model in TDT after test.

FIGURE 3 – Lockheed Martin Electra 188 wind tunnel testing on a reduced size model [12].

It was then demonstrated that the failure of the aircraft was due to a damaged pylon mount weakening the aircraft allowing whirl flutter to occur, then leading to the failure of

the entire aircraft [13].

More recently, with the current development of the new generation of engines to power aircraft in 2040 horizon, the CFM consortium, which is a joint venture between the US company GE Aerospace and the French engine manufacturer Safran Aircraft Engines, is currently developing a new engine called CFM RISE (Figure 4 ).



FIGURE 4 – CFM Rise engine concept [14].

This engine aims to achieve a technological breakthrough and is in no way similar to its predecessor's turbofan engine. It should be noted that this type of engine is composed of an unshrouded fan, which leaves room for the phenomenon of whirl flutter to take place if the design of the aircraft on which it is placed is poorly carried out. This once again demonstrates the importance of studying the whirl-flutter phenomenon.

Despite its importance in aeronautics, the whirl flutter phenomenon is also important in the energy sector. With the energy transition underway worldwide, fuelled by a global desire to reduce CO<sub>2</sub> emissions, both onshore and offshore wind turbines are a major solution for reducing carbon emissions from power generation. The European Union (EU) has issued an action plan aimed at reducing carbon emissions by 55% compared with 2005 levels by 2030, intending to achieve carbon neutrality by 2050 [15]. In 2020, the energy production sector accounted for 42% of CO<sub>2</sub> emissions worldwide [16]. The use of renewable means of production is therefore a solution for reducing this number in the future. To meet the EU's reduction target, many countries have opted to step up the deployment of renewable energy production plants on land or at sea, in particular by using wind turbines and wind farms [17]. Wind turbines therefore need to be designed to meet safety standards, but also to maximize their energy output and operating range of operation. To achieve this, it is important to identify the critical rotation speed and wind speeds that initiate the whirl flutter phenomenon.

## State of the art

Propeller whirl flutter was firstly discovered in 1938 by Browne and Taylor [11]. The study conducted detailed the interaction of vibrations coming mainly from the engine and elastic mounting measures to reduce the vibratory loads on the accessory equipment surrounding the engine. The model used to prove the concept used a reduced friction model as well

## INTRODUCTION

as an equal ratio of pylon stiffness ratio in the pitch and yaw degree of freedom. At this time in history, aircraft were not in danger to meet such instability because the stiffness of the pylon was such that any loading on it would not cause any problem of instability. However, with the emergence of new engines and aircraft structures, the aim has always been to be lighter and lighter. Two plane crashes in the early 1960s forced scientists to reconsider the discoveries made by Brown and Taylor. As a result, whirl flutter has emerged as a phenomenon to be taken into account when designing new aircraft and certifying them.

Figure 5 highlights the two types of possible whirl-flutter instabilities, respectively the backward whirl-flutter and the forward whirl flutter. The backward whirl flutter corresponds to instability causing the blade to move in the opposite direction of the flight direction whereas the forward whirl flutter corresponds to instability causing the blade to move in the direction of rotation.

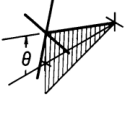
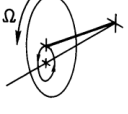
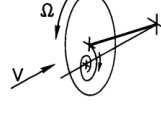
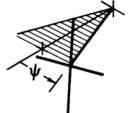
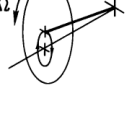
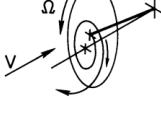
NONROTATING PROP.	ROTATING PROP. WITHOUT AIR FORCES	TRANSIENT RESPONSE WITH AIR FORCES
<p>PITCH</p> 	<p>FORWARD WHIRL</p> 	<p>STABLE (<math>V &lt; V_{CRIT.}</math>)</p> 
<p>YAW</p> 	<p>BACKWARD WHIRL</p> 	<p>UNSTABLE (<math>V &gt; V_{CRIT.}</math>)</p> 

FIGURE 5 – Natural vibration modes of system with rigid propeller [18].

A study published in 1962 by Hublot and Reed [19] identified the key parameter influencing whirl flutter instability to occur. They identified these parameters as being a combination of pitch and yaw stiffness of the nacelle, structural damping, and propeller speed. The propeller used in this study had equal pylon stiffness in the yaw and pitch directions. A study conducted by Reed [12] highlights that a system using an equal stiffness in yaw and pitch directions is a worse scenario for propeller whirl than if the stiffness in one direction is different from the one in another direction. Having an equal stiffness in both directions makes the system more prone to flutter.

The model originally presented by Reed [18] (Figure 6) is a basic model that consists of a propeller that is modeled using two degrees of freedom. The propeller consists of a rotor of radius  $R$ , rotating at an angular velocity  $\Omega$ , with a moment of inertia  $I_x$  about its rotational axis. This rotor is allowed to move around a pivot point in pitch and yaw. The pivot point is represented by a moment of inertia  $I_n$ . The equations of motion characterizing the presented model reads

$$\begin{aligned}
 I_n \ddot{\theta} + c_\theta \dot{\theta} - I_x \Omega \dot{\psi} + K_\theta \theta &= M_\theta; \\
 I_n \ddot{\psi} + c_\psi \dot{\psi} + I_x \Omega \dot{\theta} + K_\psi \psi &= M_\psi,
 \end{aligned}$$

where  $c_\theta$  and  $c_\psi$  corresponds respectively to the structural damping in the related direction,  $K_\theta$  and  $K_\psi$  to the stiffness in their relative direction,  $M_\theta$  and  $M_\psi$  to the aerodynamic moment acting on the system.

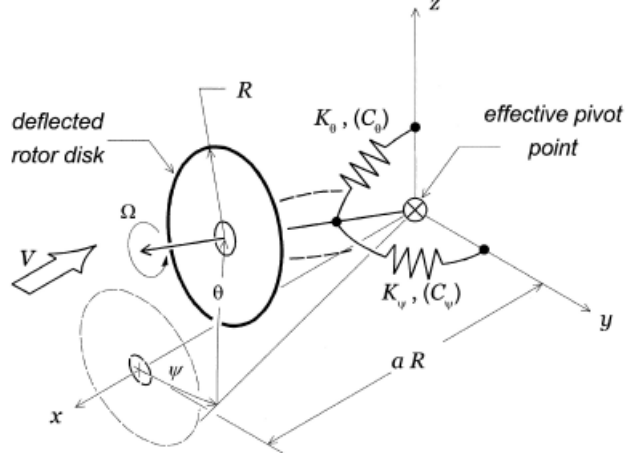


FIGURE 6 – Basic whirl-flutter model. Taken from [20].

Aerodynamic instability has long been studied whether for individual aircraft parts or coupled systems parts. A well-known aerodynamic instability is wing flutter [21] which is also called classical flutter. Wing flutter is usually modelled using a flexible wing coupled with an unsteady aerodynamic model such as Doublet Lattice Method (DLM) for example. A study conducted by Strong et al.[22] explores how prestressed mode shapes and frequencies affect wing flutter response calculations. The research suggests prestressing impacts the dynamic aeroelastic response, especially in configurations prone to body freedom flutter, like high aspect ratio blended wing body configurations.

Propeller whirl-flutter theory was first developed for a propeller attached to its pylon assuming that propeller blades were rigid and could not deform under any type of load (gravitational, aerodynamics, ...) [19]. Hoover and Shen [23] studied the whirl flutter phenomenon in free flying condition of the X-57 aircraft developed by NASA. Their study adds the tailplane to previous studies made. This addition enables the analysis of a free-flying model. The study revealed that the primary bending modes of the wing remain stable even at speeds up to double the anticipated cruising speed of the X-57. The impact of unsteady aerodynamics is significant only on the damping ratio of the symmetric torsion mode. Although the long-period phugoid mode doesn't affect elastic modes as initially thought, the frequency of the short-period mode does influence the symmetric mode of out-of-plane bending, thereby reducing the stability of both modes. Furthermore, when the stiffness of the pylon spring is decreased to mimic the condition of a significantly damaged pylon mount, propeller whirl flutter is observed at speeds where the short-period flight dynamic mode merges with the wing's elastic modes. Another study conducted by Yeo and Kreshock [24] investigates generic hingeless propeller rotor whirl flutter in cruise flight using comprehensive rotorcraft analysis codes CAMRAD II and RCAS which are multibody dynamics codes. Their main conclusion is that the elasticity of the rotor blades influences the direction of the pylon whirl. Specifically, when the rotor is rigid, pylon motion that

## INTRODUCTION

goes against the rotor rotation direction becomes unstable. Conversely, with an elastic rotor, pylon motion in the same direction as the rotor rotation tends to become unstable. In addition, the frequency of the rotor blade significantly affects how the wing modes are damped. Generally, as the blade frequency increases, the damping of the wing mode also increases. Finally, they concluded that decreasing the air density increases significantly damping value due to lower dynamic pressure.

Although not employing multibody dynamics code as Yeao and Kreshock [24] did, the study conducted by Koch [25] focuses on how various substructures, from the stiffness of local engine mounts to the overall dynamics of the aircraft, affect the aeroelastic stability of the propeller. Findings highlight the significant impact that the complexity of the aeroelastic model has on flutter behavior. Particularly critical is the interaction with the lifting surface, which can stabilize the whirl-flutter mode. Incorporating the wing's unsteady aerodynamics into the analysis can also alter whirl flutter behavior, underlining the critical need to consider whirl flutter in comprehensive aeroelastic stability evaluations at the aircraft level. Multibody dynamics code usually employs simplified aeroelastic behavior.

The wing propeller interaction is of particular interest in the study of whirl flutter. The first wing propeller model was developed in 1964 by Bennett and Bland [26]. They analysed different configurations of a wing propeller system (Figure 7). Experimental and analytical results are obtained. Results indicate that the effect of the wing deformation on the whirl-flutter boundary was large in some system configurations, most of the time having a stabilising effect on the system. In addition, the study highlights that in the case of wing large deformation, the aerodynamic of the wing has a tendency to have a stabilising effect on the system's motion.

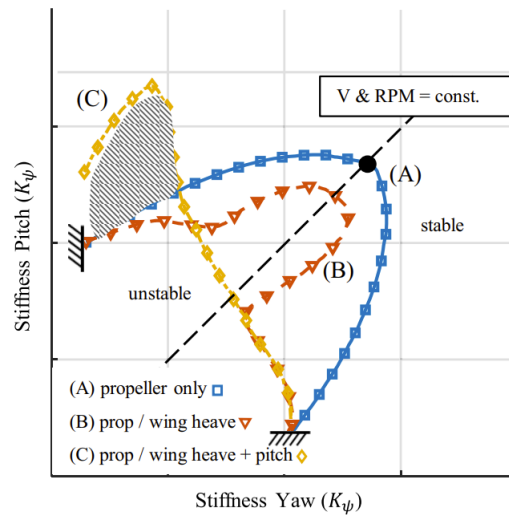


FIGURE 7 – Whirl flutter boundary and dependencies on wing motion given in the literature [27].

A study conducted by Bohnisch et al [28] studied distributed masses onto critical aeroelastic velocities of a wing propeller system. They concluded that the distributed mass, the propellers, along the wingspan influences natural frequencies, damping, and therefore flutter speed with the appearance of a hump-mode and critical flutter mode-switching. The

influence of discrete mass is intensified by the gyroscopic effect of rotating mass such as propellers (Böhnisch et al [27]). The study conducted by Böhnisch et al [27] introduce a time independant mechanical coupling between the rotating propellers and the hub in their finite element model thus neglecting partial dynamics of the rotating structure. In addition, Quanlong et al. [29] demonstrated that thrust produced by propellers on aircraft could not be neglected in predicting flutter boundary and must therefore be included in determining flutter boundary. Finally, Guruswamy [30] highlights in his study that current calculations indicate that incorporating a tip propeller results in a diverging response. Furthermore, an increase in rotation speed generally enhances stability of the wing propeller system.

Looking at the aerodynamics of air vehicles, many studies have been conducted to predict wing and propeller aerodynamic loads. A study conducted by Kosch [25] highlights different aerodynamic models used to study the whirl flutter phenomenon as unsteady aerodynamic for calculating the aerodynamic forces acting on the wing. His results show that the level of detail of the aeroelastic model used influences the prediction of the flutter behavior. In addition, his study demonstrates that the coupling with the different lifting surfaces has a strong tendency to stabilize whirl-flutter behavior.

The computation of aerodynamic forces and moments has evolved continuously over time. The first estimation of aerodynamic forces acting on a propeller was proposed during wartime by Ribner [31]. Later, a solution based on first-order strip theory is proposed by Houblot and Reed [19]. This method consists of three perturbation quantities: the local section angle of attack, the perturbation velocity in the propeller plane, and the perturbation velocity out of the propeller plane. Due to the high radial velocity of rotating propellers, Houblot and Reed also suggested adding a compressibility factor to their initial theory in order to better predict the aerodynamic force. Bennet and Bland [26] suggested a model improving on the original model proposed by Brown and Taylor. Their model takes into consideration wing deformation such as wing bending and wing torsion, which has been proven by Zwan and Bergh to have, in general, a stabilizing effect on whirl flutter [32]. Hamond et al [33] applied unsteady lifting surface theory to a rotating propeller in a compressible subsonic flow. The integral equation is generally solved using DLM [34].

With the emergence of new computing methods and the increasing availability of computing power, new techniques can be used to predict the aerodynamic forces acting on a system. Recent studies have investigated the whirl flutter phenomenon using computational fluid dynamics (CFD) as a means of predicting the aerodynamic forces acting on the various parts contributing to the phenomenon. One of the first contributions of this kind was made by Srivastava and Reddy [35] who developed a CFD code using the three-dimensional unsteady compressible Euler equations. More recently, Higgins and Barakos [36] developed a numerical model to predict whirl and flutter coupling CFD solver and a NASTRAN [37] derived model. Another computational tool which includes fluid-structure coupling has been developed by ONERA [38]. This computational tool can deal with either compressible viscid or inviscid flows. The computational method used to solve fluid dynamics is based either on RANS or URANS models with a large set of turbulence models being available. The main disadvantage of using CFD method to compute aerodynamic load on

## INTRODUCTION

lifting surfaces is the computational time required to acquire good-quality results. This might not be efficient in the conceptual design of an aircraft, where a quick approximation of whirl flutter might be necessary. However, the use of CFD can prove useful in the more advanced phases of aircraft design.

### Aim of this work

The aim of this thesis is to develop, using the Finite Element Method (FEM), an innovative mechanical coupling strategy between a rotating part and a static part to study the whirl-flutter phenomenon. This coupling, being the most complete, enables the dynamics of the rotating parts to be fully preserved, by enabling a time coupling on the mass, gyroscopic and centrifugal stiffness matrix, during modal analysis and, more particularly, during a stability study. To date, this type of coupling has never been fully realized or published in the literature using the finite element method. A paper published by Zuo et al. [39] indeed performed a time coupling between the rotating elements of a shaft and the shaft itself, but only on the stiffness matrix. Consequently, the total dynamics of the system is not represented in their equation of motion as there is no time coupling on the mass matrix and the gyroscopic matrices, making their study incomplete. This thesis therefore starts from a blank page, where each of the matrices and phenomena in play must be validated in order to ensure the correct implementation of this mechanical coupling.

### Thesis outline

In Chapter 1, notions of stability analysis are explained. From the stability of linear time invariant (LTI) systems to the stability of linear time periodic systems (LTP) using Floquet theory. In addition, the stability of a system undergoing a Coleman transformation is studied. The different perks and drawbacks of the different stability analysis are presented. The derivation of the main equations and the main results of the Floquet theory are also presented.

Chapter 2 aims at establishing and validating the different finite element matrices and components computed using Euler-Bernoulli 3D beam elements that are used later in the coupled matrix formulation of the problem. The various results and matrices obtained are validated against results in literature.

Chapter 3 deals with the time-dependent mechanical coupling between rotating and static parts. A fairly substantial mathematical review is carried out to present the various coupling equations. A numerical implementation strategy is also presented. Finally, the various coupled matrices are validated using two distinct validation models. The first model consists of a ground resonance model with which a partial coupling is validated, while the second, which consists of a rotating shaft with four blades being attached in its middle, leading to a complete validation of the coupled model.

Chapter 4 consists in an application of the developed finite element code to study an aerospace structure. First, the finite element model is applied to a Goland wing structure and the model is validated. Then, different way to compute the aerodynamics force acting on the wing are presented as well as the methodology to compute the flutter speed of a wing.

In addition, the propeller aerodynamics equations are presented. Finally, an application of the developed time coupling finite element model to a wing propeller structure is studied.

The conclusion discusses and summaries the main findings of this thesis. In addition, perspectives and possible future improvements are suggested.





The aim of this chapter is to present the main theories that can be used to study the stability of rotor systems, together with their advantages and disadvantages. In addition, the various methods required to numerically compute this stability are also presented.

## 1.1 Stability of linear time invariant system

A linear time invariant system (LTI) is a system that produces an output signal from any input signal that is, among other possible characteristic, linear and time invariant. Time invariant system can be used in many fields such as electricity and mechanics. To study the stability of LTI systems, the state space representation of the system is used. The system of equations characterising the state space representation of LTI system reads

$$\dot{\mathbf{x}}(t) = \mathbf{A}\mathbf{x}(t) + \mathbf{B}\mathbf{u}(t), \quad (1.1)$$

$$\mathbf{y}(t) = \mathbf{C}\mathbf{x}(t) + \mathbf{D}\mathbf{u}(t), \quad (1.2)$$

where  $\mathbf{x}$  is the state vector,  $\mathbf{y}$  the output vector,  $\mathbf{u}$  is the input vector,  $\mathbf{A}$  is the state matrix,  $\mathbf{B}$  is the input matrix,  $\mathbf{C}$  is the output matrix, and  $\mathbf{D}$  is the feedforward matrix.

The stability of LTI system is studied by analyzing the eigenvalues of the state space matrix  $\mathbf{A}$ . The state space matrix  $\mathbf{A}$  of time invariant mechanical system reads

$$\mathbf{A} = \begin{bmatrix} \mathbf{0} & \mathbf{I} \\ -\mathbf{M}^{-1}\mathbf{K} & -\mathbf{M}^{-1}\mathbf{C} \end{bmatrix}, \quad (1.3)$$

where  $\mathbf{M}$ ,  $\mathbf{K}$ ,  $\mathbf{C}$  respectively represent the structural mass matrix, the structural stiffness matrix and the structural damping matrix. The stability of LTI system is characterized by the sign of the eigenvalues  $\lambda_n$  characterising the system. The system is said to be:

- asymptotically stable if  $\Re(\lambda_n) < 0$ ;
- marginally stable if  $\Re(\lambda_n) = 0$ ;

- unstable if  $\Re(\lambda_n) > 0$ .

The eigenfrequencies and the modal damping ratio are retrieved thanks to

$$\omega = \sqrt{\Re(\lambda)^2 + \Im(\lambda)^2}; \quad (1.4)$$

$$\xi = \frac{-\Re(\lambda)}{\omega}. \quad (1.5)$$

## 1.2 Coleman Transformation

The aim of this thesis is to study the dynamics of time varying systems. However, this is a hazardous task that will be later proved to be complicated. That's why a Coleman transformation is often carried out [40]. Coleman-based analysis lies between LTI analysis and a full periodic analysis of the studied system. Bir [41] published a full review of the transformation in his work. Fisker [42] highlights the main steps to ensure a modal analysis of rotating structures using Coleman transformation. The main steps are:

- location of a steady state operating conditions;
- linearization of the equations of motion around the previously found steady state;
- modal decomposition of the linearised system providing modal frequencies, modal damping and modes shapes of the vibrating structure.

Using the Coleman transformation consists in applying the first two steps but, before doing the third steps, applying the Coleman transformation matrix. More information about the Coleman transformation matrix can be found in [40]. The transformation matrix reads, in its most general form,

$$\mathbf{x} = \mathbf{B}(t)\mathbf{x}_b, \quad (1.6)$$

where  $\mathbf{x}_b$  is the state variable vector and where  $\mathbf{B}(t)$  is the transformation matrix and reads

$$\mathbf{B}(t) = \begin{bmatrix} \mathbf{I}_{N_b} \cos \psi_1 & \mathbf{I}_{N_b} \sin \psi_1 & \cdots & \mathbf{I}_{N_b} \cos \tilde{B}\psi_1 & \mathbf{I}_{N_b} \sin \tilde{B}\psi_1 & -\mathbf{I}_{N_b} & 0 \\ \mathbf{I}_{N_b} \cos \psi_2 & \mathbf{I}_{N_b} \sin \psi_2 & \cdots & \mathbf{I}_{N_b} \cos \tilde{B}\psi_2 & \mathbf{I}_{N_b} \sin \tilde{B}\psi_2 & \mathbf{I}_{N_b} & 0 \\ \mathbf{I}_{N_b} \cos \psi_3 & \mathbf{I}_{N_b} \sin \psi_3 & \cdots & \mathbf{I}_{N_b} \cos \tilde{B}\psi_3 & \mathbf{I}_{N_b} \sin \tilde{B}\psi_3 & -\mathbf{I}_{N_b} & 0 \\ \vdots & \vdots & \ddots & \vdots & \vdots & \vdots & \vdots \\ \mathbf{I}_{N_b} \cos \psi_B & \mathbf{I}_{N_b} \sin \psi_B & \cdots & \mathbf{I}_{N_b} \cos \tilde{B}\psi_B & \mathbf{I}_{N_b} \sin \tilde{B}\psi_B & (-\mathbf{I}_{N_b})^B & 0 \\ 0 & 0 & \cdots & 0 & 0 & 0 & \mathbf{I}_{N_s} \end{bmatrix}, \quad (1.7)$$

where  $\tilde{B} = (B - 1)/2$  for  $B$  odd and  $\tilde{B} = (B - 2)/2$  for  $B$  even, where  $\psi_j = \Omega t + 2\pi(j - 1)/B$  is the mean azimuth angle to blade number  $j = 1, 2, \dots, B$ , and  $\mathbf{I}_{N_b}$  and  $\mathbf{I}_{N_s}$  are identity matrices of sizes  $N_b$  and  $N_s$ . In addition,  $N_b$  corresponds to the number of state variables in the rotating frame of reference and  $N_s$  is the number of inertial state variables of the rotor support.

The study of the stability of a system having undergone a Coleman transformation is established by the same stability criteria as the one previously established for LTI system.

The main advantages of the Coleman transformation is that it can be used to enable the extraction of the different modal quantities of a rotating structure by describing the

rotor degrees of freedom in the inertial frame of reference. Although it has its advantages, the Coleman transformation method also has its disadvantages. The first one is that this transformation can only be applied to isotropic systems. Therefore, studying an unbalance rotor, or studying a rotor under wind shear cannot be performed using Coleman transformation [42]. Another disadvantage of this transformation is that it is able to change the harmonic content of the different structural matrices by only leaving a small contribution of the periodicity of the studied rotating system in it. The remaining periodicity is removed by an average of the structural matrices over one period of revolution. Although it limits the contribution made by the periodicity of the system in the modal analysis, using the transformation still allows to obtain information on the frequency content of the system while still considering, to a lesser extent, the dynamics of the rotor.

## 1.3 Floquet Theory - Stability analysis of linear time periodic system

To study the stability of stationary and rotor system coupled together, a stability analysis must be carried out. In order to capture the dynamics of the system as a whole, a stability study of the system using Floquet theory must be carried out. Floquet theory enables to study the stability of linear time periodic systems. This theory was mainly developed by Floquet and Lyapunov [43]. The following subsections recall the main mathematical derivation of the Floquet theory. The main developments are based on the work of Nayfeh and Balachandran [44], Riva [45] and Bottasso and Cacciola [46].

### 1.3.1 Mathematical derivation

The state space representation of a linear time periodic system is written as

$$\dot{\mathbf{x}}(t) = \mathbf{A}(t)\mathbf{x}(t) + \mathbf{B}(t)\mathbf{u}(t), \quad (1.8)$$

$$\mathbf{y}(t) = \mathbf{C}(t)\mathbf{x}(t) + \mathbf{D}(t)\mathbf{u}(t). \quad (1.9)$$

Such a system is said to be periodic if the conditions:

$$\mathbf{A}(t+T) = \mathbf{A}(t), \quad \mathbf{B}(t+T) = \mathbf{B}(t), \quad (1.10)$$

$$\mathbf{C}(t+T) = \mathbf{C}(t), \quad \mathbf{D}(t+T) = \mathbf{D}(t), \quad (1.11)$$

are fulfilled simultaneously. The period  $T$  of the system is the smallest time interval for which the previous conditions hold.

The study of the stability of linear time periodic system is achieved by studying, as for LTI system, with the state space matrix  $\mathbf{A}(t)$ . Looking at the autonomous version of Eq.1.9 and associating an initial condition. One can rewrite the state space representation as

$$\dot{\mathbf{x}}(t) = \mathbf{A}(t)\mathbf{x}(t) \quad \text{with} \quad \mathbf{x}(0) = \mathbf{x}_0. \quad (1.12)$$

If the state of the system at time  $\tau$  is known, the state at a subsequent time  $t$  is given via the state transition matrix  $\Phi(t, \tau)$ , such that

$$\dot{\mathbf{x}}(t) = \Phi(t, \tau)\mathbf{x}(\tau). \quad (1.13)$$

The evolution of the state transition matrix is governed by

$$\dot{\Phi}(t, \tau) = \mathbf{A}(t)\Phi(t, \tau) \quad \text{with} \quad \Phi(\tau, \tau) = \mathbf{I}. \quad (1.14)$$

The state transition matrix over one period  $T$  is the most important piece of the Floquet theory and is called the monodromy matrix.

The eigenvalues  $\rho_m$  of the monodromy matrix  $\Phi$  are called the Floquet multipliers. There exists a unique set of Floquet multipliers associated with matrix  $\mathbf{A}$ . Each Floquet multiplier is a measure of the local convergence or divergence of the studied system along a particular direction over one period of the closed orbit. Introducing the transformation,

$$\mathbf{Y}(t) = \mathbf{V}(t)\mathbf{P}^{-1}, \quad (1.15)$$

where  $\mathbf{V}$  is a non singular matrix and  $\mathbf{P}$  is matrix such as its columns are the right eigenvector of the monodromy matrix. Thus, the equation

$$\mathbf{Y}(t+T) = \mathbf{V}(t)\Phi \quad (1.16)$$

can be rewritten as

$$\mathbf{V}(t+T) = \mathbf{V}(t)\mathbf{P}^{-1}\Phi\mathbf{P}. \quad (1.17)$$

If all the Floquet multipliers are distinct, Eq.1.17 can be rewritten as

$$\mathbf{V}_m(t+T) = \rho_m \mathbf{V}_m(t) \quad \forall m = 1, \dots, n. \quad (1.18)$$

From the previous equation, it follows that

$$\mathbf{V}_m(t+NT) = \rho_m^N \mathbf{V}_m(t). \quad (1.19)$$

Therefore, if  $t \rightarrow +\infty$ , then  $N \rightarrow +\infty$ , and

$$\mathbf{V}_m(t) \rightarrow 0 \quad \text{if} \quad |\rho_m| < 1 \rightarrow \text{stable} \quad (1.20)$$

$$\mathbf{V}_m(t) \rightarrow \infty \quad \text{if} \quad |\rho_m| > 1 \rightarrow \text{unstable} \quad (1.21)$$

A particular case must be considered when  $\rho_m = 1$ . In fact, when this condition is fullfield, the system's response  $\mathbf{V}_m(t)$  is periodic with period  $T$  and when  $\rho_m = -1$ , the system's response is  $2T$  periodic. The representation of the different possible cases of  $\rho_m$  in the complex plane is highlighted in Figure 1.1.

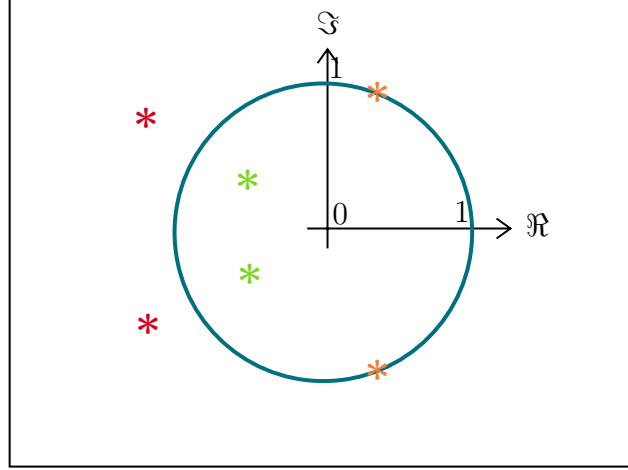


FIGURE 1.1 – Complex-plane. Positions of the eigenvalue represented by different asterisks \*. \* - eigenvalue leading to a periodic stable system, \* - eigenvalue leading to an asymptotically periodic stable system, \* - eigenvalue leading to an unstable system, Unit circle.

An important property of the Floquet multipliers associated with periodic solution  $\mathbf{X}_0(t)$  of an autonomous system of equation is always unit. The details leading to this affirmation are left to the reader but the demonstration can be found in [44].

By multiplying Eq.1.18 by  $e^{-\gamma_m(t+T)}$ , one gets

$$e^{-\gamma_m(t+T)}\mathbf{V}_m(t+T) = \rho_m e^{-\gamma_m(t+T)}\mathbf{V}_m(t), \quad (1.22)$$

where  $\gamma_m$  is defined by the relationship

$$\rho_m = e^{\gamma_m T} \Rightarrow \gamma_m = \frac{1}{T} \ln(\rho_m). \quad (1.23)$$

$\gamma_m$  are called the characteristic exponents. They are unique and integer multiple of  $\frac{2\pi i}{T}$ .

Using the periodicity property, Eq.1.22 can be rewritten as

$$e^{-\gamma_m(t+T)}\mathbf{V}_m(t+T) = \rho_m e^{-\gamma_m(t)}\mathbf{V}_m(t). \quad (1.24)$$

If  $\rho_m \neq 0$ , every  $\mathbf{V}_m$  can be expressed in the normal form

$$\mathbf{V}_m(t) = e^{\gamma_m t} \phi_m(t), \quad (1.25)$$

with  $\phi_m(t) = \phi_m(t+T)$ . Therefore, the stability of the system may also be deduced from the characteristic exponents. In fact, one can conclude that if

$$\Re(\gamma_m) < 0, \mathbf{V}_m(t) \rightarrow 0, t \rightarrow \infty \rightarrow \text{stable}, \quad (1.26)$$

$$\Re(\gamma_m) > 0, \mathbf{V}_m(t) \rightarrow \infty, t \rightarrow \infty \rightarrow \text{unstable}. \quad (1.27)$$

The previously established normal form can be used to determine the solution of

$$\dot{\mathbf{x}}(t) = \mathbf{A}(t)\mathbf{x}(t). \quad (1.28)$$

One seeks a solution of the form

$$\mathbf{x}(t) = e^{\gamma t} \phi(t). \quad (1.29)$$

To solve,

$$\dot{\phi} = [\mathbf{A}(t) - \gamma \mathbf{I}]. \quad (1.30)$$

Expanding  $\phi$  in a Fourier series leads to

$$\phi = \sum_{k=-\infty}^{k=+\infty} \mathbf{a}_k \exp\left(\frac{2ik\pi t}{T}\right). \quad (1.31)$$

Using the expression in the previous relation and equating each harmonic on both sides lead to an infinite dimensional eigenvalue problem, where the determinant of the coefficient matrix is called the Hill's determinant and is a key point when studying the stability of linear time periodic system.

## 1.4 Numerical integration schemes

As previously stated, the stability of the studied structure is characterised by analysing its stability over a period of revolution  $T$  of the rotating system. Therefore, it is necessary to solve the equation of motion characterising the motion of the system. To do so, different numerical schemes can be exploited, each of them having their perks and drawbacks. To study the stability of the studied system, the monodromy matrix must be computed. In the following sections, a mathematical derivation is proposed for some numerical scheme or an algorithm is presented to understand how to compute it when using Runge-Kutta integration scheme.

### 1.4.1 Newmark time integration scheme

The first time integration scheme being studied is the Newmark integration scheme. Starting from given initial conditions, Newmark integration scheme is used to advance the solution in time. The procedure related to the Newmark integration scheme is represented in Appendix C.

This integration scheme is characterized by three distinct variables, each of them having its influence in the obtained solution. The three variable are the time step  $h$  and the parameters  $\beta$  and  $\gamma$ . The latter is set to 0.5 leading to a minimum integration error [47]. In addition, as this value corresponds to a stability limit, it means that no artificial amplification nor numerical damping is introduced in the resolution process. The parameter  $\beta$  must be higher or equal than 0.25 to ensure unconditional stability of the numerical scheme. However, it is proven that the maximum accuracy is reached when  $\beta = 0.25$ . Therefore, in the following computations,  $\beta$  is set to 0.25. The last parameter, the time step  $h$  is defined such that the response of the system is correctly captured, with the constraint that a small time step can lead to expensive computational cost, whereas a larger time step can lead to a larger periodicity error. As a result, a compromise has to be made between the desired accuracy and calculation time.

It is worth noting that the Newmark integration scheme is not made to handle time varying mass matrix. Therefore, when being used in the scope of this thesis, it is assumed that the mass matrix between two time step is being constant. This is a large approximation which can be eliminated by using other numerical integration schemes.

#### 1.4.1.1 Mathematical derivation of the monodromy matrix for Newmark integration scheme

The aim of this thesis is to study the whirl flutter phenomenon. It is therefore of interest to derive the amplification matrix of such a scheme. From this, the monodromy matrix is derived. The mathematical derivations are skipped but are available in [47]. The monodromy matrix of the Newmark scheme reads:

$$\Psi = \prod_{t=0}^T \mathbf{H}_1^{-1}(t+1) \mathbf{H}_0(t),$$

where

$$\mathbf{H}_1 = \begin{bmatrix} \mathbf{M} + h^2\beta\mathbf{K} & \beta h^2\mathbf{C} \\ \gamma h\mathbf{K} & \mathbf{M} + \gamma h\mathbf{C} \end{bmatrix}, \mathbf{H}_0 = \begin{bmatrix} \mathbf{M} - h^2(0.5 - \beta)\mathbf{K} & h\mathbf{M} - \left(\frac{1}{2} - \beta\right)h^2\mathbf{C} \\ -(1 - \gamma)h\mathbf{K} & \mathbf{M} - (1 - \gamma)h\mathbf{C} \end{bmatrix}. \quad (1.32)$$

An issue with the presented formulation is that the acceleration terms contain the mass matrix which varies over time. In fact, the aim of this thesis is to deal with a complete implementation of the coupling between stationnary and rotating components, therefore the mass matrix will vary overtime. An alternative could be to pre-multiply the equation of the dynamics by the inverse mass matrix  $\mathbf{M}^{-1}$ , and therefore to only get an identity matrix  $\mathbf{I}$  term on the acceleration term to get this term constant. This operation can only be carried out on the assumption that the mass matrix is invertible. This is the case because the matrices encountered are the structural matrices assembled with the degrees of freedom specific to the structure already blocked. This makes the structural matrices invertible. As a result, the iteration matrix constituting the monodromy matrix reads

$$\mathbf{H}_1 = \begin{bmatrix} \mathbf{I} + h^2\beta\mathbf{K}\mathbf{M}^{-1} & \beta h^2\mathbf{C}\mathbf{M}^{-1} \\ \gamma h\mathbf{K}\mathbf{M}^{-1} & \mathbf{I} + \gamma h\mathbf{C}\mathbf{M}^{-1} \end{bmatrix};$$

$$\mathbf{H}_0 = \begin{bmatrix} \mathbf{I} - h^2(0.5 - \beta)\mathbf{K}\mathbf{M}^{-1} & h\mathbf{I} - (1/2 - \beta)h^2\mathbf{C}\mathbf{M}^{-1} \\ -(1 - \gamma)h\mathbf{K}\mathbf{M}^{-1} & \mathbf{I} - (1 - \gamma)h\mathbf{C}\mathbf{M}^{-1} \end{bmatrix}.$$

This new formulation of the monodromy matrix will be called Newmark-V2 when being used in the following of the thesis.

#### 1.4.2 Generalised $\alpha$ scheme

To compensate for the large approximation made in Newmark's integration scheme for the time-dependent mass matrix. It may make sense to use the generalised  $\alpha$  method. First, Hilbert et al [48] proposed a way of introducing numerical damping in Newmark's scheme without degrading the second order accuracy of the latter by using a single parameter



ranging from 0 to 1. Their method consists of averaging the internal forces and the external forces between two successive time steps. Later, Chung and Hulbert [49] proposed to use the same concept as the one proposed by Hilbert et al, but this time using two different averaging parameters. One of them,  $\alpha_m$ , acting on inertia forces and the other one,  $\alpha_f$ , acting on elastic and damping forces. The equation representing this numerical scheme reads

$$(1 - \alpha_m)\mathbf{M}\ddot{\mathbf{q}}_{n+1} + \alpha_m\mathbf{M}\ddot{\mathbf{q}}_n + (1 - \alpha_f)(\mathbf{K}\mathbf{q}_{n+1} + \mathbf{C}\dot{\mathbf{q}}_{n+1}) + \alpha_f(\mathbf{K}\mathbf{q}_n + \mathbf{C}\dot{\mathbf{q}}_n) \\ = (1 - \alpha_f)\mathbf{g}(\mathbf{q}_{n+1}, t) + \alpha_f\mathbf{g}(\mathbf{q}_n, t).$$

Note that when  $\alpha_m$  and  $\alpha_f$  are equal to 0 simultaneously, the Newmark integration scheme is recovered. Omitting the details leading to this result, it is shown that the scheme remains second-order accurate and is unconditionally stable if

$$\left. \begin{aligned} \gamma &= \frac{1}{2} + \alpha_f - \alpha_m \\ \beta &= \frac{1}{4}(1 + \alpha_f - \alpha_m)^2 \end{aligned} \right\} \quad \text{with} \quad 0 \leq \alpha_m \leq \alpha_f \leq \frac{1}{2}.$$

It is worth noting that the solution obtained with this numerical integration scheme depends on the values given to the parameters  $\alpha_f$  and  $\alpha_m$ . These parameters can be determined from the value given to the spectral radius

$$\left. \begin{aligned} \alpha_m &= \frac{2\rho_\infty - 1}{\rho_\infty + 1} \\ \alpha_f &= \frac{\rho_\infty}{\rho_\infty + 1} \end{aligned} \right\} \quad \text{with} \quad 0 \leq \rho_\infty \leq 1.$$

The closer the spectral radius  $\rho$  is to one, the less numerical dissipation there is. The closer the spectral radius is to zero, the more numerical dissipation there is in the high frequencies.

An in-depth parametric study is later carried out on the effect of the spectral radius on the solution obtained. However, a study carried out by Gufler et al [50] shows that having a spectral radius of less than 0.4 will often lead to a significant delay in the behaviour of the solution. Beyond this limit, the significant addition of numerical dissipation can also remove physical vibrations that are important in the behaviour of the solution.

#### 1.4.2.1 Mathematical derivation of the monodromy matrix for the Generalised $\alpha$ scheme

Similarly to the Newmark scheme, the monodromy matrix corresponding to the generalized alpha scheme reads

$$\mathbf{H}_1 = \begin{bmatrix} \mathbf{M} + \gamma h \left( \frac{1 - \alpha_f}{1 - \alpha_m} \right) \mathbf{C} & \gamma h \left( \frac{1 - \alpha_f}{1 - \alpha_m} \right) \mathbf{K} \\ \beta h^2 \left( \frac{1 - \alpha_f}{1 - \alpha_m} \right) \mathbf{C} & \mathbf{M} + \beta h^2 \left( \frac{1 - \alpha_f}{1 - \alpha_m} \right) \mathbf{K} \end{bmatrix},$$

$$\mathbf{H}_0 = \begin{bmatrix} \mathbf{M} - \left( \frac{\alpha_f}{\alpha_m} \right) h(1 - \gamma) \mathbf{C} & - \left( \frac{\alpha_f}{\alpha_m} \right) h(1 - \gamma) \mathbf{K} \\ h\mathbf{M} - h^2(0.5 - \beta) \left( \frac{\alpha_f}{\alpha_m} \right) \mathbf{C} & \mathbf{M} - h^2(0.5 - \beta) \left( \frac{\alpha_f}{\alpha_m} \right) \mathbf{K} \end{bmatrix}.$$

It is worth noting that the  $\mathbf{H}_0$  and  $\mathbf{H}_1$  matrices are similar to the matrices obtained for the Newmark integration scheme with the only difference being that in the expression of the matrices in the case of the generalized  $\alpha$  scheme, the influence of the various weighting parameters on the inertia, elastic and damping forces can be seen. In addition, it is important to note that the different matrices involved in the amplification matrices  $\mathbf{H}_0$  and  $\mathbf{H}_1$  correspond to the structural matrices calculated at time  $t_n$  and  $t_{n+1}$  respectively.

### 1.4.3 Runge-Kutta integration scheme

The last numerical method used is the Runge-Kutta method. This method is widely used to solve differential equations numerically. It is an explicit solution scheme. In this thesis, the Runge-Kutta method employed is based on a Dormand-Prince Runge-Kutta method [51] that uses fourth- and fifth-order approximations to estimate the solution of ordinary differential equations. The main advantage of this method, which has an adaptive time step, is that it speeds up the resolution when the solution is no longer subject to large variations, but also reduces the time step when large variations are encountered while guaranteeing a relatively low relative error. In conclusion, its major advantage over other numerical schemes is its error control.

#### 1.4.3.1 Derivation of the monodromy matrix

As with the other numerical schemes employed, it is in the interest of this thesis to derive the expression of the monodromy matrix to study the stability of the structure studied. For the Runge-Kutta numerical scheme, deriving an explicit formulation of the monodromy matrix is not possible. However, it is still possible to compute it numerically. To do so, the monodromy matrix is built up progressively. Each column of the monodromy matrix at a time  $t$  is constructed by imposing an unitary initial condition on the displacement  $U(i) = 1$ , where  $i$  corresponds to the degree of freedom being studied. The others are left to zero. The numerical scheme is then solved using the previously computed initial condition vector. The solution vector corresponds to the column  $i$  of the monodromy matrix being build at time  $t$ . This operation is repeated for each degree of freedom  $i$  composing the structure. This procedure is summarised in the Algorithm 1.

---

**Algorithm 1** Computation of Monodromy Matrix for Runge-Kutta Integration Scheme

---

- 1: **for**  $j=1$  to  $2 \times \text{Number of dof}$  **do**
  - 2:     Initialize  $U_0$  as a zero vector of size  $(2 \times \text{number of dof}, 1)$
  - 3:      $U_0[j] = 1$
  - 4:     Define  $t$  as  $[0, \text{Period}]$
  - 5:     Solve the ODE using Runge-Kutta integration scheme with initial condition vector  $U_0$
  - 6:     Update monodromy matrix  $\Phi(:, j)$  with the last value of  $U$ , the solution of the integration scheme
  - 7: **end for**
-

## 1.5 Campbell diagram and the advantage of the periodic Campbell diagram

The Campbell diagram is used to show the evolution of the natural frequencies of a system containing rotating components as a function of the speed of rotation of these same components.

The most commonly used approximation being made is the linear time invariant system approximation. However, this approximation has the effect of neglecting the time expenditure of the terms influencing the dynamics of the system under study. In addition, it only reveals one natural frequency per rotating structure. This approximate the obtained final results and therefore it neglects an important part of the system dynamics as can be seen in Figure 1.2. Although this approximation has its advantages, it is beginning to reach its limits. In fact, the aeronautics and energy industries are tending to make increasingly bulky structures while trying to reduce their weight as much as possible to gain in efficiency.

The Coleman transformation, explained before, allows several harmonics to appear for each mode, which improves the accuracy of the result obtained compared to when an approximation of a LTI system, while still approximating the real solution. This improvement in capturing the system dynamics is shown in Figure 1.3 and by comparing it with Figure 1.2.

Finally, the linear time periodic method, which is the method used in this thesis, allows theoretically to compute an infinite number of frequencies associated with each mode and therefore, to fully capture the dynamics of the rotating system. Each of the frequencies has a modal participation factor and therefore has their impact on the solution. It is worth noting that when the participating factor of a harmonic is exactly one, while the other one is equal to zero, the Campbell diagram obtained for this mode of deformation will be equivalent to the one obtained with the linear time invariant method. The Campbell diagram obtained using such a method is represented in Figure 1.4

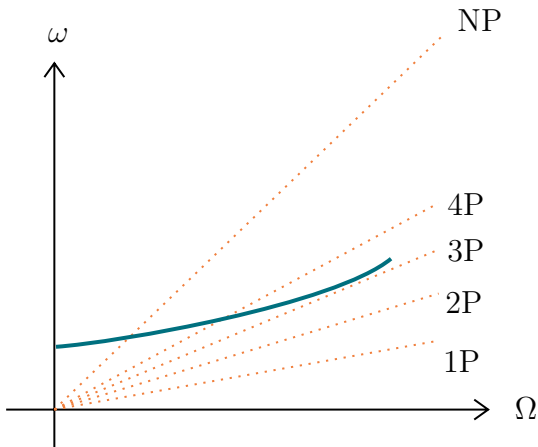


FIGURE 1.2 – Campbell diagram with LTI approximation. Reproduced from [45]

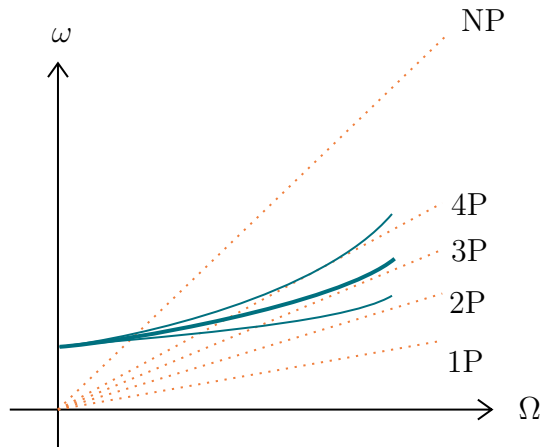


FIGURE 1.3 – Campbell diagram with Coleman transformation. Reproduced from [45].

1.5. CAMPBELL DIAGRAM AND THE ADVANTAGE OF THE PERIODIC  
CAMPBELL DIAGRAM

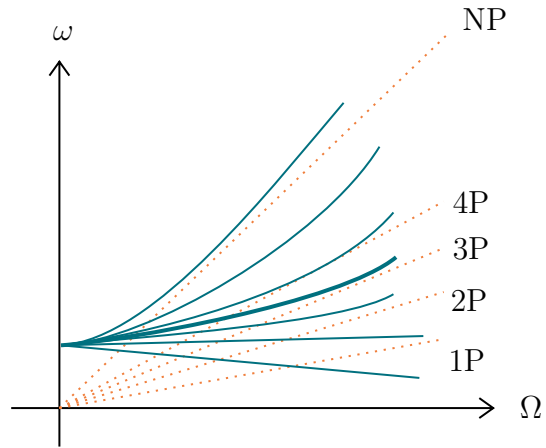


FIGURE 1.4 – Campbell diagram using LTP method. Reproduced from [45]



## 2.1 Finite element selection

To build the finite element model, it is mandatory to choose the type of element that will model the studied structure. An Euler-Bernoulli beam element is chosen to study the structure.

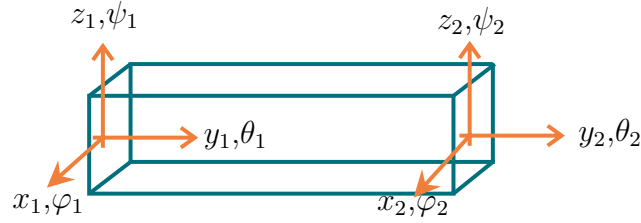


FIGURE 2.1 – Euler-Bernoulli beam element constitute of two nodes, each node containing 3 translational degrees of freedom and 3 rotational degrees of freedom.

Euler-Bernoulli elements are constructed using several kinematic assumptions. According to Bauchau and Craig [52], Euler-Bernoulli are made of the following kinematic assumptions:

- The cross-section is infinitely rigid in its own plane.
- The cross-section of a beam remains plane after deformation.
- The cross-section remains normal to the deformed axis of the beam.

It is proved that these assumptions are valid for long, slender, and isotropic beams. When one of these conditions is not met, a loss of precision is to be expected.

The first structure being studied is a single rotating beam which is clamped at the root. The structure is subject to physical effects which are linked to its rotation. The equation describing the motion of this structure in a rotating frame of reference reads

$$\mathbf{M}\ddot{\mathbf{q}}(t) + (\mathbf{D} + \mathbf{G})\dot{\mathbf{q}}(t) + (\mathbf{K} + \mathbf{P} - \mathbf{K}_\Omega)\mathbf{q}(t) = \mathbf{r}(t),$$

where  $\mathbf{q}$  is the generalized coordinate vector. In the present study, only the behavior of the structure rotating at a constant speed is carried out so that the term corresponding to the angular acceleration matrix  $\mathbf{P}$  is null. This term cannot be neglected when studying motor powering, which is not the case in this thesis. Consequently, the equation of motion of a particle rotating at constant speed is

$$\mathbf{M}\ddot{\mathbf{q}}(t) + (\mathbf{D} + \mathbf{G})\dot{\mathbf{q}}(t) + (\mathbf{K} - \mathbf{K}_\Omega)\mathbf{q}(t) = \mathbf{r}(t). \quad (2.1)$$

Defining  $\mathbf{N}$  as the shape function matrix and  $\mathbf{B}$  as the deformation matrix, the mathematical definitions of the various terms making up the above equation are:

- The mass matrix  $\mathbf{M}$ :

$$\mathbf{M} = \int_V \rho \mathbf{N}^T \mathbf{N} dV;$$

- The gyroscopic matrix  $\mathbf{G}$ :

$$\mathbf{G} = \int_V 2\rho \mathbf{N}^T \boldsymbol{\Omega} \mathbf{N} dV;$$

- The elastic stiffness matrix  $\mathbf{K}$ :

$$\mathbf{K} = \int_V \mathbf{B}^T \mathbf{C} \mathbf{B} dV;$$

- The centrifugal acceleration matrix  $\mathbf{K}_\Omega$ :

$$\mathbf{K}_\Omega = \int_V \rho \mathbf{N}^T \boldsymbol{\Omega}^2 \mathbf{N} dV.$$

- The internal force vector:

$$\mathbf{r} = - \int_V \rho \mathbf{N}^T \boldsymbol{\Omega}^2 \mathbf{x} dV,$$

where  $\mathbf{x}$  is the location vector taken from the axis of rotation of the structure and  $\boldsymbol{\Omega}$  is the rotation matrix directly coming from the rotation vector  $\boldsymbol{\omega} = [\omega_1, \omega_2, \omega_3]^T$ , which reads

$$\boldsymbol{\Omega} = \begin{bmatrix} 0 & -\omega_3 & \omega_2 \\ \omega_3 & 0 & -\omega_1 \\ -\omega_2 & \omega_1 & 0 \end{bmatrix}.$$

The definition of the different shape function is available in Appendix B. To gain so computation time, it might useful to directly use the predefined formulations of the elementary mass and elementary elastic stiffness matrix for 3D Euler-Bernoulli beam elements. These different matrices are available in Appendix A and Appendix C.

To build the structural damping matrix  $\mathbf{C}$ , the methodology introduced by Gerardin and Rixen [47] is followed. The modal damping coefficients  $\epsilon_s$  are defined by

$$\epsilon_s = \frac{\beta_s}{2\omega_s \mu_s}, \quad (2.2)$$

where  $\omega_s$  corresponds to the pulsation of mode  $\mathbf{x}_s$  and  $\mu_s$  is computed as

$$\mu_s = \mathbf{x}_s^T \mathbf{M} \mathbf{x}_s \quad (2.3)$$

To build a damping matrix that guarantees diagonal modal damping, a proportional damping approach is chosen and reads as

$$\mathbf{C} = \sum_{s=1}^n \mathbf{K} \mathbf{x}_s \frac{2\varepsilon_s}{\omega_s^2 \mu_s} \mathbf{x}_s^T \mathbf{K}, \quad (2.4)$$

where  $n$  represents the number of modes considered.

In general, only a small amount of modes are identified and therefore the damping matrix  $\mathbf{C}$  is computed as

$$\mathbf{C} = \sum_{s=1}^{m < n} \mathbf{K} \mathbf{x}_s \frac{2\varepsilon_s}{\omega_s^2 \mu_s} \mathbf{x}_s^T \mathbf{K}, \quad (2.5)$$

where the diagonal elements of the modal damping matrix  $\Phi^T \mathbf{C} \Phi$ , where  $\Phi$  is the modal matrix are given by

$$\beta_s = 2\varepsilon_s \omega_s \mu_s \quad (2.6)$$

with the conditions,

$$\beta_s = \begin{cases} 2\varepsilon_s \omega_s \mu_s, & \text{if } s \leq m \\ 0, & \text{if } s > m. \end{cases} \quad (2.7)$$

This equation is quite a big approximation as it assumes no modal damping for missing nodes. Therefore, to correct this truncated approximation, a linearly increasing damping coefficient is assumed for the higher modes. The damping of the higher modes is given by

$$\mathbf{C} = a\mathbf{K}, \quad (2.8)$$

such that

$$\varepsilon_s = \frac{a\omega_s}{2}, \quad s > m. \quad (2.9)$$

Therefore, the diagonal off terms of  $\Phi^T \mathbf{C} \Phi$  are expressed as:

$$\beta_s = a\omega_s^2 \mu_s, \quad s > m. \quad (2.10)$$

As a result, the damping matrix is built as

$$\mathbf{C} = a\mathbf{K} + \sum_{s=1}^{m < n} \mathbf{K} \mathbf{x}_s \left( \frac{2\varepsilon_s}{\omega_s^3 \mu_s} - \frac{a}{\omega_s^2 \mu_s} \right) \mathbf{x}_s^T \mathbf{K}.$$

In this work, a modal damping coefficient of 0.01% is assumed (Megson [53]) for the first six modes of deformation, whereas a linearly increasing damping coefficient for a mode higher than 6 is supposed. This is an approximation and it goes without saying that to find true damping values, laboratory tests of the various materials and structures studied must be carried out.

The various integrals presented in this work are computed using Gauss-Legendre numerical integration. This integration method has the advantage of being exact when dealing with polynomials, which is the case given the expression of the matrix of shape functions.



More details on this method are available in Appendix E.

In this study, all physical phenomena are taken into account. Therefore, it is necessary to introduce in Eq. 2.1 the geometrical stiffness matrix originating from the deformation of the beam due to the centrifugal force. The equation of motion of a particle rotating at constant speed is

$$\mathbf{M}\ddot{\mathbf{q}}(t) + (\mathbf{D} + \mathbf{G})\dot{\mathbf{q}}(t) + (\mathbf{K} - \mathbf{K}_\Omega + \mathbf{K}_g)\mathbf{q}(t) = \mathbf{r}(t). \quad (2.11)$$

The expression of the geometrical stiffness matrix  $\mathbf{K}_g$  is

$$\mathbf{K}_g = \int_V \rho \mathbf{N}'^T \sigma_0 \mathbf{N}' dV. \quad (2.12)$$

To compute the geometrical stiffness matrix, the initial stress of the structure is required. To do so, the axial displacement of each element is computed. As a result, the static problem

$$\mathbf{K}\mathbf{q} = \mathbf{r}(t)$$

is solved. Knowing the generalized displacement of the structure, the initial stress tensor  $\sigma_0$  of the element is computed thanks to Young's modulus  $E$  linking the stress and the deformation.

### 2.1.1 Validation of the centrifugal force

To validate the first model, it is crucial to validate the different components taking part in the dynamic of the future coupled structure. Therefore, to begin with, the computation of the centrifugal force is validated. To do so, a validation comparing the implementation of the computational code with a reference solution provided by the ASTER code [54]. The validation reference reports [55] provides numerous results using different types of elements. The analytical solution for a rotating beam in the local reference frame of the beam reads

$$\frac{\partial^2 U_x}{\partial x^2} + \frac{\rho}{E} \omega^2 x = 0 \quad \text{with} \quad \begin{cases} U_x(0) = 0 \\ \frac{\partial U_x}{\partial x}(L) = \sigma_{xx}(L) = 0 \end{cases}. \quad (2.13)$$

Therefore, the displacement in local frame of reference reads:

$$U_x(x) = \frac{\rho \omega^2}{2E} \left( xL^2 - \frac{x^3}{3} \right), \quad \text{with} \quad U_y = U_z = 0. \quad (2.14)$$

The displacements of all points of the beam can be written in the global reference frame, by

$$U_x(X, Y, Z) = \frac{\rho \omega^2}{2\sqrt{3}E} \left( rL^2 - \frac{r^3}{3} \right) \quad \text{with} \quad r = \sqrt{X^2 + Y^2 + Z^2}, \quad (2.15)$$

which is used to compare the obtained results of the developed model. The obtained results and the comparison with the analytical solution are represented in Figure 2.2. The result is obtained by discretising the beam using 100 elements.

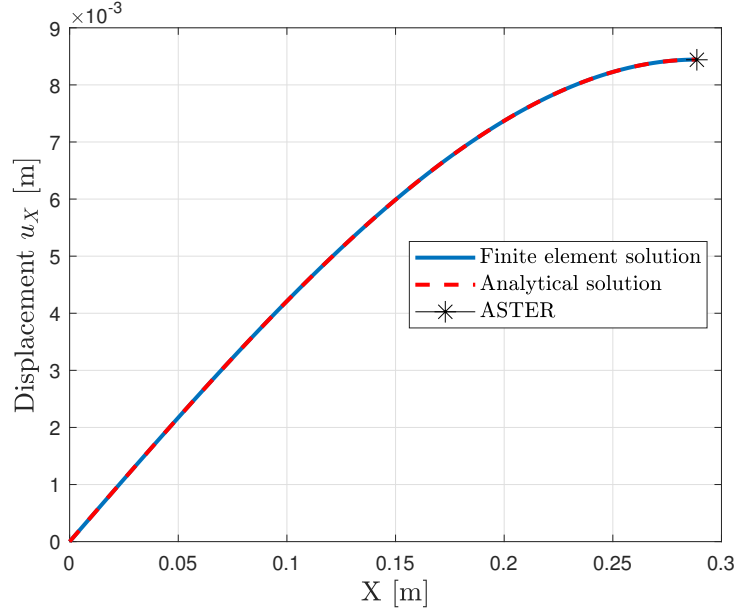


FIGURE 2.2 – Axial displacement  $u_X$  in global frame of reference. The beam is directed along the direction vector  $[1 \ 1 \ 1]$  with a rotation speed vector  $\mathbf{\Omega} = [\Omega \ 0 \ -\Omega]$  with  $\Omega = 3000$  rad/s.  $u_X$  is the displacement along the X direction in the global frame of reference.

Figure 2.2 highlights the good correlation between the finite element solution implemented and the analytical solution. In addition, the finite element solution corresponds to the solution obtained via ASTER with a relative error of 0.04 % at the tip of the beam. Code Aster only provides a single result, the one at the tip of the beam. Therefore, it is safe to conclude that the finite element implementation of the centrifugal force via the developed finite element code is correct.

Figure 2.3 reveals that, by taking into account the geometric stiffness in addition to the elastic stiffness when calculating the displacement due to centrifugal forces, the displacement is less since the structure is stiffer. This calculation has no real physical meaning but is intended to show that the geometric stiffness matrix does have a stiffening effect. Given that no validation data for the geometric stiffness matrix has been found and that the observed behavior is indeed a stiffening effect, it is reasonable to assume that the implementation is correct and can therefore be used in the remaining of this work.

### 2.1.2 Analytical model validation

The mathematical model previously expressed is developed in MATLAB [56]. Results obtained via the implemented model are compared to results obtained via commercial software. The commercial software chosen to validate the model is Ansys Workbench [57]. Ansys Workbench is a well-known finite element analysis software that has already proven its capability to provide accurate and reliable results of rotating structures (Hisham et al [58]).

To validate the analytical model implemented in MATLAB, the case of a propeller compound of four propeller blades is studied. More precisely, an analysis is performed on a

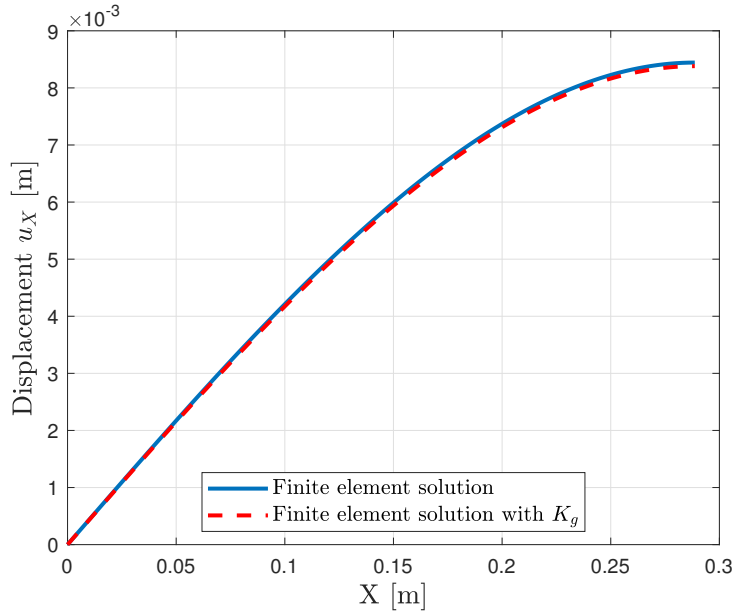


FIGURE 2.3 – Axial displacement  $u_X$  in a global frame of reference taking into account  $K$  and  $K_g$ . The beam is directed along the direction vector  $[1 \ 1 \ 1]$  with a rotation speed vector  $\mathbf{\Omega} = [\Omega \ 0 \ -\Omega]$  with  $\Omega = 3000$  rad/s.  $u_X$  being the displacement along the X direction in the global frame of reference.

single blade of the propeller. The blade is assumed to be a circular beam rotating clamped to the rotor. A schematic of the studied structure is represented in Figure 2.4.

The different simulations leading to the validation of the model are carried out using identical material properties.

### 2.1.2.1 Eigenfrequencies computation and Campbell diagram

As mentioned previously, given that the structure under study undergoes a rotational movement, it is expected that a shift in the natural frequencies of the structure due to this rotation is possible. This shift itself is a function of the rotational speed of the structure. To ensure that the natural frequencies match when the structure rotates at different speeds, a natural frequency tracking system is set up using the modal assurance criterion matrix (MAC Matrix) as proposed by Pastor et al [59]:

$$\mathbf{MAC} = \frac{|\boldsymbol{\psi}_i^T \boldsymbol{\psi}_{i-1}|^2}{(\boldsymbol{\psi}_i^T \boldsymbol{\psi}_i)(\boldsymbol{\psi}_{i-1}^T \boldsymbol{\psi}_{i-1})}, \quad (2.16)$$

where  $i$  corresponds to the studied rotation speed,  $i - 1$  to the previous rotation speed and  $\boldsymbol{\psi}$  to a mode shape of the structure. The MAC matrix is the ideal candidate for implementing the tracking system since only the natural frequencies vary as a function of rotation speed, therefore tracking them allows us to follow the evolution of the system's dynamics as its speed of rotation changes. Consequently, these are a good indicator for identifying the natural eigenfrequencies between different speeds of rotation of the studied structure.

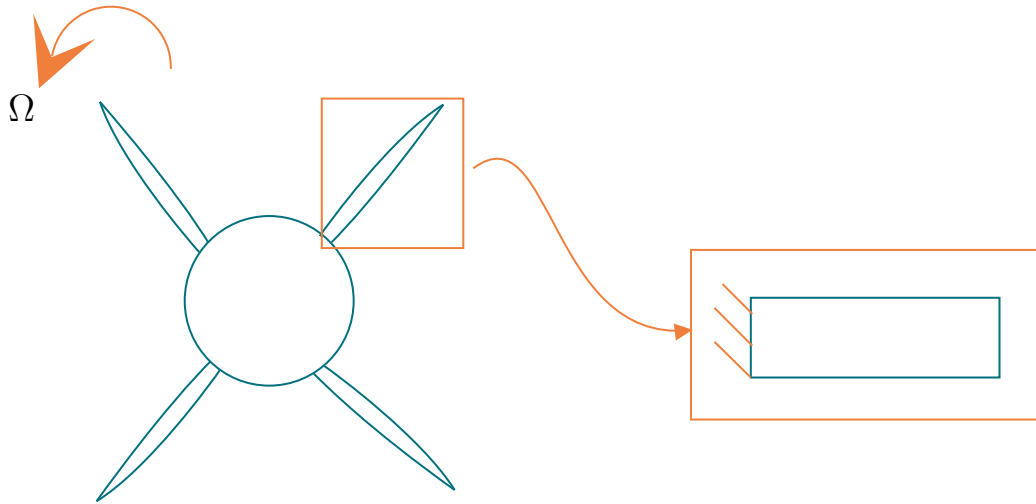


FIGURE 2.4 – Validation model: single clamped rotating beam.

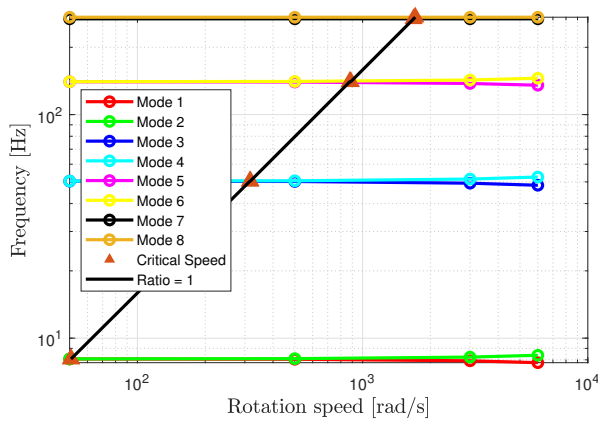


FIGURE 2.5 – Campbell diagram using Ansys model.

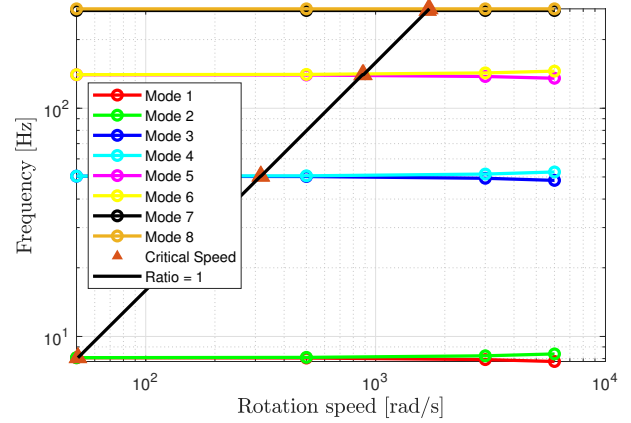


FIGURE 2.6 – Campbell diagram using MATLAB model.

Model	Mode	Direction	100 Hz	200 Hz	300 Hz	400 Hz	500 Hz	600 Hz
ANSYS	1	BW	7.83 Hz	7.83 Hz	7.82 Hz	7.82 Hz	7.81 Hz	7.81 Hz
MATLAB	1	BW	7.83 Hz	7.83 Hz	7.82 Hz	7.82 Hz	7.81 Hz	7.81 Hz
ANSYS	2	FW	7.84 Hz	7.85 Hz	7.85 Hz	7.86 Hz	7.86 Hz	7.87 Hz
MATLAB	2	FW	7.84 Hz	7.85 Hz	7.85 Hz	7.86 Hz	7.86 Hz	7.87 Hz
ANSYS	3	BW	48.88 Hz	48.85 Hz	48.81 Hz	48.78 Hz	48.74 Hz	48.71 Hz
MATLAB	3	BW	48.88 Hz	48.85 Hz	48.81 Hz	48.78 Hz	48.74 Hz	48.71 Hz
ANSYS	4	FW	48.95 Hz	48.99 Hz	49.02 Hz	49.06 Hz	49.09 Hz	49.13 Hz
MATLAB	4	FW	48.95 Hz	48.99 Hz	49.02 Hz	49.06 Hz	49.09 Hz	49.13 Hz
ANSYS	5	BW	136.05 Hz	135.96 Hz	135.88 Hz	135.80 Hz	135.72 Hz	135.63 Hz
MATLAB	5	BW	136.05 Hz	135.96 Hz	135.88 Hz	135.80 Hz	135.72 Hz	135.63 Hz
ANSYS	6	FW	136.21 Hz	136.29 Hz	136.38 Hz	136.46 Hz	136.54 Hz	136.63 Hz
MATLAB	6	FW	136.21 Hz	136.29 Hz	136.38 Hz	136.46 Hz	136.54 Hz	136.63 Hz

TABLE 2.1 – Comparison of MATLAB and ANSYS results for different rotation speeds. BW = backward whirl and FW = forward whirl.

The results obtained using the analytical model and Ansys are highlighted in Table 2.1, in Figure 2.5 and Figure 2.6. Looking at the different results, it is concluded that the developed analytical model has been correctly implemented and can be used in more complex models to study the whirl-flutter phenomenon.

The influence of the matrices  $\mathbf{K}_g$  and  $\mathbf{K}_\Omega$  is twofold: on one hand, it causes a stiffening effect due to the tensile stresses induced by rotation, and on the other hand, a softening effect is induced due to the non-inertial frame in which the equations of motions are expressed. The combination of these effects results in a net stiffening effect, leading to an increase in the absolute value of both the forward and backward branches of the Campbell diagram. This effect is clearly visible in Figure 2.6. In fact, as the frequencies relating to the whirl flutter phenomena come in pairs, it can be seen that as the speed of rotation of the structure increases, the frequencies become further apart. This phenomenon confirms the correct implementation of the analytical model.

## 2.2 Single clamped beam

Always with the same objective of continuing the validation of the finite element model developed, the second structure being studied is a cantilever beam (Figure 2.7).

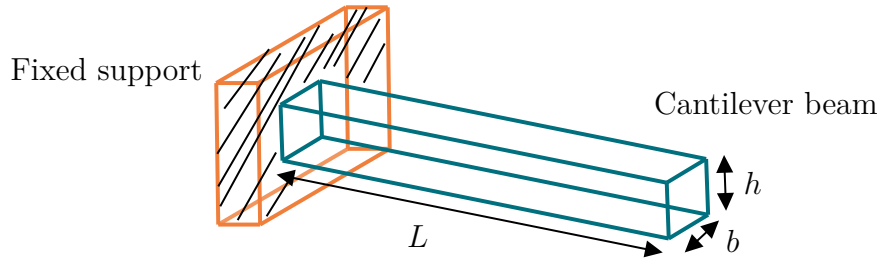


FIGURE 2.7 – Validation model: single cantilever beam.

The equation of motion describing the movement of structure in a static frame of reference reads

$$\mathbf{M}\ddot{\mathbf{q}} + \mathbf{C}\dot{\mathbf{q}} + \mathbf{K}\mathbf{q} = \mathbf{f}. \quad (2.17)$$

An analytical solution has been developed by Meirovitch [60]. The analytical solution assume that the mass of the beam is distributed along with the stiffness of the beam. The analytical equation of motion reads

$$\frac{d}{dx^2} \left[ EI(x) \frac{d^2 Y(x)}{dx^2} \right] = \omega^2 m(x) Y(x). \quad (2.18)$$

For a cantilever beam the equations are simplified as

$$\frac{d^4 Y(x)}{dx^4} - \beta^4 Y(x) = 0, \quad (2.19)$$

where  $\beta^4 = \omega^2 m / EI$ . Finally, the first three in-plane eigenfrequencies computes as

$$\omega_n = \alpha_n^2 \sqrt{\frac{EI}{\rho AL^5}}, \quad (2.20)$$

where for the three first in-plane eigenfrequencies,  $\alpha_n = 1.875, 4.694$  and  $7.885$ .

### 2.2.1 Validation of the model

The finite element model is tested using beam elements. Material and geometrical properties are highlighted in Table 2.2.

<i>Parameter</i>	<i>Value</i>	<i>Units</i>
Young's modulus $E$	210	GPa
Poisson's ratio $\nu$	0.30	-
Density $\rho$	7800	kg/m <sup>3</sup>
Length $L$	5.7	m
Height $h$	0.05	m
Width $b$	0.03	m

TABLE 2.2 – Material properties and geometrical properties of the constituting beam.

The results are highlighted in Table 2.3 and compared to analytical model predictions. It is noticeable that the FEM model develops 3 new eigenfrequencies that the analytical model developed by Meirovitch does not highlight (Figure 2.8). These three new eigenfrequencies come from out-of-plane/torsion modes of deformation which are not considered in the 2D model developed by Meirovitch. Looking at the relative error between the eigenfrequencies computed by the finite element model and the analytical model, it makes sense to deduce that the implemented finite element model has been correctly set up and can be used subsequently.

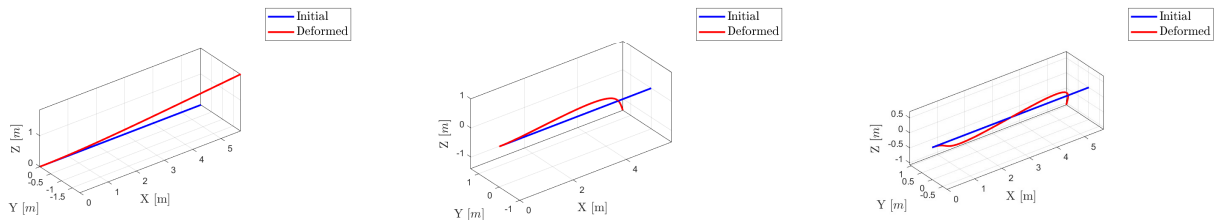


FIGURE 2.8 – Out of plane mode of deformation. From left to right: first mode, third mode, and fifth mode of deformation.

Frequency	$f_1$	$f_2$	$f_3$	$f_4$	$f_5$	$f_6$
MATLAB FE model frequency [Hz]	0.7740	1.2899	4.8504	8.0841	13.58	22.64
Analytical model frequency [Hz]	/	1.2898	/	8.0835	/	22.8095
Relative error [%]	/	$\approx 0$	/	$\approx 0$	/	-0.8

TABLE 2.3 – First six natural frequencies obtained using MATLAB with 10 elements discretising the beam, and comparison with the analytical model. Relative error computed assuming analytical solution frequency being the reference.

## 2.3 Conclusion

In this chapter was demonstrated the good implementation of the different structural matrix and of the centrifugal force using the finite element method. The different mathematical derivation of the matrices are presented and are validated against results obtained using a finite element commercial software. The centrifugal force implementation is validated using an analytical solution and the usage of result obtained using open-source code. The analysis performed for the single rotating beam is carried out in the static frame of reference. Therefore, it is now of interest to express the rotating element finite element formulation in the rotating frame of reference using a time coupling between the rotating elements namely the blades and the stationary component, the hub. This temporal coupling is the subject of the third chapter.

## CHAPTER 3

# COUPLING BETWEEN STATIONARY AND ROTATING PARTS

### 3.1 Preamble

The present work aims to establish a new method to study the whirl-flutter phenomenon. To do so, a full coupling between stationary and rotating parts of a structure is established. The coupling is a time dependent coupling. This coupling takes place on the mass matrix, the gyroscopic matrix, and the centrifugal stiffness matrix. The coupling strategy employed aims to couple the dynamics of the rotating parts of a structure expressed in the rotating frame of reference with the rest of the structure, which is expressed in the inertial frame of reference. Thanks to this coupling, all the dynamics of the structure can be captured and no information is lost.

According to the author, the implementation of this full finite element coupling strategy has never been performed or published in the literature before. A recent attempt to perform partial time coupling on the stiffness matrix using finite element method was made by Zuo et al.[39] who also employed the Floquet theory to determine the stability of the system under study. However, they study performed only a partial coupling, not a full coupling between stationary and rotating parts thus neglecting a lot of the dynamics of the rotating components.

### 3.2 Theoretical and mathematical background

The mathematical derivation is mainly based on the work produced by Vollan and Komzsik [61] with additional information and mathematical development being included.

#### 3.2.1 Full coupling of stationary and rotating parts

Before going into the mathematical derivation of the coupling for the finite element formulation of the problem. It is of interest to understand beforehand, the coupling of particles of mass  $m$ . Less complete types of coupling also exists, they might be useful to capture



some physical phenomena. However, there are not of interest in the developed model and therefore only a focus on the full coupling of the particles of mass  $m$  is achieved. The coupling of stationary and rotating parts allows translational and rotational displacements on both stationary and rotating particles. A schematic of the studied coupling is highlighted in Figure 3.1.

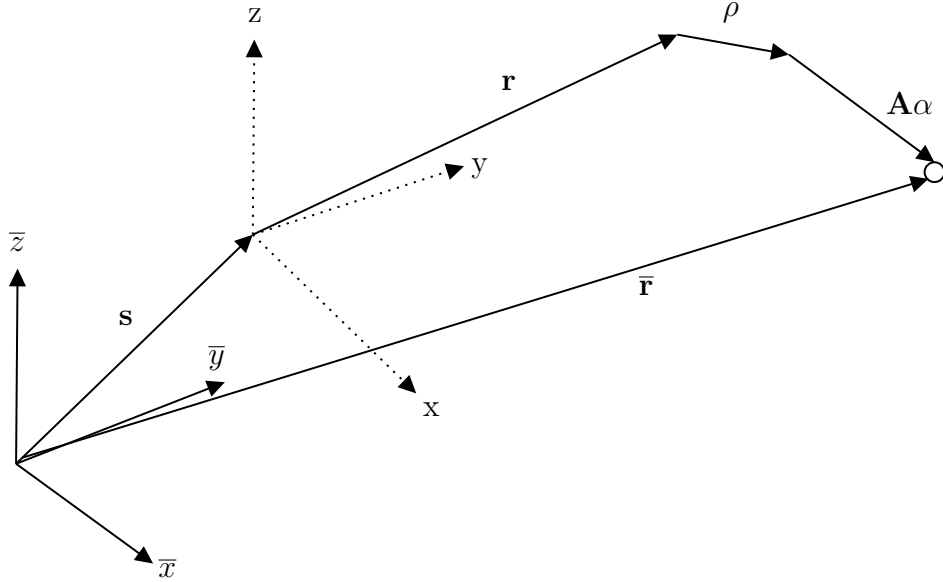


FIGURE 3.1 – Schematic of the full coupled stationary and rotating parts. Reproduced from [61].

In Figure 3.1,  $\mathbf{s}$ ,  $\boldsymbol{\rho}$  and  $\mathbf{A}\boldsymbol{\alpha}$  represents respectively the translation vector of the stationary part, the translation vector of the rotating part, and the transformation matrix of the rotational deformation of the rotating part. The location vector of a rotating particle reads, in its most general form,

$$\bar{\mathbf{r}} = \mathbf{s} + \mathbf{B}\mathbf{H}\mathbf{r} + \mathbf{H}\boldsymbol{\rho} + \mathbf{H}\mathbf{A}\boldsymbol{\alpha} + \mathbf{H}\mathbf{r}, \quad (3.1)$$

where the  $\{\bar{\cdot}\}$  makes reference to the fixed coordinate system. The matrix  $\mathbf{B}$  corresponds to the transformation matrix of the small nodal translations. This matrix reads as

$$\mathbf{B} = \begin{bmatrix} 0 & -\bar{\theta} & \bar{\psi} \\ \bar{\theta} & 0 & -\bar{\varphi} \\ -\bar{\psi} & \bar{\varphi} & 0 \end{bmatrix}. \quad (3.2)$$

It is also of interest to introduce the transformation matrix  $\mathbf{H}$  which allows switching from a location vector located in the rotating frame of reference to the fixed coordinate system. This transformation matrix reads

$$\mathbf{H} = \begin{bmatrix} \cos \Omega t & -\sin \Omega t & 0 \\ \sin \Omega t & \cos \Omega t & 0 \\ 0 & 0 & 1 \end{bmatrix}. \quad (3.3)$$

This transformation matrix is only valid for a rotation around the  $z$ -axis. One also introduces the matrix  $\mathbf{A}$ , which is simply the matrix containing the coordinates of rotating

nodes. This matrix reads

$$\mathbf{A} = \begin{bmatrix} 0 & z' & -y' \\ -z' & 0 & x' \\ y' & -x' & 0 \end{bmatrix}, \quad (3.4)$$

, where the notation  $\{\cdot\}$  refers to the coordinates of the rotating mass points.

### 3.2.1.1 Mathematical properties of the transformation matrix $\mathbf{H}$

It is of interest to introduce some mathematical properties of the transformation matrix  $\mathbf{H}$ .

$$\mathbf{H}^T \mathbf{H} = \begin{bmatrix} 1 & 0 & 0 \\ 0 & 1 & 0 \\ 0 & 0 & 1 \end{bmatrix} = \mathbf{I}; \quad (3.5)$$

$$\dot{\mathbf{H}} = \Omega \begin{bmatrix} -\sin \Omega t & -\cos \Omega t & 0 \\ \cos \Omega t & -\sin \Omega t & 0 \\ 0 & 0 & 0 \end{bmatrix} = \Omega \bar{\mathbf{H}}; \quad (3.6)$$

$$\ddot{\mathbf{H}} = \Omega^2 \begin{bmatrix} -\cos \Omega t & \sin \Omega t & 0 \\ -\sin \Omega t & -\cos \Omega t & 0 \\ 0 & 0 & 0 \end{bmatrix} = \Omega^2 \bar{\bar{\mathbf{H}}}; \quad (3.7)$$

$$\bar{\mathbf{H}}^T \mathbf{H} = \begin{bmatrix} 0 & 1 & 0 \\ -1 & 0 & 0 \\ 0 & 0 & 0 \end{bmatrix} = \mathbf{P}; \quad (3.8)$$

$$\mathbf{H}^T \bar{\mathbf{H}} = \begin{bmatrix} 0 & -1 & 0 \\ 1 & 0 & 0 \\ 0 & 0 & 0 \end{bmatrix} = \mathbf{P}^T = -\mathbf{P}; \quad (3.9)$$

$$\bar{\mathbf{H}}^T \bar{\mathbf{H}} = \begin{bmatrix} 1 & 0 & 0 \\ 0 & 1 & 0 \\ 0 & 0 & 0 \end{bmatrix} = \mathbf{J} = \bar{\mathbf{H}} \bar{\mathbf{H}}^T. \quad (3.10)$$

To take into account the rotation of the stationary part, it is of interest to rewrite the second term of Eq.3.1. The following transformations allow the rotation of the stationary part to be taken into account:

$$\begin{aligned}
 \mathbf{B}\mathbf{H}\mathbf{r} &= \begin{bmatrix} 0 & -\bar{\theta} & \bar{\psi} \\ \bar{\theta} & 0 & -\bar{\varphi} \\ -\bar{\psi} & \bar{\varphi} & 0 \end{bmatrix} \begin{bmatrix} \cos \Omega t & -\sin \Omega t & 0 \\ \sin \Omega t & \cos \Omega t & 0 \\ 0 & 0 & 1 \end{bmatrix} \begin{Bmatrix} x \\ y \\ z \end{Bmatrix} \\
 &= \begin{bmatrix} 0 & -\bar{\theta} & \bar{\psi} \\ \bar{\theta} & 0 & -\bar{\varphi} \\ -\bar{\psi} & \bar{\varphi} & 0 \end{bmatrix} \begin{Bmatrix} x \cos \Omega t - y \sin \Omega t \\ x \sin \Omega t + y \cos \Omega t \\ z \end{Bmatrix} \\
 &= \begin{Bmatrix} -\bar{\theta}(x \sin \Omega t + y \cos \Omega t) \\ \bar{\theta}(x \cos \Omega t - y \sin \Omega t) \\ -\bar{\psi}(x \cos \Omega t - y \sin \Omega t) + \bar{\varphi}(x \sin \Omega t + y \cos \Omega t) \end{Bmatrix} \quad (3.11) \\
 &= \begin{bmatrix} 0 & 0 & -x \sin \Omega t - y \cos \Omega t \\ 0 & 0 & x \cos \Omega t - y \sin \Omega t \\ x \sin \Omega t + y \cos \Omega t & -x \cos \Omega t + y \sin \Omega t & 0 \end{bmatrix} \begin{Bmatrix} \bar{\varphi} \\ \bar{\psi} \\ \bar{\theta} \end{Bmatrix} \\
 &= \mathbf{B}_0 \boldsymbol{\beta}.
 \end{aligned}$$

As a result, the augmented generalised coordinate vector reads

$$\mathbf{g} = \begin{Bmatrix} \mathbf{s} \\ \boldsymbol{\beta} \\ \boldsymbol{\rho} \\ \boldsymbol{\alpha} \\ \mathbf{r} \end{Bmatrix}, \quad (3.12)$$

and the governing matrix  $\mathbf{M}$  of the motions becomes

$$\mathbf{M} = \begin{bmatrix} \mathbf{I} & \mathbf{B}_0 & \mathbf{H} & \mathbf{H}\mathbf{A} & \mathbf{H} \end{bmatrix}. \quad (3.13)$$

The Lagrange equations are not rewritten in this particular case, but will be in the next sub-section, when applied to the finite element method.

### 3.2.2 Finite element coupling of stationary and rotating parts

Now that the basic mathematics related to the coupling between stationary and rotating parts have been established, it is of interest to apply it to the finite element formulation of the problem. In the fully coupled behavior presented before, the offset vector of the stationary part  $\boldsymbol{\rho}$  and the vector  $\boldsymbol{\beta}$  respectively produce the degrees of freedom of a node of the stationary part. As for the stationary part, the offset vector  $\boldsymbol{\rho}$  and the rotation vector  $\boldsymbol{\alpha}$  produce the degrees of freedom of a node of the rotating structure.

It is important to note that the rotation, in finite element, using Euler-Bernoulli 3D beams elements, is given via the type of element chosen and the discretisation of the studied structure. Consequently, the term  $\mathbf{A} \boldsymbol{\alpha}$  in the generalised coordinate vector of the rotating part should no longer be considered. In addition, the position of a mass located at a distance  $r$  from its center of rotation will never vary, therefore the term corresponding to  $\mathbf{H}\mathbf{r}$  in Eq.

3.1 will also cancel out. Therefore, the position vector of a rotating structural component with respect to a stationary component is written as

$$\bar{\mathbf{r}} = \mathbf{s} + \mathbf{B}\mathbf{H}\mathbf{r} + (\mathbf{I} + \mathbf{B})\mathbf{H}\boldsymbol{\rho}. \quad (3.14)$$

An energetic approach is adopted to identify the matrices on which time coupling takes place.

### 3.2.2.1 Potential energy

The potential energy of a structural system that undergoes elastic deformation reads

$$\mathcal{U} = \frac{1}{2} \int_V (\boldsymbol{\sigma}_0 + \boldsymbol{\sigma})^T (\boldsymbol{\epsilon} + \boldsymbol{\epsilon}_l) dV; \quad (3.15)$$

$$= \frac{1}{2} \int_V \boldsymbol{\sigma}_0^T \boldsymbol{\epsilon} + \boldsymbol{\sigma}_0^T \boldsymbol{\epsilon}_l + \boldsymbol{\sigma}^T \boldsymbol{\epsilon} + \boldsymbol{\sigma}^T \boldsymbol{\epsilon}_l dV, \quad (3.16)$$

where  $\boldsymbol{\sigma}_0$  and  $\boldsymbol{\epsilon}_l$  represent the initial stresses and large deformation due to the initial pre-stressed structure in rotation. The first and last products are ignored as they can be considered as second-order small quantities, having little impact on the finite element structure. Therefore, the potential energy reads

$$\mathcal{U} = \frac{1}{2} \int_V \boldsymbol{\sigma}_0^T \boldsymbol{\epsilon}_l dV + \frac{1}{2} \int_V \boldsymbol{\sigma}^T \boldsymbol{\epsilon} dV. \quad (3.17)$$

Assuming that the material used remains within its elastic deformation range, the link between the constraint and the deformation is established by the material matrix  $\mathbf{E}$ , which contains the Young's modulus and Poisson ratio relative to the material used. The second integral in Eq.3.17 represents the potential energy of the structure. By using the relationship between the nodal generalised displacement  $\boldsymbol{\epsilon} = \mathbf{B}\mathbf{g}$  and the relationship between strain and stress, the potential energy related to elastic deformation reads

$$\mathcal{U}_E = \frac{1}{2} \int_V \mathbf{g}^T \mathbf{B}^T \mathbf{E} \mathbf{B} \mathbf{g} dV. \quad (3.18)$$

As the aim is to build the Lagrange equation of motion in finite element formulation, the potential energy is derived with respect to the generalised coordinate

$$\frac{d\mathcal{U}_E}{d\mathbf{g}} = \int_V \mathbf{B}^T \mathbf{E} \mathbf{B} \mathbf{g} dV = \mathbf{K} \mathbf{g}. \quad (3.19)$$

This equation highlights the fact that no coupling in the elastic stiffness matrix takes place when taking into account the coupling between stationary and rotating parts.

The first term of Eq.3.17 corresponds to the potential energy of the structure due to initial stress. Initial stress comes from a pre-loading of the structure. In the case of a rotating structure, the initial stress comes from the pre-loading due to centrifugal force in the rotating frame of reference. As a result, it reads

$$\mathcal{U}_G = \frac{1}{2} \int_V (\boldsymbol{\sigma}_0^T \boldsymbol{\epsilon}_l) dV = \frac{1}{2} \int_V \mathbf{e}_l^T \boldsymbol{\sigma}_0 \mathbf{e}_l dV. \quad (3.20)$$

where  $\sigma_0$  contains the initial stress of the structure. The vector  $\mathbf{e}_l = \mathbf{B}\mathbf{g}$  contains the displacement via the derivative of the shape function. Therefore, the derivative of the initial stress-based potential energy yields

$$\frac{dU_G}{d\mathbf{g}} = \int_V \mathbf{B}'^T \sigma_0 \mathbf{B}' dV = \Omega^2 \mathbf{K}_G \mathbf{g}. \quad (3.21)$$

Like the elastic stiffness matrix, the geometric stiffness matrix contains no coupling between the rotating and static sub-structures.

### 3.2.3 Kinetic energy

The kinetic energy of a coupling of a structure undergoing a full coupling between stationary and rotating parts reads

$$\mathcal{T} = \frac{1}{2} \int_V \rho \dot{\mathbf{r}}^T \dot{\mathbf{r}} dV. \quad (3.22)$$

The expression of the displacement vector with respect to the stationary parts reads

$$\bar{\mathbf{r}} = \mathbf{s} + \mathbf{B}\mathbf{H}\mathbf{r} + (\mathbf{I} + \mathbf{B})\mathbf{H}\boldsymbol{\rho} + \mathbf{H}\mathbf{r}, \quad (3.23)$$

where the rotation of the rotating parts is neglected as the rotation is brought via the finite element discretization. In addition, it is assumed that the location vector  $\mathbf{r}$  is fixed and does not vary with respect to time. Therefore, the velocity vector reads

$$\dot{\bar{\mathbf{r}}} = \dot{\mathbf{s}} + \dot{\mathbf{B}}\mathbf{H}\mathbf{r} + \mathbf{B}\dot{\mathbf{H}}\mathbf{r} + \dot{\mathbf{H}}\boldsymbol{\rho} + \mathbf{I}\dot{\mathbf{H}}\boldsymbol{\rho} + \dot{\mathbf{B}}\mathbf{H}\boldsymbol{\rho} + \mathbf{B}\dot{\mathbf{H}}\boldsymbol{\rho} + \mathbf{B}\mathbf{H}\dot{\boldsymbol{\rho}} + \dot{\mathbf{H}}\mathbf{r}. \quad (3.24)$$

By using the relationship

$$\mathbf{B}\mathbf{H}\mathbf{r} = \mathbf{B}_0\boldsymbol{\beta}, \quad (3.25)$$

the governing coupling matrix then writes

$$\mathbf{M} = \begin{bmatrix} \mathbf{I} & \mathbf{B}_0 & \mathbf{H} \end{bmatrix}. \quad (3.26)$$

Therefore, the kinetic energy writes

$$\mathcal{T} = \frac{1}{2} m (\dot{\mathbf{g}}^T \mathbf{M}^T \mathbf{M} \dot{\mathbf{g}} + \mathbf{g}^T \dot{\mathbf{M}}^T \dot{\mathbf{M}} \mathbf{g} + 2\mathbf{g}^T \dot{\mathbf{M}}^T \mathbf{M} \dot{\mathbf{g}}). \quad (3.27)$$

However, a finite element approach to the problem is being formulated. Consequently, in the finite element formulation, mass  $m$  is replaced by density  $\rho$ , and the generalised coordinate vector  $\mathbf{g}$  is expressed as a function of the shape functions matrix  $\mathbf{N}$ , which depend solely on space variable, and the nodal displacement vector  $\mathbf{u}(t)$ , which depends on time. Therefore, the kinetic energy in finite element formulation with coupling matrices writes

$$\mathcal{T} = \frac{1}{2} \rho \int_V \mathbf{N}^T \dot{\mathbf{u}}^T \mathbf{M}^T \mathbf{M} \mathbf{N} \dot{\mathbf{u}} + \mathbf{N}^T \mathbf{u} \dot{\mathbf{M}}^T \dot{\mathbf{M}} \mathbf{N} \mathbf{u} + 2\mathbf{N}^T \mathbf{u} \dot{\mathbf{M}}^T \mathbf{M} \mathbf{N} \dot{\mathbf{u}} dV. \quad (3.28)$$

Analysing the previous equation, different characteristic matrix expressions can be identified. In fact, the first term corresponds to the mass matrix expression in finite element while having added a coupling product to its formulation. The second term corresponds to the coupled formulation of the centrifugal stiffness matrix. Finally, the last term corresponds to the coupled formulation of the gyroscopic matrix.

Therefore, it is concluded that a coupling only originates, in a floating frame of reference formulation, in the mass matrix, centrifugal stiffness matrix, and gyroscopic matrix.

### 3.2.3.1 Lagrange equation of motion

Making use of all the previously established relationships, it is possible to derive the Lagrange equation of motion for the fully coupled case. The equation is not written in finite element formulation, so as to have a more readable solution and to highlight the coupling matrices. To obtain the finite element formulation of the equation, the mass  $m$  must be replaced by the density and the volume of the element studied. Therefore the Lagrange equation of motion reads, in the fully coupled case,

$$m \begin{bmatrix} \mathbf{I} & \mathbf{B}_0 & \mathbf{H} \\ \mathbf{B}_0^T & \mathbf{B}_0^T \mathbf{B}_0 & \mathbf{B}_0^T \mathbf{H} \\ \mathbf{H}^T & \mathbf{H}^T \mathbf{B}_0 & \mathbf{I} \end{bmatrix} \begin{Bmatrix} \ddot{\mathbf{s}} \\ \ddot{\boldsymbol{\beta}} \\ \ddot{\boldsymbol{\rho}} \end{Bmatrix} + 2m\Omega \begin{bmatrix} \mathbf{0} & \bar{\mathbf{B}}_0 & \bar{\mathbf{H}} \\ \mathbf{0} & \mathbf{B}_0^T \bar{\mathbf{B}}_0 & \mathbf{B}_0^T \bar{\mathbf{H}} \\ \mathbf{0} & \mathbf{H}^T \bar{\mathbf{B}}_0 & \mathbf{H}^T \bar{\mathbf{H}} \end{bmatrix} \begin{Bmatrix} \dot{\mathbf{s}} \\ \dot{\boldsymbol{\beta}} \\ \dot{\boldsymbol{\rho}} \end{Bmatrix} + m\Omega^2 \begin{bmatrix} \mathbf{0} & \bar{\bar{\mathbf{B}}}_0 & \bar{\bar{\mathbf{H}}} \\ \mathbf{0} & \mathbf{B}_0^T \bar{\bar{\mathbf{B}}}_0 & \mathbf{B}_0^T \bar{\bar{\mathbf{H}}} \\ \mathbf{0} & \mathbf{H}^T \bar{\bar{\mathbf{B}}}_0 & \mathbf{H}^T \bar{\bar{\mathbf{H}}} \end{bmatrix} \begin{Bmatrix} \mathbf{s} \\ \boldsymbol{\beta} \\ \boldsymbol{\rho} \end{Bmatrix} = \begin{Bmatrix} -m\bar{\bar{\mathbf{H}}}\mathbf{r} \\ -m\mathbf{B}_0^T \bar{\bar{\mathbf{H}}}\mathbf{r} \\ \mathbf{f}_\rho \end{Bmatrix}, \quad (3.29)$$

where the different component in the vector on the right-hand side of the equation corresponds to the various forces applying to the system under study. The first force is an unbalanced force, the second one corresponds to a Coriolis force and the third one being the centrifugal force.

## 3.3 Numerical implementation of the coupling between stationary and rotating parts

### 3.3.1 General considerations

The main difficulty of this thesis, in addition to the understanding of the phenomena involved, is the implementation of the coupling between stationary and rotating parts of the structure. To simplify the explanation of the numerical implementation of the coupling, one defines the different sub-structures that can be encountered. The different sub-structures that can be encountered are

- the stationary structure;
- the hub;
- the rotating structure(s).

The stationary consist of a structure composing the global structure. For a wing propeller system, the wing would be the stationary structure. The hub is the attachment point of the rotating structures. The hub is the stationary part of the coupling in the previous section. Finally, the rotating structures are the structure rotating and mechanically linked to the hub. In the present study, the rotating structures are not linked to each others anywhere other than at the hub node. Therefore, the dynamics of each of the rotating structures cannot influence the dynamics of the other rotating structure except at the hub node. A schematic of the implementation to derive the equations of motion is represented in Figure 3.2.

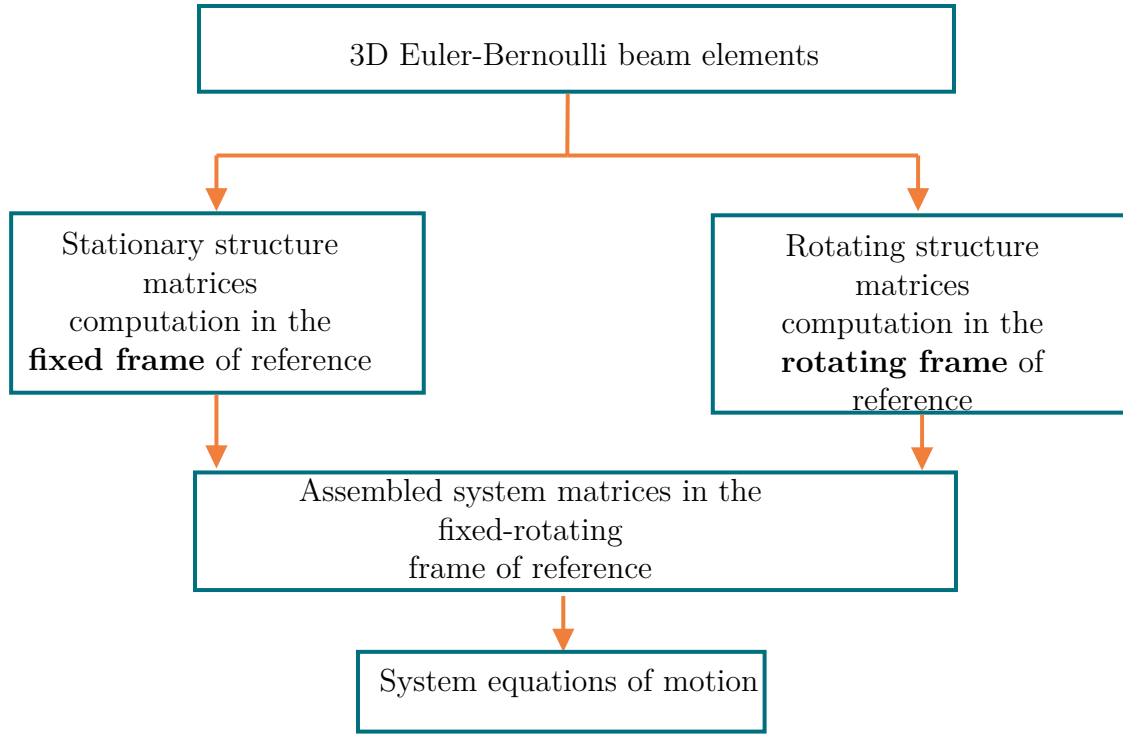


FIGURE 3.2 – Schematic of the implementation to derive the equation of motion. Partially reproduced from Zuo et al [39].

### 3.3.2 Time coupling implementation and assembly strategy

The formulation of the coupling between stationary and rotating parts is well established when dealing with particle of mass  $m$ . However, concerning its finite element formulation and especially its implementation and the matrices assembly, it is a void. A representation of an assembled structural matrix constituting the equation of motion of the studied system is represented in Figure 3.3. Analysis of the Figure 3.3 reveals the coupling between the rotor hub and the rotating structures, as well as the coupling between the rotating structure and the rotor hub. All this shows that the coupling only affects the rotating system and not the stationary structure.

It is important to pay attention to a few details: The different coupling matrices are expressed in the rotating frame of reference. However, the different matrices are computed at the element level. Therefore, the different coupling matrices must be transformed to the element frame of reference via the transformation matrix  $\mathbf{R}_e$  before being used to build the finite element elementary matrices. The transformation of the different coupling matrices is used to take into account the phase shift between each rotating part. This phase shift between each rotating part is important and must be respected in order to correctly represent the physics of the system under study. An algorithm presenting an implementation of the coupling is available in Appendix F.

Looking at the different boundary conditions, in the rotating frame of reference, the rotating elements are clamped to the hub. In addition, in the fixed frame of reference, the studied structure also has its own boundary conditions, influencing the assembly of the different matrices. Finally, the addition of the mass in rotation to the corresponding degree

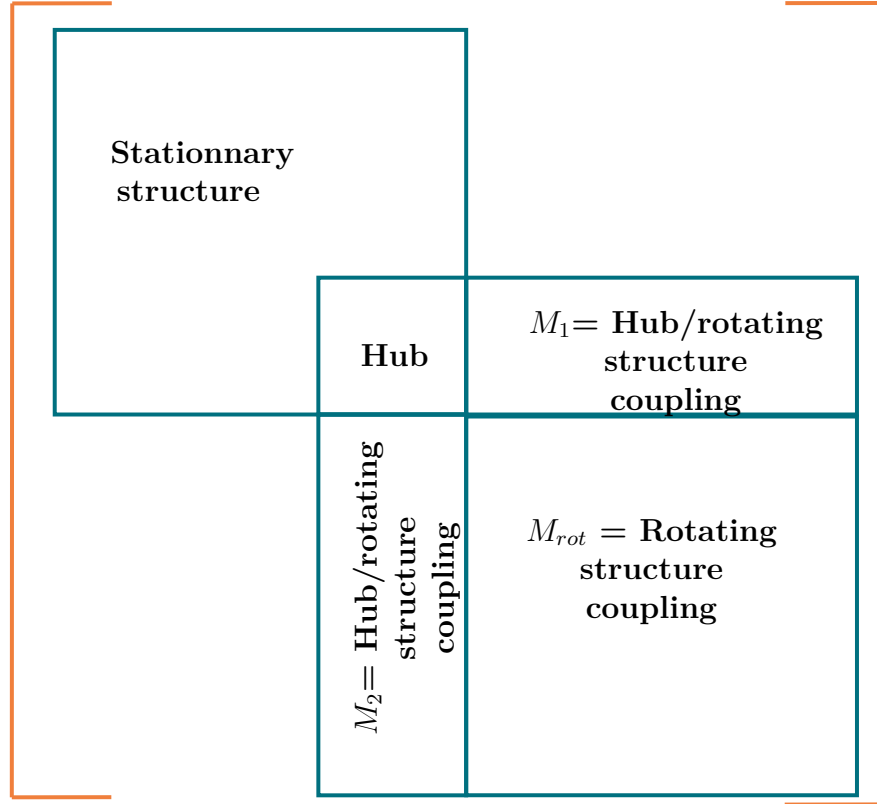


FIGURE 3.3 – Representation of a structural matrix undergoing time coupling between the rotating structure and the hub. The different rows and columns (not represented) of the matrix represents the different degrees of freedom of the complete structure.

of freedom of the hub, in the fixed-rotating frame of reference must be accomplished to fully take into account the physical phenomena. This addition of mass must be made. If this is not achieved, the system dynamics obtained will be incorrect. This must be done when using partial coupling, i.e. when only the translational degrees of freedom of the rotating structures are coupled with those of the hub, but also when the full coupling is performed, i.e. when the translational degrees of freedom of the rotating structure are also coupled with the rotational degrees of freedom of the hub. When a full coupling is used, the inertia of the rotating structures must be added to the rotational degrees of freedom of the hub in order to correctly represent the physics of the problem.

### 3.4 Validation of the coupling

The aim now is to validate this mechanical coupling and to validate the time integration scheme employed. In order to achieve this, a validation of the temporal integration on a Ground resonance (GR) model is proposed for a rigid model but also offering temporal coupling. Subsequently, the mechanical coupling is also validated on a GR model but with the finite element method by applying the procedure presented previously. Furthermore, a validation of the unbalanced force is proposed. Finally, an attempt to validate the complete time coupling is carried out.



### 3.4.1 Coupling validation model: Ground resonance model

In the first instance, the aim is to partially validate the coupled finite element model established previously. The coupling is tested on a ground resonance model established by Hammond et al [62]. The studied model is represented in Figure 3.4.

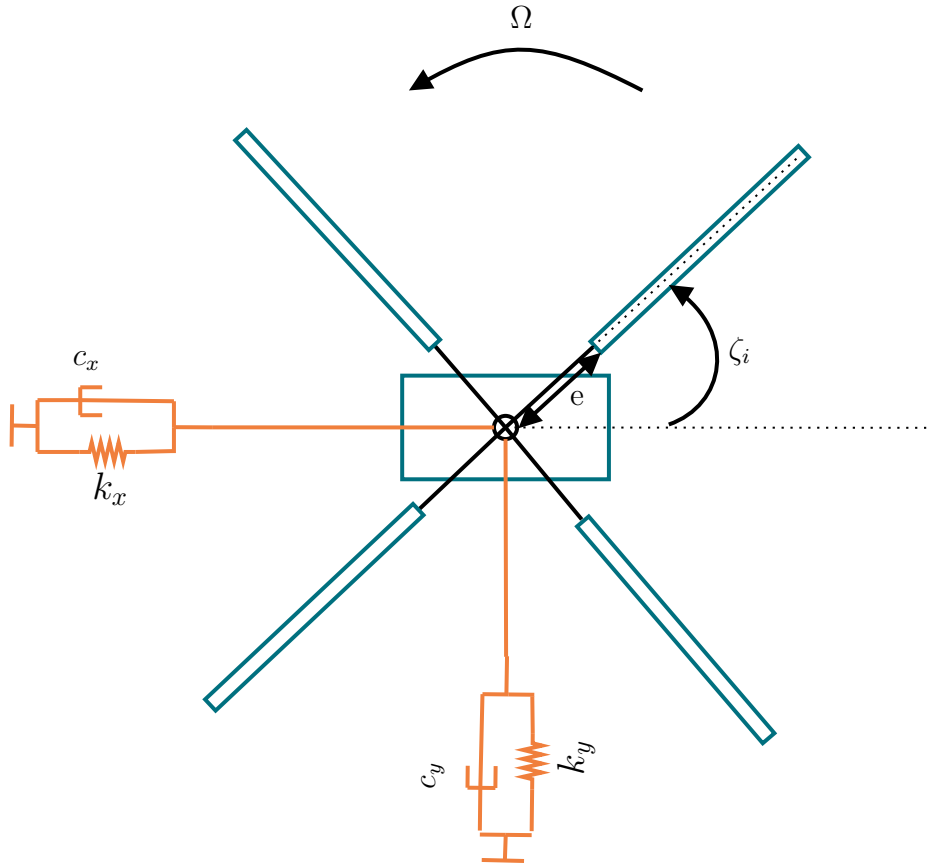


FIGURE 3.4 – Validation case: Ground resonance model. Reproduced from Hammond et al [62].

The different parameters used to perform the validation are available in Table 3.1.

<i>Parameter</i>	<i>Value</i>	<i>Units</i>
Number of blade $N$	4	-
Rotor radius $R$	5.64	m
Operational rotor speed $\Omega_0$	31.42	rads <sup>-1</sup>
Blade mass $m_b$	94.9	kg
Blade mass moment $S_b$	281.1	kg m
Blade mass moment of inertia $I_b$	1084.7	kg m <sup>2</sup>
Lag hinge offset $e$	0.3048	m
Longitudinal hub mass $M_x$	8026.6	kg
Lateral hub mass $M_y$	3283.6	kg
Longitudinal hub spring $k_x$	1240481.08	N/m
Lateral hub spring $k_y$	1240481.08	N/m
Lag damper $c_b$	4067.5	mNs/rad

TABLE 3.1 – Ground resonance model parameters (Hammond et al [62]).

### 3.4.1.1 Rigid model

A rigid model has already been developed by former student Sviatoslav Tezikov [63]. In his work, a rigid model is studied which does not take into account the deformation of the helicopter blades and therefore their potential impact on the stability of the system under study. The equations governing the motions of such a system have been derived by Hammond [62] and read

$$\begin{aligned}
(m_x + Nm_b)\ddot{x}_h + c_x\dot{x}_h + k_x x_h &= S_b \sum_{i=1}^N \left[ (\ddot{\zeta}_i - \Omega^2 \zeta_i) \sin \psi_i + 2\Omega \dot{\zeta}_i \cos \psi_i \right]; \\
(m_y + Nm_b)\ddot{y}_h + c_y\dot{y}_h + k_y y_h &= -S_b \sum_{i=1}^N \left[ (\ddot{\zeta}_i - \Omega^2 \zeta_i) \cos \psi_i - 2\Omega \dot{\zeta}_i \sin \psi_i \right].
\end{aligned}$$

This system of equations consists of  $N+2$  differential equations which are coupled. The periodic coefficient arise because the blades equations are developed in a rotating frame of reference whereas the hub equations are developed in a fixed frame of reference. An alternative consist of writing the hub equations of motion in the rotating frame of reference. The equations thus read:

$$\begin{aligned}
\ddot{\bar{x}} + \eta_h \dot{\bar{x}} + (\omega_h^2 - \Omega^2)\bar{x} - 2\Omega \dot{\bar{y}} - \Omega \eta_h \bar{y} &= \nu_h^2 \sum_{j=1}^N \left[ (\zeta_j - \Omega^2 \zeta_j) \sin \frac{2\pi}{N}(j-1) + 2\Omega \zeta_j \cos \frac{2\pi}{N}(j-1) \right]; \\
\ddot{\bar{y}} + \eta_h \dot{\bar{y}} + (\omega_h^2 - \Omega^2)\bar{y} + 2\Omega \dot{\bar{x}} + \Omega \eta_h \bar{x} &= -\nu_h^2 \sum_{j=1}^N \left[ (\zeta_j - \Omega^2 \zeta_j) \cos \frac{2\pi}{N}(j-1) - 2\Omega \zeta_j \sin \frac{2\pi}{N}(j-1) \right],
\end{aligned}$$

where the bar notation refers to the global frame of reference and where the following parameters have been introduced

$$\begin{aligned}\nu_h^2 &= \frac{S_b}{m_x + Nm_b}; \\ \omega_h^2 &= \frac{k_x}{m_x + Nm_b}; \\ \eta_h &= \frac{c_x}{m_x + Nm_b}.\end{aligned}$$

### 3.4.1.2 Validation of the different numerical schemes

Again intending to validate the various tools used in the validation of the different finite element models, it seeks to validate the numerical integration schemes employed. To achieve this, the various previously presented numerical schemes are tested and compared to results available in the literature. The different results obtained with the various numerical schemes are highlighted in Figure 3.5, Figure 3.6, Figure 3.7 and Figure 3.8.

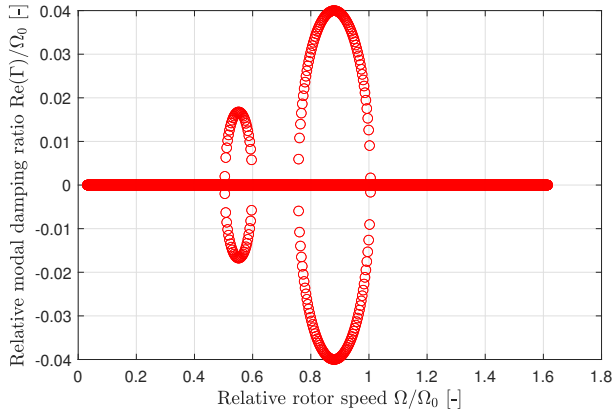


FIGURE 3.5 – Relative modal damping ratio obtained using Newmark integration scheme using rigid model.

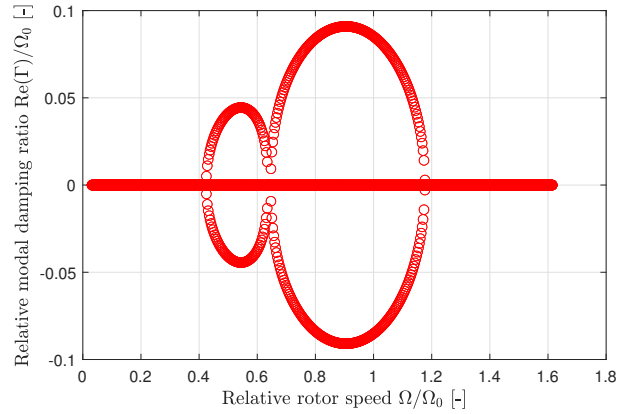


FIGURE 3.6 – Relative modal damping ratio obtained using Runge-Kutta integration scheme using rigid model.

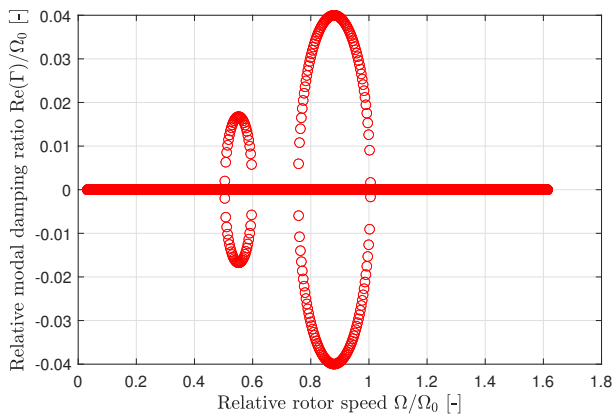


FIGURE 3.7 – Relative modal damping ratio obtained using Newmark V2 integration scheme using rigid model.

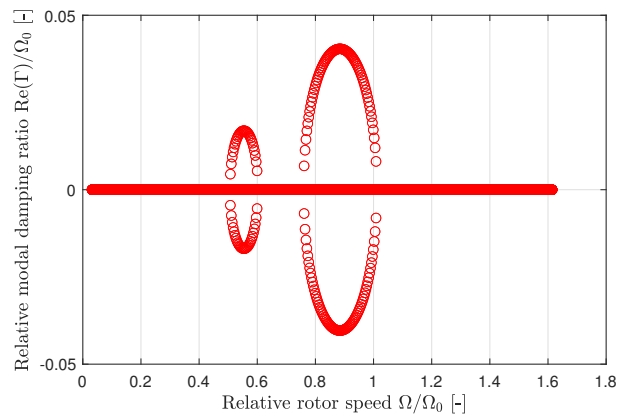


FIGURE 3.8 – Relative modal damping ratio obtained using  $\alpha$  generalised integration scheme using rigid model.

The different numerical schemes employed provide results in agreement with results presented by Ignacio et al in [64]. The different results are obtained neglecting the external damping on the hub  $c_x$  and  $c_y$  and the blade damping  $c_b$ , but taking into account the coupling term corresponding to the gyroscopic term. However, one can observe that the results obtained using the Runge-Kutta integration scheme are quite different from the ones obtained using the Newmark integration scheme. In fact, the zone of instability which corresponds to a positive modal damping is larger than the zone of instability obtained using the Newmark integration scheme. In addition, the Newmark integration scheme detects two zones of instability, each separated by a stability zone. These results seem to be more in accordance with results obtained in the literature. The difference in the instability zone is probably coming from the particularity of the different integration schemes. In fact, the Runge-Kutta integration scheme employs a variable time step to limit the relative error between two integration steps whereas the Newmark integration scheme employs a constant time step. The results obtained using  $\alpha$  generalised numerical scheme are a bit higher than the one obtained using Newmark numerical scheme but this is due to the fact that the spectral radius is taken into in the computation of the value of the parameter  $\beta$  and  $\gamma$  of the scheme, which makes them different from the one of the Newmark scheme.

Although Floquet theory and the analysis of Floquet exponents have enabled us to conclude whether the rigid model under study is stable or not, it is interesting to study the behavior of the dynamic system under study at a speed of rotation concluded by Floquet theory to be stable or unstable. To do so, the Newmark integration scheme is employed using as an initial condition an initial displacement, over one blade, of 0.001 m and no initial velocity. Figure 3.9 and Figure 3.11 each represent the movement in the  $x$  and  $y$  degrees of freedom plane of the hub. It can be seen that when the rigid system is rotated at a speed of 3 rad/s, which is a stable speed according to Floquet theory, the movement remains bounded around its equilibrium position, which is confirmed by analyzing the movement over ten periods of revolutions (Figure 3.10), whereas when this system is rotated at a speed of rotation said to be unstable by Floquet's theory, it can be seen that the hub's movement is not bounded and could lead to its destruction if operated at this speed of rotation. This critical behavior is visible when looking at Figure 3.12, when the movement of the hub is studied over ten periods of revolution of the propeller.

Now that the time integration has been validated for the rigid model without damping, it is of interest to analyse the behavior of the GR model when damping is present on the various blades and when the hub has isotropic damping. Figure 3.13 and Figure 3.14 highlights the behavior of the system when taking into account the damping acting on the blade but also on the hub. Results highlights an unconditional stability stability of the system. In addition, the obtained results are in accordance with results obtained in the literature by [62]. It is clear that the results obtained are not the same but this is due to the fact that the integration scheme is not the same and that the relative error and absolute error can be controlled when using Runge-Kutta integration scheme, which is not the case when using the Newmark scheme.

To illustrate the stable behavior predicted by Floquet exponents, one can also analyse the behavior of the displacement of the system when subject to an unitary displacement on the hub in the  $x$  direction. The behavior obtained when using Newmark integration scheme

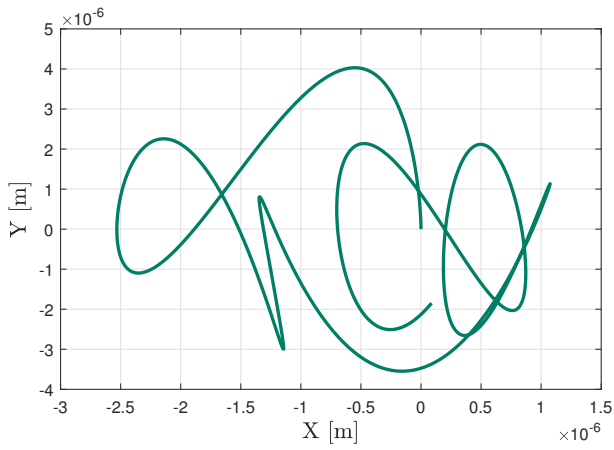


FIGURE 3.9 – Hub displacement over one period of revolution when rotor rotating at  $\Omega = 3$  rad/s.

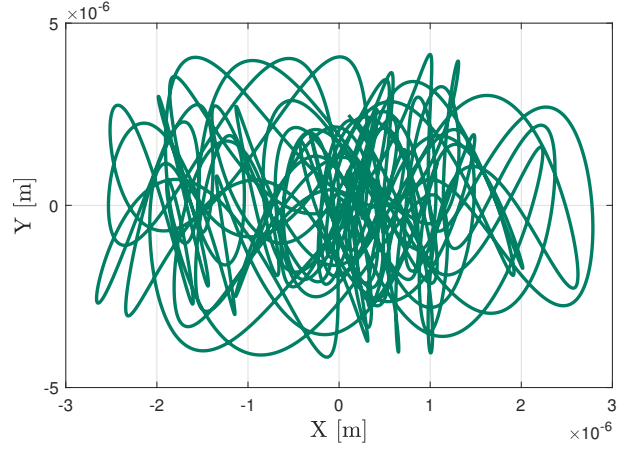


FIGURE 3.10 – Hub displacement over ten periods of revolution when rotor rotating at  $\Omega = 3$  rad/s

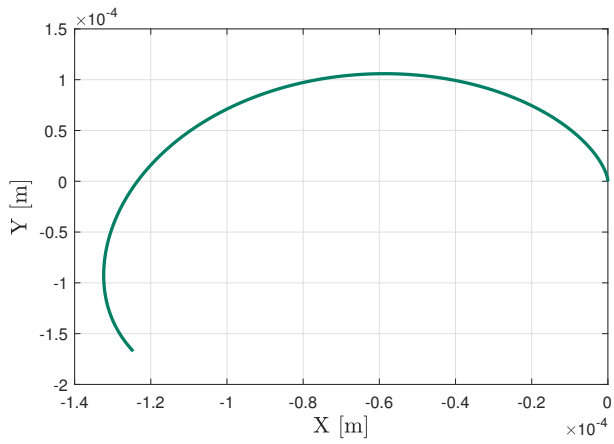


FIGURE 3.11 – Hub displacement over one period of revolution when rotor rotating at  $\Omega = 30$  rad/s.

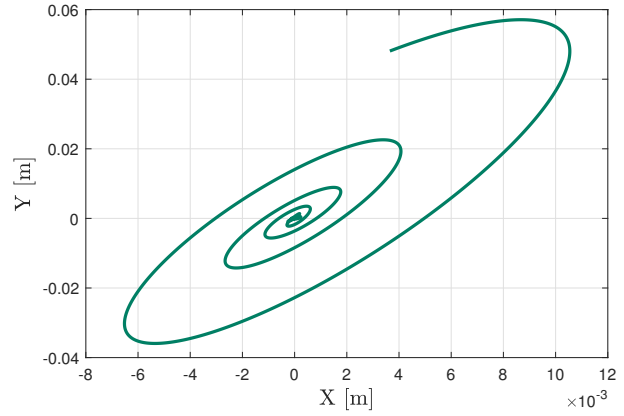


FIGURE 3.12 – Hub displacement over ten periods of revolution when rotor rotating at  $\Omega = 30$  rad/s

are highlighted in Figure 3.15.

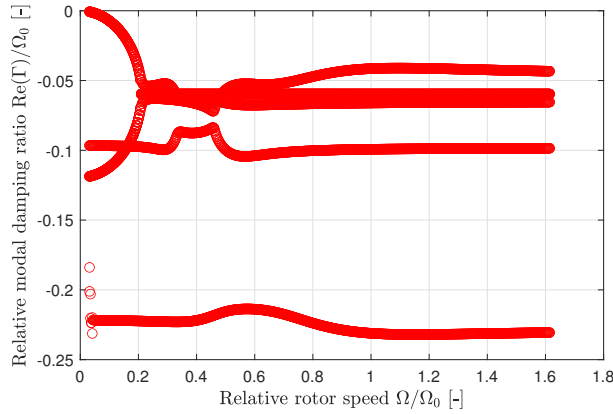


FIGURE 3.13 – Relative modal damping ratio obtained using Newmark integration scheme using rigid model with dampers acting on the hub and on the different blades.

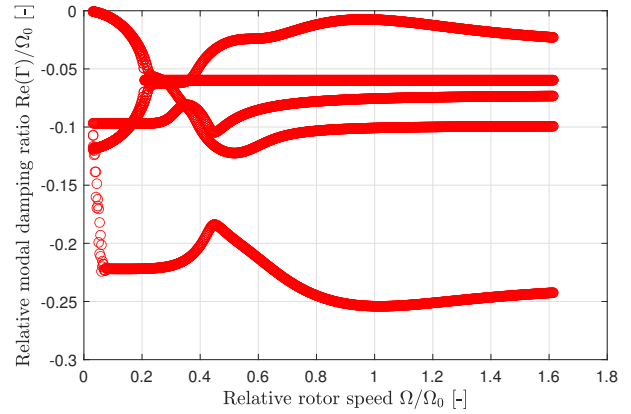


FIGURE 3.14 – Relative modal damping ratio obtained using Runge-Kutta integration scheme using rigid model with dampers acting on the hub and on the different blades.

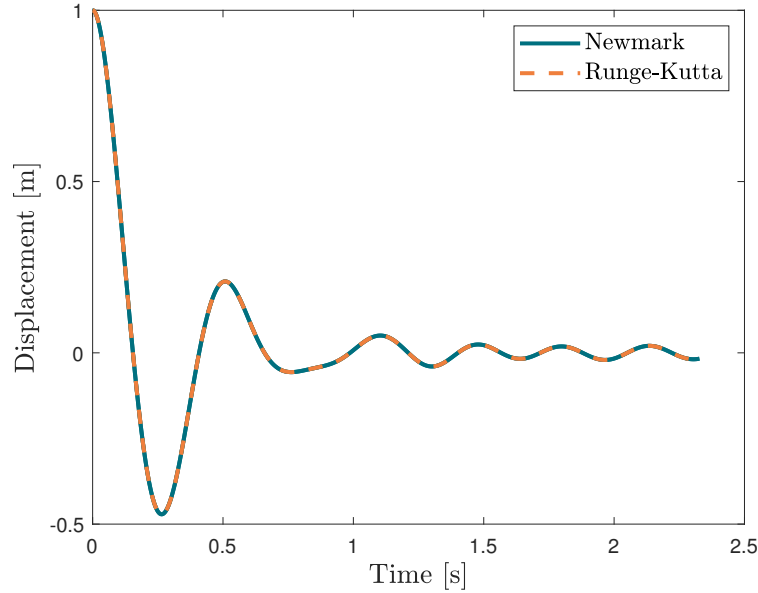


FIGURE 3.15 – Displacement of the hub in the  $X$  direction for an initial displacement of 1m on the hub in the  $X$  direction. Comparison between the Newmark integration scheme and Runge-Kutta integration scheme.

### 3.4.1.3 Finite element model

Now that the different results characterising the ground resonance model have been established for the rigid problem, the finite element implementation is studied. To get as close as possible to the rigid model, partial coupling is used. In other words, we will only consider a coupling between the degrees of freedom in translation of the elements located on each of the blades and those of the hub, and vice versa. Consequently, the coupling terms on the rotational degrees of freedom of the hub, which is the static part, are neglected. Consequently, the Lagrange equation characterising the dynamics of the system in the fixed-rotating frame of reference reads:

$$m \begin{bmatrix} \mathbf{I} & \mathbf{H} \\ \mathbf{H}^T & \mathbf{I} \end{bmatrix} \begin{Bmatrix} \ddot{\boldsymbol{\sigma}} \\ \ddot{\boldsymbol{\rho}} \end{Bmatrix} + 2m\Omega \begin{bmatrix} \mathbf{0} & \bar{\bar{\mathbf{H}}} \\ \mathbf{0} & \mathbf{H}^T \bar{\bar{\mathbf{H}}} \end{bmatrix} \begin{Bmatrix} \dot{\boldsymbol{\sigma}} \\ \dot{\boldsymbol{\rho}} \end{Bmatrix} + m\Omega^2 \begin{bmatrix} \mathbf{0} & \bar{\bar{\mathbf{H}}} \\ \mathbf{0} & \mathbf{H}^T \bar{\bar{\mathbf{H}}} \end{bmatrix} \begin{Bmatrix} \boldsymbol{\sigma} \\ \boldsymbol{\rho} \end{Bmatrix} = \begin{Bmatrix} -m\bar{\bar{\mathbf{H}}}\mathbf{r} \\ \mathbf{f}_\rho \end{Bmatrix}. \quad (3.30)$$

To get as close as the rigid model, an equivalent beam model is used. The different material and beam properties are highlighted in Table 3.2. The properties of the fuselage remain unchanged.

<i>Parameter</i>	<i>Value</i>	<i>Units</i>
Number of blade $N$	4	-
Rotor radius $R$	5.64	m
Operational rotor speed $\Omega_0$	31.42	rads <sup>-1</sup>
Beam diameter $D$	0.026	m
Young modulus	210	GPa
Density	7800	kgm <sup>3</sup>
Poisson coefficient	0.3	-

TABLE 3.2 – Ground resonance equivalent model parameters for finite element formulation of the problem.

The aim of this subsection is therefore to validate the implementation of the partial coupling via comparing the obtained results with the one obtained with the rigid model, keeping in mind that the previously obtained results are the obtained under the assumption of a rigid model, therefore neglecting a large part of the dynamics of the system under study and its stability.

When different numerical integration schemes are used with the finite element model, the results obtained are not always consistent. The use of the Newmark integration scheme indeed leads to different solutions than the Runge-Kutta integration scheme. Observing the modal damping ratio behavior with the Newmark scheme for the undamped case in Figure 3.16, one can notice that for relative rotor speeds greater than 0.3 the system is unstable with very large modal damping ratio values that make very little physical sense. The Runge-Kutta integration scheme, on the other hand, predicts total system stability over the speed range tested in Figure 3.17. In fact, all the relative modal damping ratios have a negative real part, which allows to conclude that the system studied is stable. The values obtained for the modal damping are all negative but all very close to zero. Since it is the undamped case that is being studied, these values are due to numerical noise introduced by the Runge-Kutta integration scheme.

Looking at the results obtained for the damped case in Figure 3.18 and Figure 3.19, one can remark that the solution obtained for the damped is similar as the one obtained for the undamped case, meaning that the system is unstable even when damping is introduced in the system. Furthermore, Figure 3.19 highlights similar stability conclusion as the results obtained with the rigid model, with the difference that now the different blades can deform in the finite element model. One can see that the different relative modal damping of the different blades coincides. This result is not surprising as the different blades all have the

same material properties ,are modeled using the same number of element on each blades and the different blades are connected via a same node (the hub) which is also an assumption made in this study.

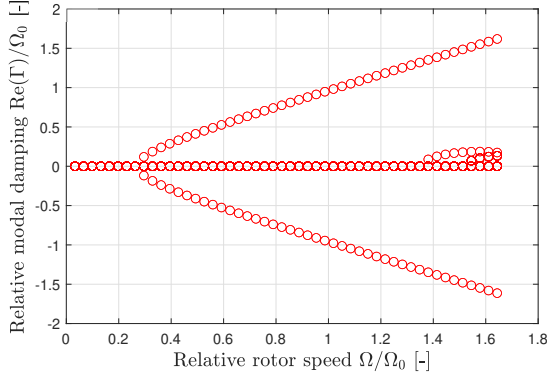


FIGURE 3.16 – Relative modal damping for the undamped case using Newmark integration scheme.

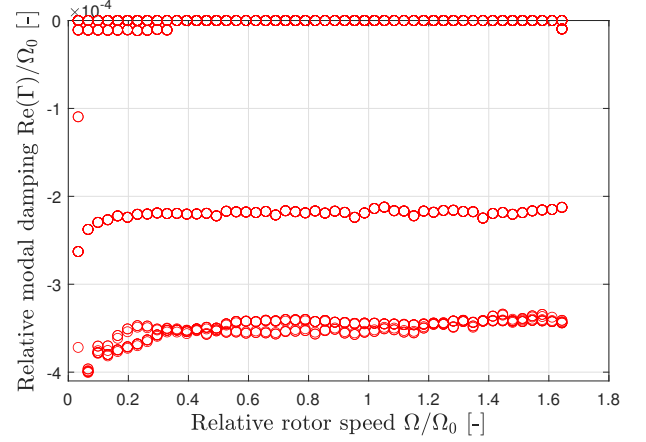


FIGURE 3.17 – Relative modal damping for the undamped case using the Runge-Kutta integration scheme.

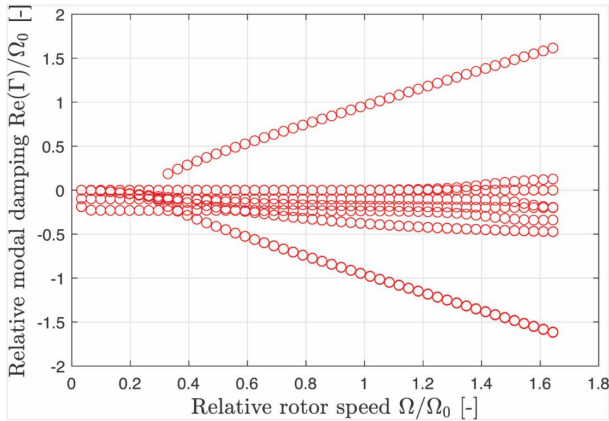


FIGURE 3.18 – Relative modal damping for the damped case using Newmark integration scheme.

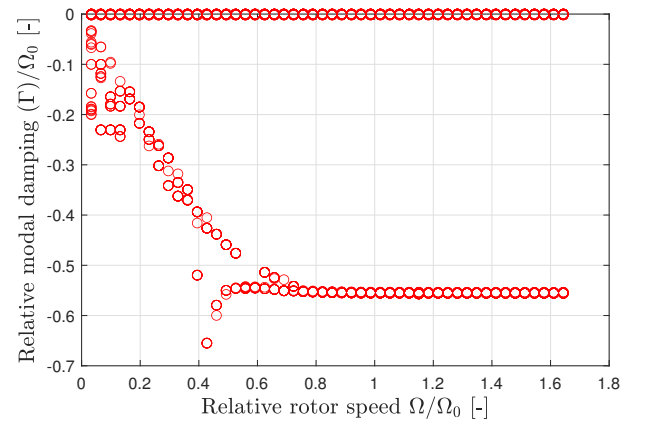


FIGURE 3.19 – Relative modal damping for the damped case using the Runge-Kutta integration scheme.

A further way of supporting the validation of the partial coupling is to observe the imaginary part of gamma as a function of relative rotor speed when using the implemented finite element model and compare this with the rigid model. Figure 3.20 and Figure 3.21 both show similar behavior. The different points in each mode are not connected to keep the different graphs legible. The behavior of the two models is similar, although more modes are present with the finite element model because the number of degrees of freedom is greater with the finite element model. In addition, there are more crossings with the 0 axis in the case of the finite element model compared to the rigid model. The crossings with the 0 axis, i.e. going from an imaginary part which is positive to negative and vice versa, correspond to a transition from one type of oscillation to another. There are more crossings with the 0 axis when using the finite element model. This is due to the fact that the finite element model describe the studied structure more accurately. This increase in



the number of modes can therefore lead to more complex and more frequent interactions between modes, resulting in a greater number of transitions (sign changes) in the imaginary part of  $\Gamma$ .

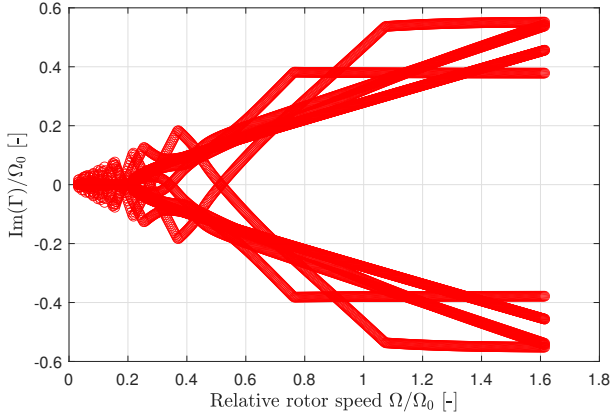


FIGURE 3.20 – Evolution of the imaginary part of  $\Gamma$  as a function of the rotor speed for the damped case using the rigid model.

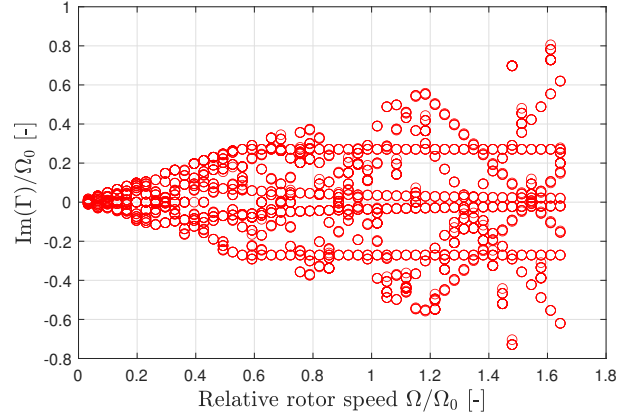


FIGURE 3.21 – Evolution of the imaginary part of  $\Gamma$  as a function of the rotor speed for the damped case using the finite element model.

One might question the fact that the results obtained with Runge-Kutta predict a stability of the system studied using the finite element model. However, this result is not surprising at all when knowing that taking into account the flexibility of both the rotating and static parts improves the stability prediction of the system studied. The results obtained using Runge-Kutta integration scheme with the finite element model are produced after conducting an relative error sensitivity of the results. In fact, the numerical scheme is resolved for a rotation speed being unstable in the rigid case. In this case, a rotation speed of 27 rad/s is selected. The numerical scheme is computed using an initial unit displacement on the hub along the  $X$  direction and the response of the first blade at the tip along the  $Y$  direction is observed. The results obtained for the undamped case are highlight in Figure 3.22 and in Figure 3.23.

It is clearly visible that admitting a relative error too large leads to an unstable system response but as soon that the relative error decrease to  $10^{-2}$  %, the undamped system remains stable following the unit solicitation on the hub. The main problem with the Runge-Kutta integration scheme is its computational cost. In fact, as all the structural matrices have to be computed by solving the integral defining them, the number of integration that must be undertaken is very large and so as the computational cost associated to this computation (Figure 3.24). The CPU time is obviously lower than the real time taken to compute the different solution at the different relative rotor speed as it is only the time during which the CPU was used to do computation. Therefore, the following computation using Runge-Kutta integration scheme will be done using a relative error of  $10^{-6}$  % which is a compromise between precision and computational time.

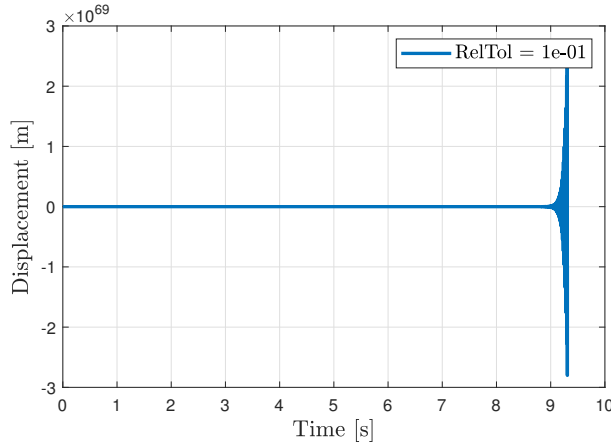


FIGURE 3.22 – Relative error analysis using Runge-Kutta integration scheme for the undamped. Comparing the displacement in the Y direction at the tip of blade n°1 at  $\Omega = 27$  rad/s.

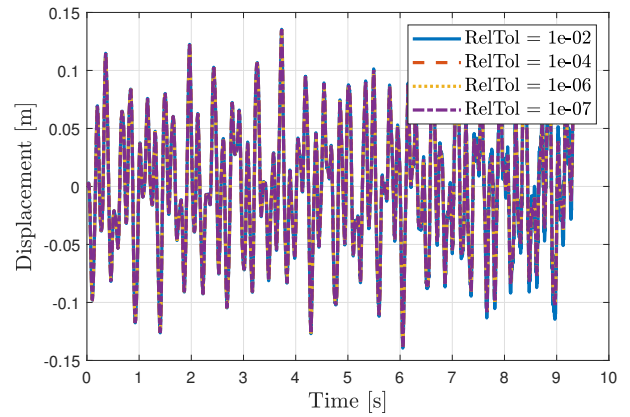


FIGURE 3.23 – Relative error analysis using Runge-Kutta integration scheme for the undamped case. Comparing the displacement in the Y direction at the tip of blade n°1 at  $\Omega = 27$  rad/s for different relative error.

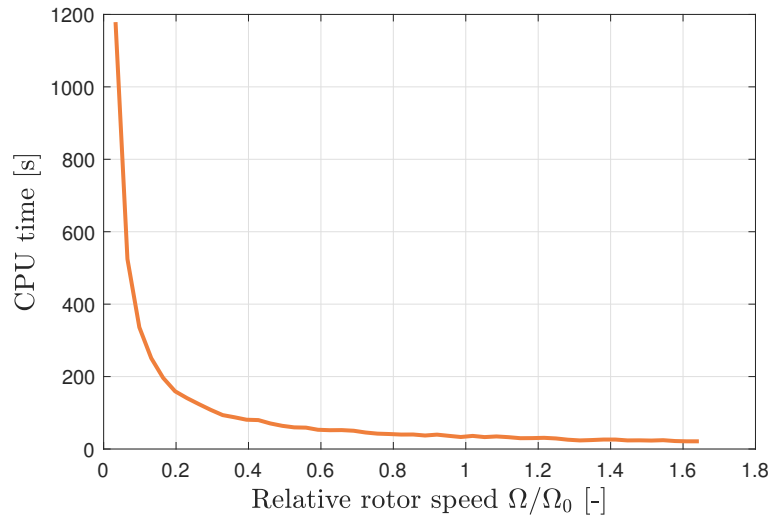


FIGURE 3.24 – CPU time for the computation of the undamped case using Runge-Kutta integration scheme.

When using the Newmark integration scheme, a similar analysis as the one performed using Runge-Kutta can be performed. As the Newmark integration scheme uses a constant time step, to achieve a consistent analysis, it is of interest to perform an analysis over the number of steps in which it is desired to fragment the time interval of the period of revolution.

The results in Figure 3.25 and Figure 3.26 show a total divergence of the response of the system to a step increment on the hub in the X-direction whether with the undamped model or the damped model. This results is totally surprising as it does not agree with what is observed when using Runge-Kutta integration scheme. In fact, taking into account the blades deformation can deform should increase the stability of the studied system compared to the rigid solution. There are several potential reasons to explain this divergence in results

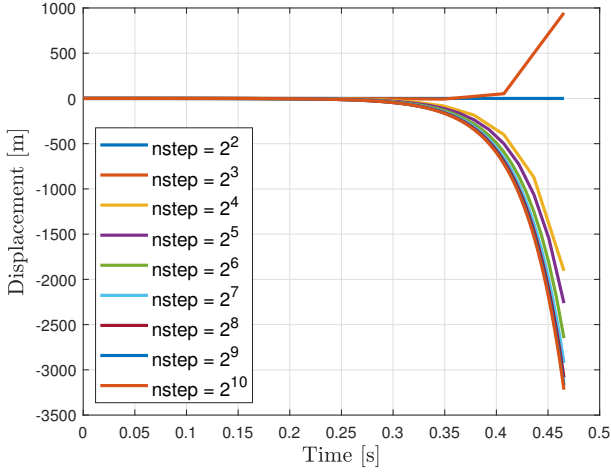


FIGURE 3.25 – Displacement of the first blade after a unit initial displacement on the hub along  $X$  direction for an undamped system. Comparison between different discretisation of the time interval.

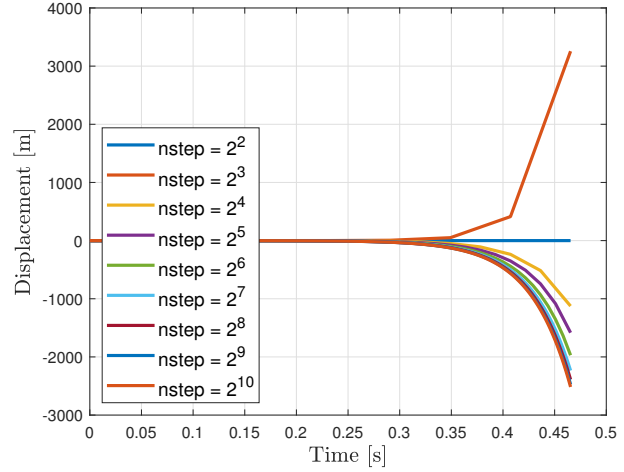


FIGURE 3.26 – Displacement of the first blade after a unit initial displacement on the hub along  $X$  direction for a damped system. Comparison between different discretisation of the time interval.

compared to the one obtained with the rigid model:

- The Newmark scheme may not be sufficiently stable or suitable, especially for systems with high modal frequencies or non-linear behavior.
- The conditioning of the resulting matrices following numerical coupling may also partly explain this discrepancy in the results obtained with the Newmark integration scheme.

As a result, it can be concluded that the Newmark integration scheme is not suitable to be used when studying the stability of linear time periodic system with the finite element method.

### 3.4.2 Coupling validation model: Rotating shaft

The next structure being studied with the aim to validate the previously established finite element model is a rotating shaft composed of a rotating shaft and four blades attached at its center. The studied structure is represented in Figure 3.27.

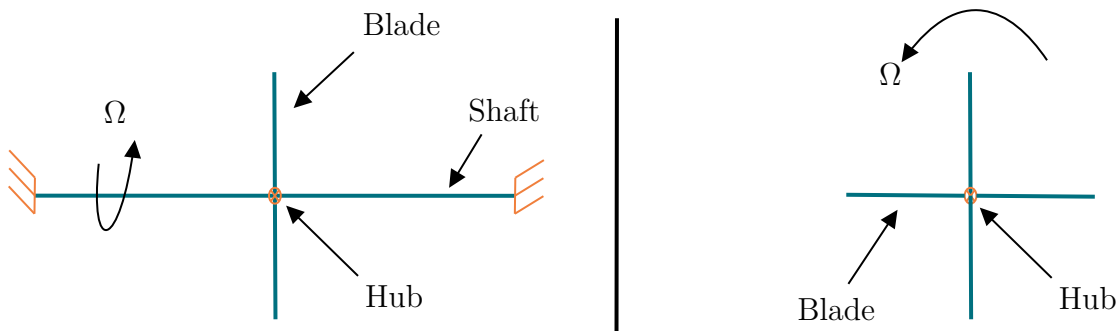


FIGURE 3.27 – Schematic of the rotating shaft. Left side - side view. Right side - front view.

This final model consists at validating the complete coupling between stationary and rotating structures. In this case, the Lagrange equations of motion reads

$$\begin{aligned}
 m \begin{bmatrix} \mathbf{I} & \mathbf{B}_0 & \mathbf{H} \\ \mathbf{B}_0^T & \mathbf{B}_0^T \mathbf{B}_0 & \mathbf{B}_0^T \mathbf{H} \\ \mathbf{H}^T & \mathbf{H}^T \mathbf{B}_0 & \mathbf{I} \end{bmatrix} \begin{Bmatrix} \ddot{\mathbf{s}} \\ \ddot{\boldsymbol{\beta}} \\ \ddot{\boldsymbol{\rho}} \end{Bmatrix} + 2m\Omega \begin{bmatrix} \mathbf{0} & \bar{\mathbf{B}}_0 & \bar{\mathbf{H}} \\ \mathbf{0} & \mathbf{B}_0^T \bar{\mathbf{B}}_0 & \mathbf{B}_0^T \bar{\mathbf{H}} \\ \mathbf{0} & \mathbf{H}^T \bar{\mathbf{B}}_0 & \mathbf{H}^T \bar{\mathbf{H}} \end{bmatrix} \begin{Bmatrix} \dot{\mathbf{s}} \\ \dot{\boldsymbol{\beta}} \\ \dot{\boldsymbol{\rho}} \end{Bmatrix} \\
 + m\Omega^2 \begin{bmatrix} \mathbf{0} & \bar{\bar{\mathbf{B}}}_0 & \bar{\bar{\mathbf{H}}} \\ \mathbf{0} & \mathbf{B}_0^T \bar{\bar{\mathbf{B}}}_0 & \mathbf{B}_0^T \bar{\bar{\mathbf{H}}} \\ \mathbf{0} & \mathbf{H}^T \bar{\bar{\mathbf{B}}}_0 & \mathbf{H}^T \bar{\bar{\mathbf{H}}} \end{bmatrix} \begin{Bmatrix} \mathbf{s} \\ \boldsymbol{\beta} \\ \boldsymbol{\rho} \end{Bmatrix} = \begin{Bmatrix} -m\bar{\bar{\mathbf{H}}}\mathbf{r} \\ -m\mathbf{B}_0^T \bar{\bar{\mathbf{H}}}\mathbf{r} \\ \mathbf{f}_\rho \end{Bmatrix}. \quad (3.31)
 \end{aligned}$$

Therefore, it means that now the full dynamic of the rotating structures is being taken into account. There is a coupling between the degrees of freedom in translation of the rotating components and the degrees of freedom in translation of the hub but also a coupling between the degrees of freedom in translation of the rotating components and the degrees of freedom in rotation of the hub. Regarding the boundary condition imposed, in the fixed frame of reference, the shaft is clamped at both ends whereas in the rotating frame of reference, the blades are clamped to the hub. The different dimensions and material being used for this validation are available in Table 3.3.

<i>Parameter</i>	<i>Value</i>	<i>Units</i>
Blade length	2	m
Blade Young modulus	75.76	GPa
Blade Poisson coefficient	0.42	-
Blade's cross section	2500	mm <sup>2</sup>
Rotation shaft length	1	m
Rotation shaft Young modulus	200	GPa
Rotation shaft Poisson coefficient	0.3	-
Rotation shaft cross section	31414	mm <sup>2</sup>

TABLE 3.3 – Rotating shaft model parameters.

The material constituting the blades is gold as it is wanted to have blades as heavy as possible and with a Young modulus different from the one of the shaft to prevent mode coalescence between the blades and the shaft. The results obtained via the developed finite element code are partially compared to results obtained using ANSYS. Even though Ansys performed its analysis in the fixed frame of reference and without taking any time coupling on the rotating structure, the obtained results are good indicator on whether or not the developed code is well implemented. To compare the results, Campbell diagram are used. In order, to gain in computation time, only 1 element per rotating blades is taken into account. Although this is a fairly onerous assumption, it should not overly endorse the stability result obtained. In addition, the results of the Campbell diagrams start at 50 rad/s for obvious reasons of saving computing time. It goes without saying that having the evolution of the different modes of the structure from 0 rad/s would help this case to be fully validated. The obtained results using the developed finite element model are highlight in Figure 3.28 and Figure 3.29.

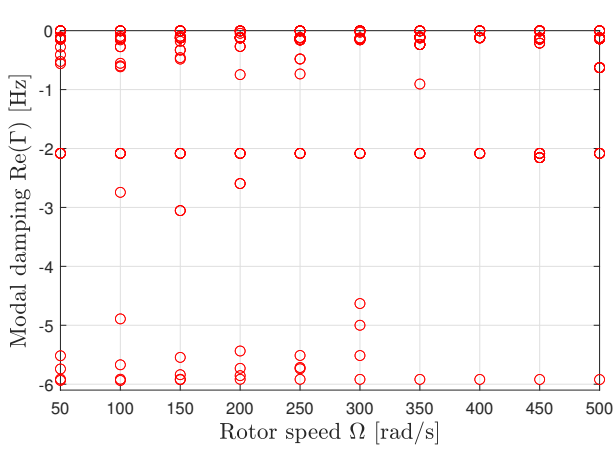
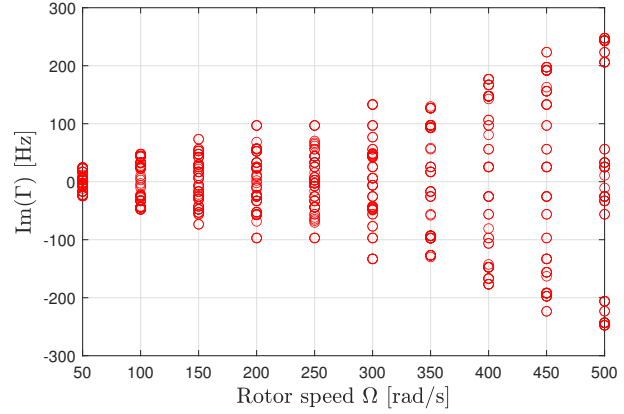


FIGURE 3.28 – Evolution of the modal damping with respect to the rotation speed of the shaft.


 FIGURE 3.29 – Evolution of the imaginary part of  $\Gamma$  as a function of the rotor speed of the shaft.

The results obtained start at a rotation speed of 50 rad/s in order to save calculation time. As the number of degrees of freedom in the analysis of this model is greater than for the GR model, the calculation times are longer and as the necessary computing power is not available, the study is carried out over an interval of 50 rad/s to 500 rad/s by segmenting the interval into 10 values. The analysis of Figure 3.28 shows the stable behavior of the structure studied with the finite element model developed. In addition, the obtained value for one mode strongly negative, meaning that this mode of vibration is over-damped. In addition, the relative modal damping ratio remains constant and oscillates slightly around its mean position as the speed of rotation increases, suggesting that this structure is highly stable as the speed of rotation increases. Looking at Figure 3.29, one can see that the imaginary part of  $\Gamma$  continues to grow as a function of the speed of rotation. This means that the natural frequencies of the modes diverge more and more as the speed of rotation increases. The increase in frequencies with rotation speed is linked to gyroscopic effects, which tend to increase the natural frequencies of certain modes but also to the complete coupling between the degrees of freedom of the rotating elements and the degrees of freedom of the hub which perfectly models the dynamics of the studied structure.

The original aim of this validation was to validate the implementation of the complete coupling between stationary and rotating elements by comparing the solution obtained by the implemented model and results of ANSYS. However, ANSYS does not offer suitable results as the stability analysis is performed in a static frame of reference therefore totally neglecting the time varying coupled term that are used for the complete coupling with the implemented finite element code. Therefore, the results obtained via ANSYS are not exploitable to validate the complete coupling model. Although the results provided by Ansys cannot be exploited directly, the stability indication can serve as an indicative basis. In fact, ANSYS predicts the stability of the system studied over the speed range studied, thereby supporting the conclusion drawn previously. The results obtained using ANSYS are available in Table 3.4. The results highlight the fact that there is no mode coalescence between the modes of the shaft and the one from the blades. To fully validate this model, a link between the modes obtained using ANSYS and the one obtained using the Floquet theory must be established but this is outside the scope of this master thesis and therefore must be investigated in a future work.

Stability	Mode	Type	100 Hz	200 Hz	300 Hz	400 Hz	500 Hz	600 Hz
Stable	1	Torsion	48.352 Hz	48.352 Hz	48.352 Hz	48.352 Hz	48.352 Hz	48.352 Hz
Stable	2	BW	132.62 Hz	132.61 Hz	132.6 Hz	132.59 Hz	132.58 Hz	132.42 Hz
Stable	3	FW	132.62 Hz	132.62 Hz	132.63 Hz	132.64 Hz	132.65 Hz	132.81 Hz
Stable	4	BW	298.59 Hz	298.57 Hz	298.49 Hz	298.43 Hz	298.38 Hz	297.27 Hz
Stable	5	FW	298.59 Hz	298.62 Hz	298.7 Hz	298.75 Hz	298.8 Hz	299.9 Hz
Stable	6	Bending	387.83 Hz	387.83 Hz	387.83 Hz	387.83 Hz	387.83 Hz	387.83 Hz

TABLE 3.4 – ANSYS results for different rotation speeds. BW = backward whirl, FW = forward whirl.

### 3.4.3 Unbalanced force validation

The unbalanced force can be validated using an analytical solution as a reference solution. To do so, consider a system similar to the ground resonance model presented in Figure 3.4 except that the model is now no longer composed of four blades but of one single blade. The unbalanced force takes its origin with the combination of two phenomena. The first one is when the axis of inertia of the studied system is parallel to the axis of rotation. The second one is when the axis of inertia of the studied system and the axis of rotation are secant to each other. The analytical solution corresponding to an unbalance force reads

$$F_x = mR\omega^2 \cos(\omega t), \quad (3.32)$$

$$F_y = mR\omega^2 \sin(\omega t). \quad (3.33)$$

The finite element equation characterising the unbalance force reads:

$$\mathbf{F}_u = -\mathbf{N}^T \bar{\bar{\mathbf{H}}} \mathbf{r}. \quad (3.34)$$

Figure 3.30 and Figure 3.31 both highlights the perfect correlation between the finite element solution implemented and the analytical solution. This correlation can be seen for both the  $F_x$  and  $F_y$  forces. Therefore, it is safe to conclude that the finite element implementation of the unbalanced force via the developed finite element code is correct and can be used safely.

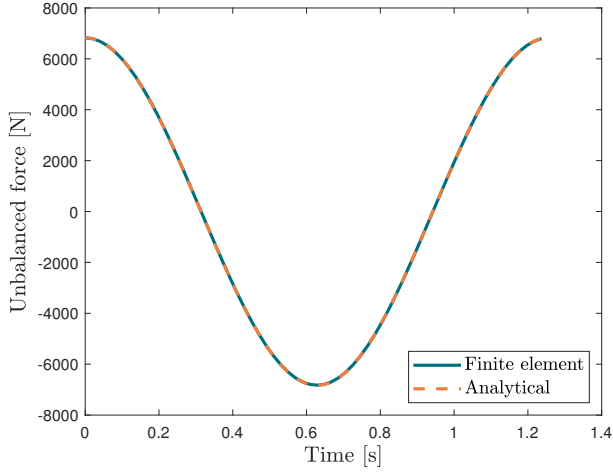


FIGURE 3.30 – Unbalanced force along  $X$  direction. Comparison between analytical solution and finite element solution.

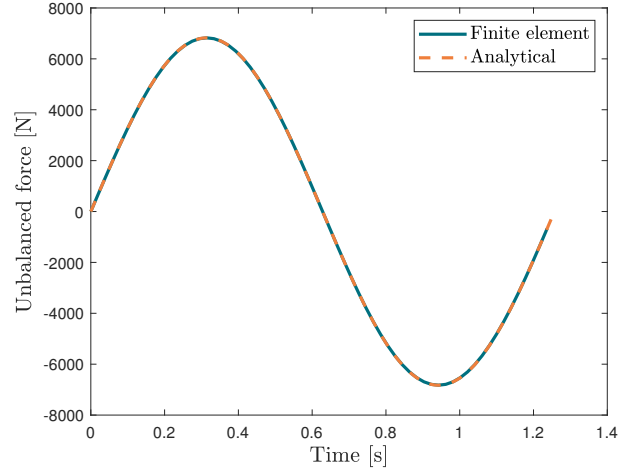


FIGURE 3.31 – Unbalanced force along  $Y$  direction. Comparison between analytical solution and finite element solution.

### 3.5 Conclusion

This chapter demonstrated an innovative way to couple rotating structures to a static one by using finite element formulation and expressing rotational structures in a floating frame of reference. The different integration scheme that could be used are validated on the basis of results available in the literature for a ground resonance model. The partial coupling between the rotating structures and the stationary one is validated also using a ground resonance model. In this validation was demonstrated the inability of the Newmark scheme to converge to stability for the finite element formulation whereas Runge-Kutta time integration scheme was able to converge to a stable solution but at the cost of a very long computation time. Finally, an attempt to validate the full time coupling between stationary and rotating structures is performed on a structure consisting of a shaft and four blades. It is unable to fully validate the full time coupling as the commercial software performs its stability analysis in the static frame of reference. However, the two formulations of the problem both predict the stability of the system at the rotation speeds tested, which suggests that the coupling has been correctly implemented. Finally, the finite element implementation of the unbalance force is validated on the basis of an analytical solution of the unbalance force for a single clamped rotating beam.

# CHAPTER 4

---

## TEST CASE OF A WING PROPELLER SYSTEM

The objective of this section is to apply the finite element model previously developed and apply it to an aerospace structure. In order to carry out a complete study of this system and to validate the various elements making up this structure, a modal analysis of a wing is achieved. Finally, the validated partial coupling is applied to a wing and propeller structure and the results are analysed. The aim of this chapter is to apply the previously established and validated finite element model coupling.

### 4.1 Standalone wing

The first structure being studied in this chapter is a wing clamped at the root. In order to validate this model, a Goland wing (Goland and Buffalo [65]), a type of wing extensively studied since its creation in the 1940s, is referred to in this context. The Goland wing's properties are referred to in Table 4.1. Examining this type of wing allows for the validation

<i>Parameter</i>	<i>Value</i>	<i>Units</i>
Half span $b/2$	6.096	m
Chord $c$	1.8288	m
Mass per unit of length $m$	35.71	kg/m
Span-wise elastic axis	33%/chord	-
Center of gravity	43%/chord	-
Spanwise bending rigidity	$9.77 \cdot 10^7$	Nm <sup>2</sup>
Torsional rigidity	$0.987 \cdot 10^7$	Nm <sup>2</sup>

TABLE 4.1 – Mechanical Properties of the Goland wing.

of both the finite element model that describes the structure's dynamics. Span-wise elastic axis and center of gravity positions value being expressed from the leading edge of the wing.

The equation describing the motion of the wing in a static frame of reference reads

$$\mathbf{M}\ddot{\mathbf{q}}_{\mathbf{w}} + \mathbf{C}\dot{\mathbf{q}}_{\mathbf{w}} + \mathbf{K}\mathbf{q}_{\mathbf{w}} = \mathbf{f}_{\mathbf{w}}. \quad (4.1)$$



#### 4.1.0.1 Eigenfrequencies computation of the undamped wing

The eigenfrequencies of the undamped wing and their related mode shape are of interest in the case of the whirl flutter phenomenon. Therefore, it is of interest to compute them. The wing equation of motion undergoing free vibration about a stable equilibrium position is given by

$$\mathbf{M}\ddot{\mathbf{q}}_{\mathbf{w}} + \mathbf{K}\mathbf{q}_{\mathbf{w}} = \mathbf{0}. \quad (4.2)$$

One can then solve the eigen value problem

$$\mathbf{K}\mathbf{x} = \omega^2\mathbf{M}\mathbf{x}. \quad (4.3)$$

A convergence study is performed over the number of elements constituting the structure;

A total number of 20 elements constituting the beam is chosen. The results obtained with the Matlab model are highlighted in Table 4.2

Frequency	$f_1$	$f_2$	$f_3$	$f_4$	$f_5$	$f_6$
Matlab model frequency [Hz]	7.8765	14.9369	44.8519	49.3612	74.8895	105.1326
Reference FEM model [66] [Hz]	7.664	15.245	39.053	55.583	72.276	/
Relative error [%]	2.77	-2.02	14.93	-11.19	3.61	/

TABLE 4.2 – First six natural frequencies obtained on MATLAB with 20 elements discretising the beam. Comparison with the FEM model developed by Akpinar [66]. Relative error computed assuming FEM model of Akpinar being the reference.

By analysing the obtained results and their relative error compared to a reference in Table 4.2, it is visible that there is a good correlation between the established MATLAB model and the reference FEM model on which the relative error is computed. A relative error of less than 3%, in absolute terms, is obtained on the first two frequencies, which can be considered sufficient to validate the accuracy of the model created. Moreover, the lowest relative error is reached on these frequencies. This is important given that the first bending and torsion modes of the wing impact the dynamic behavior of the wing-propeller system, which will be studied later. Looking at third and fourth eigenfrequencies, a larger relative error is achieved. This is mainly due to the type of finite element chosen. In fact, the MATLAB model developed is based on 3D Euler-Bernoulli elements whereas the reference obtains its results using a 2D finite element formulation. In addition, the first corresponding bending mode obtained with the developed model is in agreement with the reference. The first torsional mode cannot be concluded as the wing is modeled as a simple beam with wing inertia properties.

### 4.1.1 Wing aerodynamics

In this section, the main theories used to calculate the aerodynamic forces on a wing and on a propeller are presented, but will not be applied in the rest of this project.

#### 4.1.1.1 Theodorsen's theory

The theory developed by Theodorsen [67] is a 2D theory which models the unsteady lift on bi-dimensional flat plate with a simple harmonic motion. The main assumption of

Theodorsen's theory is that attached flow conditions are always assumed, the wake is modeled via a planar wake meaning that the movement of the wake is directly linked to the movement of the freestream. The effect of the wake history changes the circulation of the fluid around the flat plate. The bi-dimensional lift force and pitching moment for a flat plate in a freestream of density  $\rho$  and speed  $V$  reads

$$L = \pi\rho b^2(\ddot{h} + V\dot{\alpha} - ba\ddot{\alpha}) + 2\pi\rho VbC(k)w, \quad (4.4)$$

$$M = \pi\rho b^2 \left[ ab\ddot{h} - Vb\left(\frac{1}{2} - a\right)\dot{\alpha} - b^2\left(\frac{1}{8} + a^2\right)\ddot{\alpha} \right] + 2\pi\rho Vb^2\left(a + \frac{1}{2}\right)C(k)w, \quad (4.5)$$

where  $b$  is the airfoil semi-chord,  $h$  is the vertical displacement of the airfoil,  $\alpha$  is the rotation of the airfoil about the elastic axis,  $a$  is the relative location of the elastic axis compared to the semichord, and  $w$  is the total aerodynamic downwash at the three quarter chord position in the airfoil. The total aerodynamic downwash reads

$$w = \dot{h} + V\alpha + b\left(\frac{1}{2} - a\right)\dot{\alpha}. \quad (4.6)$$

Finally, the term  $C(k)$  is called the Theodorsen function. When studying flutter, Theodorsen function generally takes the form

$$C(k) = 1 - \frac{0.165}{1 - \frac{0.0455}{k}j} - \frac{0.335}{1 - \frac{0.3}{k}j}, \quad (4.7)$$

where  $k$  corresponds to the reduced frequency and is computed as

$$k = \frac{\omega b}{V}, \quad (4.8)$$

where  $\omega$  corresponds to the frequency of motion of the flat plate. The first term of each equation of Eq.4.5 corresponds to the non circulatory lift and the non circulatory moments whereas the second term of equation of Eq.4.5 corresponds to the circulatory lift and the circulatory moment. The non circulatory lift and moments corresponds are results of added mass effect whereas the circulatory lift and moments both includes the wake history effect of the lift and on the moment acting on the airfoil. It is of interest to notice that the set of equations in Eq.4.5 is a combination of time dependent term and frequency dependent term. When studying flutter, this is not a problem and it can be handled. However, when the evolution of lift and moment over time is needed, this is a problem. To remove this frequency dependency, a method proposed by Wagner or by Leishman can be used but this is not developed in the scope of this work.

#### 4.1.1.2 Strip theory

Applying Theodorsen's theory to a finite wing is an enormous simplification. In fact, the theory suggests that each strips constituting the wing is infinite. This simplification is only valid for large aspect ratio wing. In reality, three dimensional effect takes place thus decreasing the total lift produced by the wing altering the lift distribution over the wing. Yates Jr. [68] suggest to modify the previously establish lift and moment expression by Theodorsen's theory. Its theory modify the constant lift coefficient by a variable lift

coefficient over the wing  $C_{l_\alpha}$  and a variable aerodynamic center position  $a_c$ . Therefore, the lift, the moment and the downwash over a strip reads

$$L = \pi \rho b^2 (\ddot{h} + V \dot{\alpha} - ba \ddot{\alpha}) + C_{l_\alpha} \rho V b C(k) w, \quad (4.9)$$

$$M = \pi \rho b^2 \left[ ab \ddot{h} - V b \left( \frac{C_{l_\alpha}}{2\pi} + a_c - a \right) \dot{\alpha} - b^2 \left( \frac{1}{8} + a^2 \right) \ddot{\alpha} \right] + C_{l_\alpha} \rho V b^2 (a - a_c) C(k) w, \quad (4.10)$$

$$w = \dot{h} + V \alpha + b \left( \frac{C_{l_\alpha}}{2\pi} + a_c - a \right) \dot{\alpha}. \quad (4.11)$$

If the strip lift coefficient is not known, the elliptical lift curve slope can be used. The elliptical lift curve slope is computed as

$$C_{l_\alpha} = 2\pi \sqrt{1 - \frac{y^2}{b^2}}, \quad (4.12)$$

where  $y$  is the distance of the strip from the wing root and  $b$  is the semi-span of the wing.

### 4.1.2 Flutter speed computation

The flutter speed is computed using a  $p - k$  method (Hassig [69]). The derivation of the flutter is presented by Güner [70] and the main derivation is presented here. The dynamics equation in its most general form reads:

$$\mathbf{M} \ddot{\mathbf{x}}(t) + \mathbf{C} \dot{\mathbf{x}}(t) + \mathbf{K} \mathbf{x} = \mathbf{f}. \quad (4.13)$$

Using the transformation between the coordinate and the modal coordinates

$$\mathbf{x}(t) = \Phi \mathbf{q}(t), \quad (4.14)$$

Eq. 4.13 can be written in modal coordinates

$$\mathbf{M}_q \ddot{\mathbf{q}}(t) + \mathbf{C}_q \dot{\mathbf{q}}(t) + \mathbf{K}_q \mathbf{q}(t) = \mathbf{f}_q(t), \quad (4.15)$$

where  $\mathbf{M}_q$ ,  $\mathbf{C}_q$  and  $\mathbf{K}_q$  are respectively the modal mass matrix, the modal damping matrix and the modal stiffness matrix. Making the assumption of a damped sinusoidal motion, it is possible to define the damping which control the flutter to occur.

$$\mathbf{q}(t) = \hat{\mathbf{q}}(t) e^{p \frac{U_\infty}{l} t} = \hat{\mathbf{q}} e^{p\tau}, \quad (4.16)$$

where  $\tau$  is the non-dimensional time,  $\omega$  is the oscillatory frequency, and  $\hat{\mathbf{q}}$  is the amplitude. The non-dimensional parameter  $p$  is defined as:

$$p = g + ik, \quad (4.17)$$

where  $k$  is the reduced frequency and  $g = \gamma k$ , where  $\gamma$  is the true damping coefficient and is defined as

$$\gamma = \frac{1}{2\pi} \ln \left( \frac{a_{i+1}}{a_i} \right), \quad (4.18)$$

where  $a_{i+1}$  and  $a_i$  corresponds to the amplitude of successive cycles. As a result, using Eq.4.16, the flutter equation reads:

$$\left[ \frac{U_\infty}{l^2} \mathbf{M}_q p^2 + \frac{U_\infty}{m} \mathbf{C}_q p + \mathbf{K}_q - \frac{1}{2} \rho_\infty U_\infty^2 \mathbf{Q}(p) \right] \hat{\mathbf{q}} = 0, \quad (4.19)$$

where  $U_\infty$  is the freestream velocity and  $\mathbf{Q}(p)$  is the complex modal aerodynamic force matrix for a harmonic motion of reduced frequency  $\Im(p) = k$  and damping characterised by  $\Re(p) = g$ . The  $p - k$  method assumes that the modal aerodynamic force is only valide for an undamped simple harmonic motion ( $g = 0$ ). Therefore, the flutter equation reads:

$$\left[ \frac{U_\infty}{l^2} \mathbf{M}_q p^2 + \frac{U_\infty}{m} \mathbf{C}_q p + \mathbf{K}_q - \frac{1}{2} \rho_\infty U_\infty^2 \mathbf{Q}(ik) \right] \hat{\mathbf{q}} = 0. \quad (4.20)$$

To determine the flutter speed of a structure, this equation must be solved for every free-stream  $U_{inf}$  and every single mode constituting the structure must be tested separately.

## 4.2 Propeller Aerodynamics

To better predict whirl flutter frequency and get as close as possible to reality, it is necessary to compute the aerodynamic load acting on the propeller. The aim of this thesis is to mainly apply the finite element model and more specifically the coupling between the stationary part (the hub) and the rotating part (the propeller blades). Therefore, the aerodynamic model is just presented for anyone wishing to follow up on this thesis and wanting to improve the whirl flutter prediction. The aerodynamic model is based on the model published by Rodden and Rose [71]. In this theory, the propeller blades are assumed to be rigid. This is a strong assumption which could affect the results obtained later. In addition, the effect of the wing downwash on the propeller aerodynamic forces is also considered which, on the other hand, helps to get as close as possible to the physical phenomena present. The formulation is based on a quasi-steady approach. The main equations of the different forces and moments are presented here while details of all the terms in the equation are given in reference [71] for clarity.

First, the effective angles are defined as

$$\bar{\theta}_P = \theta_P - \frac{e}{V} \dot{\theta}_P; \quad (4.21)$$

$$\bar{\psi}_P = \psi_P - \frac{e}{V} \dot{\psi}_P. \quad (4.22)$$

The forces and moments acting on the propeller hub are defined as:

$$F_{z,P} = \frac{1}{2} \rho V^2 \pi R^2 \left( c_{z,\theta} \bar{\theta}_P + c_{z,\psi} \bar{\psi}_P + c_{z,q} \frac{R}{V} \dot{\theta}_P + c_{z,r} \frac{R}{V} \dot{\psi}_P \right); \quad (4.23)$$

$$F_{y,P} = \frac{1}{2} \rho V^2 \pi R^2 \left( c_{y,\theta} \bar{\theta}_P + c_{y,\psi} \bar{\psi}_P + c_{y,q} \frac{R}{V} \dot{\theta}_P + c_{y,r} \frac{R}{V} \dot{\psi}_P \right); \quad (4.24)$$

$$M_{y,P} = \rho V^2 \pi R^3 \left( c_{m,\theta} \bar{\theta}_P + c_{m,\psi} \bar{\psi}_P + c_{m,q} \frac{R}{V} \dot{\bar{\theta}}_P + c_{m,r} \frac{R}{V} \dot{\bar{\psi}}_P \right); \quad (4.25)$$

$$M_{z,P} = \rho V^2 \pi R^3 \left( c_{n,\theta} \bar{\theta}_P + c_{n,\psi} \bar{\psi}_P + c_{n,q} \frac{R}{V} \dot{\bar{\theta}}_P + c_{n,r} \frac{R}{V} \dot{\bar{\psi}}_P \right). \quad (4.26)$$

### 4.3 Application to an aerospace structure

The aim is now to apply the previously established coupling model to an aerospace structure. The structure being studied is a wing and a flexibly attached propeller. The propeller is flexibly attached at middle of the wing half span. In this study, the aerodynamic forces acting on both the wing and the propeller are neglected. In addition, as Euler-Bernoulli beam elements are being used to represent the wing, the bending center and the center of gravity are at the same position. Finally, a partial coupling is applied between the hub and the rotating blades and vice versa. A schematic of the studied structure is represented in Figure 4.1. A stiffness and a damper in pitch and yaw direction are added at the pivoting point, to help controlling the whirl flutter phenomenon.

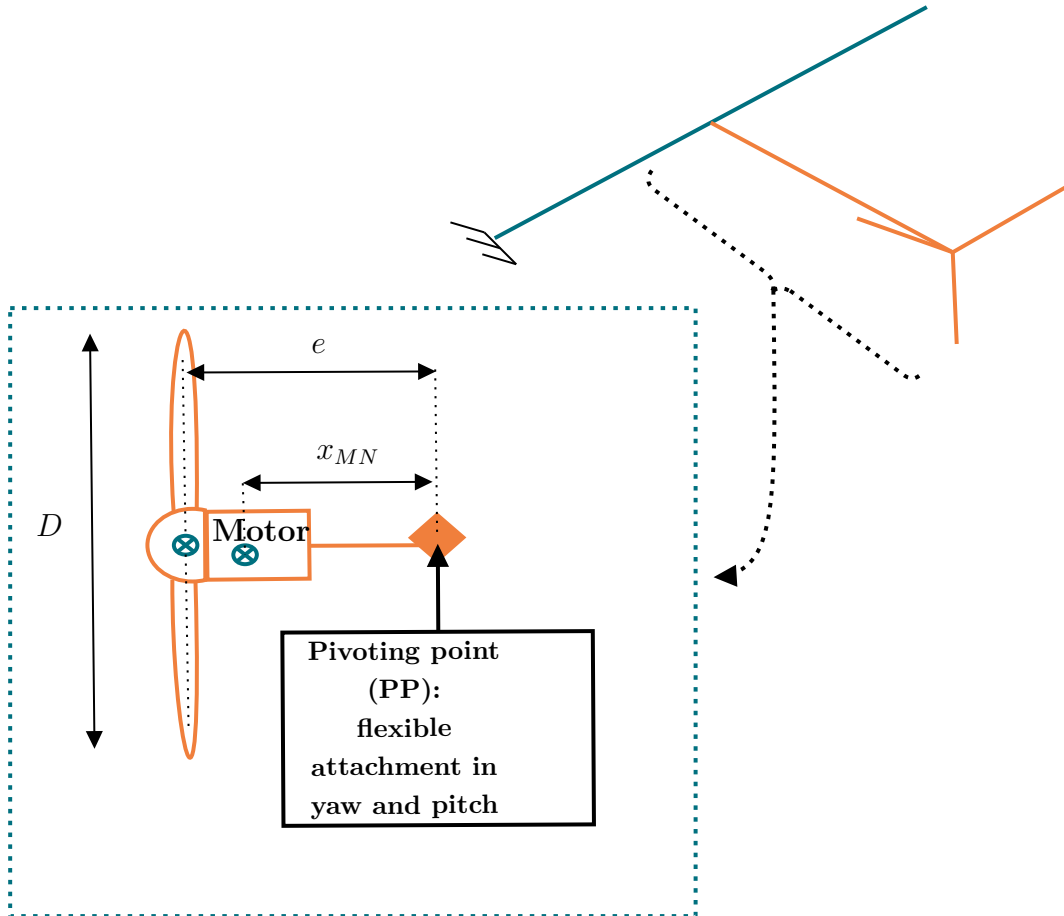


FIGURE 4.1 – Wing Propeller structure. Propeller being flexibly attached to the wing via springs and dampers in pitch and yaw direction. Partially reproduced from [27].

### 4.3. APPLICATION TO AN AEROSPACE STRUCTURE

The different properties of the wing and of the propeller are highlighted in Table 4.3, Table 4.4 and Table 4.5. The different values are taken from [72].

<i>Parameter</i>	<i>Value</i>	<i>Units</i>
Wing span	11.4	m
Root chord	1.25	m
Tip chord	0.8	m
Mass per unit length	25	kg/m
Radius of gyration (about CG)	25% chord	-
Spanwise elastic axis (from LE)	50% chord	-
Centre of gravity (from LE)	50% chord	-
Bending rigidity (EI)	$7 \times 10^5$	Nm <sup>2</sup>
Torsional rigidity (GJ)	$2 \times 10^5$	Nm <sup>2</sup>

TABLE 4.3 – Mechanical properties of the wing.

<i>Parameter</i>	<i>Value</i>	<i>Units</i>
Rotor mass	8	kg
Motor-nacelle mass	35	kg
Position of rotor CG $e$	1.16	m
Position of motor CG $x_{MN}$	0.86	m
Pitch damping, $g_\theta$	0.005	%
Yaw damping, $g_\psi$	0.005	%
Pitch stiffness $k_\theta$	70	kN/m
Yaw stiffness $k_\psi$	70	kN/m

TABLE 4.4 – Mechanical properties related to Pitch and Yaw Axes of the propeller. The position of the rotor CG and motor CG are expressed from the wing CG.

<i>Parameter</i>	<i>Value</i>	<i>Units</i>
$I_Q$	1.55	kg · m <sup>2</sup>
$I_{\theta,P}$	36.65	kg · m <sup>2</sup>
$I_{\psi,P}$	36.65	kg · m <sup>2</sup>
$S_{\theta,P}$	-39.38	kg · m
$I_{\theta\alpha,P}$	36.65	kg · m <sup>2</sup>
$I_{\alpha,P}$	36.65	kg · m <sup>2</sup>
$S_{\alpha,P}$	-39.38	kg · m

TABLE 4.5 – Inertial and structural properties of the propeller.

The obtained results are available in Figure 4.2 and Figure 4.3. The results are obtained over a speed range from 400 rad/s to 600 rad/s, by segmenting this speed range into 6 distinct calculation points. This decision is taken with the sole aim of reducing the calculation time, which is already very substantial. The only purpose of the study carried out on this aerospace application is to demonstrate the capacity of the code developed to work on complex structures. Analysing Figure 4.2, one can establish the studied wing propeller structure is stable at the different rotation speed tested. It is clear that no conclusion on the stability can be drawn between the different rotation speeds tested. In addition, there are a lot of real part of the characteristic exponents  $\Gamma$  located around 0, meaning that the system might become unstable for greater rotation speed. The system might be unstable on the speed range tested. However, one is unable to capture it because of the discretization of the interval adopted. Some modes might be over damped but this is probably due to the choice of the parameters adopted at the connecting point between the propeller and the wing structure and triggering the whirl-flutter phenomenon. To find out for sure, a study of the influence of these parameters on whirl-flutter should be carried

out. Looking at the evolution of the imaginary part of the characteristic exponent  $\Gamma$  in Figure 4.3, one can see the influence of the gyroscopic term on the imaginary part of  $\Gamma$  so as demonstrated in 4.3.

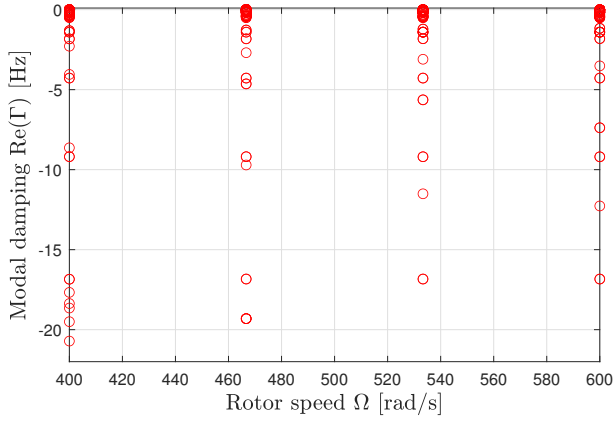


FIGURE 4.2 – Evolution of the relative modal damping ratio with respect to the rotation speed of the propeller.

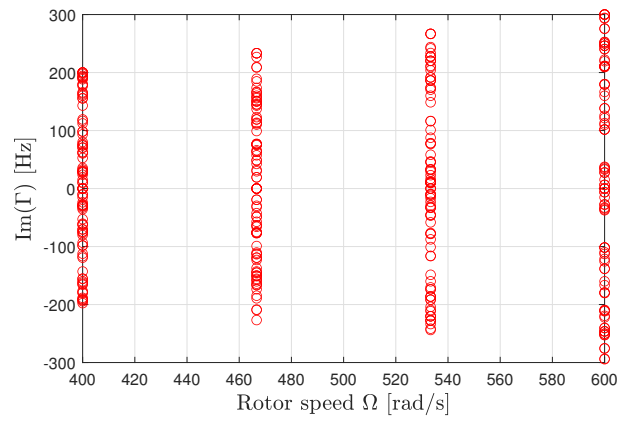


FIGURE 4.3 – Evolution of the imaginary part of  $\Gamma$  as a function of the rotor speed of the propeller.

## 4.4 Conclusion

In this chapter is studied the case of a wing propeller aerospace structure. First, the case of a Goland wing is studied to validate the finite element mass and elastic stiffness matrices used in this study. The different aerodynamic force acting on the structure ,although not use in this study, are presented. The ability of the developed finite element code to work on such type of complex structure is highlighted.

### Conclusions.

The aim of this work was to develop a finite element code that is able to predict whirl flutter using the Floquet theory to establish the stability of aerospace structure. The developed finite element code highlights the capability to study rotor dynamics when enabling a partial coupling between the different rotating structures and the hub to which they are linked. From the author's knowledge, it is the first time that a full coupling between stationary and rotating structure is established under a finite element formulation.

Chapter 1 presents the different possibilities to study the stability of structures from the hypothesis of a LTI system and to study the stability of a LTP system using the Floquet theory, but also presenting the Coleman transformation. Each of the different methods presented have their advantages, disadvantages and their different degree of precision on the stability analysis. The different numerical schemes that can be used to study the stability of an LTP system are presented, and the methodology to compute the monodromy matrix or its expression as a function of the numerical integration scheme used is presented.

Chapter 2 consists in studying a rotating structure and presenting the different equations related to it in a rotating frame of reference. The studied structure and its implementation are validated comparing obtained results using a commercial software and literature. It came to the conclusion that the implementation of the different matrices is well executed. The validation is performed by analysing the Campbell diagram of the clamped rotating beam. The results obtained show a perfect correlation between the implemented finite element code and the commercial software. This result also highlights the impact of the centrifugal stiffness matrix on the natural frequencies of the system.

Chapter 3 is the most important contribution of this thesis. Indeed, the theory allowing a coupling between a static and a rotating part is explained at the particle level. A finite element formulation is then proposed by identifying the different matrices on which temporal coupling occurs. In addition, an implementation strategy for this coupling is developed for the finite element formulation. The partial coupling is then validated using a ground resonance validation model. First, the rigid model of the validation case is studied and used to validate the numerical integration model. The various integration schemes are validated using the literature. Then, the finite element formulation, which features a partial coupling between the hub degrees of freedom in translation and those of the rotating elements, is



## CONCLUSIONS AND PERSPECTIVES

studied. The study of the system with the finite element formulation allows the validation of the finite element implementation of the coupling while highlighting the inability of the Newmark integration scheme to converge to a solution for the prediction of the stability. Finally, the full coupling is studied but not validated. However, the results obtained are optimistic about the possibility of validating it.

Chapter 4 applies the finite element model developed earlier to an aerospace structure. First, the natural frequencies of a Goland wing are studied in order to validate the implementation of the finite element model on a wing. Next, the calculation of aerodynamic forces on a wing is presented. In addition, the aerodynamic forces acting on a propeller are presented. Finally, the finite element model is applied to the aeronautical structure, using a partial coupling. The results obtained are studied using a Campbell diagram.

### Perspectives.

The work carried out highlights the potential benefits of using Floquet's theory to study the dynamics of rotating systems. This theory is applied using a full time coupling on the mass, gyroscopic and centrifugal stiffness matrices of the rotating parts expressed in the rotating frame of reference. However, certain assumptions have been made. As a result, the work and the code used to produce the results can be improved, either to increase the accuracy of the results or to reduce the computation time required to obtain the results.

The following is a list of potential improvements to be made for improvement on the precision of the results, computational time and the full validation of the code

- The present model use Euler-Bernoulli 3D beam elements to model the structural properties of the different structures incorporating the global structure. As stated in Chapter 2, Euler-Bernoulli 3D beam elements has assumptions limiting its range of validity. Therefore, it is of interest to implement and to use Timoshenko beam elements [73]. Timoshenko beam elements incorporate shear deformation effects, making this type of element more suitable to study short beams, thick beams or beams made of a material with low shear stiffness. The inclusion of shear deformation makes Teemochenko beam elements more suitable to accurately predict the dynamic response of such a structure.
- The present work highlights Chapter 3 the inability of the Newmark integration scheme to give consistent results when employing the finite element formulation of the problem although the numerical scheme is able to produce consistent results when using the rigid formulation of the problem. Some possible avenues for this failure have been put forward but need to be investigated in more detail. Depending on whether or not the results of this investigation are conclusive, one will have to be taken on the choice of time integration scheme to study stability of the studied structure over a period of revolution. A compromise will have to be made between the accuracy of the desired results and the computing time required to obtain them.
- Chapter 3 revealed that computing time was a real issue in obtaining results. This could be reduced by using another programming language, such as Python, which has a number of open-source libraries for efficient parallelization of computations.
- Identify the link between the mode shapes obtained in ANSYS and the one obtained

using the Floquet theory in order to try to validate the complete time dependent coupling.

- Another potential method for reducing calculation times is to use a reduction technique, such as the one proposed by Craig-Bampton [74], then to apply the coupling on the terms retained in this reduction. This will significantly reduce calculation times, thus making the developed code faster.
- A simplification of the current code architecture may also be considered. Although not addressed in this report, this may prove useful for anyone wishing to continue this work from the code already established. The identification of the nodes on which coupling takes place can be simplified by effectively tagging them.
- Currently, the dynamics of the various rotating elements are only linked via the hub node. This is a simplification of the solution. To compensate this, it would be wise to add a spring linking each of the rotating parts together. With this addition, the dynamics of each of the rotating components would be linked by more than just the hub node to which they are connected. In addition, the hub is actually modeled using a single node, whereas in reality it is a complex geometry. Therefore, representing the real geometry of the hub will help to obtain more accurate results for predicting the whirl-flutter phenomenon.
- The code developed has been partially validated using results from the literature. However, it would be of interest to find analytical validation cases to confirm the good behavior of the coupling terms on the dynamics of the system using results from a problem with a known analytical solution.
- The current code only deals with the first stress on the structure due to centrifugal force. If external forces have to be taken into account in the analysis, it is advisable to take these forces into account when calculating the stiffness matrix of the externally-loaded structure.
- An important aspect that has been neglected in this study is the consideration of aerodynamic forces. Taking these forces into account and studying their impact on the prediction of whirl flutter must be carried out in future work. Various methods for calculating aerodynamic forces have been presented but were not employed in the study. It would be interesting to study the difference in whirl-flutter prediction using different methods for aerodynamic force prediction. Since two parameters will now have an influence on the prediction of the phenomenon, namely air speed and rotor speed, the study of whirl flutter should be carried out as a function of the advance ratio.
- The most challenging perspectives and the last one is the validation of the full code on an aerospace structure against experimental data available. If not available, such experimental data may be obtained carrying out wind tunnel tests. This perspective is the most important one as it will allow to fully validate the developed code, even though parts of the code have already been validated against analytical solutions, and to know the limitations of this code when predicting whirl-flutter instability.



## APPENDIX A

## ELEMENTARY MASS MATRIX

The elementary mass matrix for 3D Euler-Bernoulli beam elements is developed by Gerardin and Rixen [47]. The elementary mass matrix is given by

$$\mathbf{M}_{elm} = m\ell \begin{bmatrix} \frac{1}{3} & & & & & & & & & & & \\ 0 & \frac{13}{35} & & & & & & & & & & \\ 0 & 0 & \frac{13}{35} & & & & & & & & & \\ 0 & 0 & 0 & \frac{r_1^2}{3} & & & & & & & & \\ 0 & 0 & -\frac{11\ell}{210} & 0 & \frac{\ell^2}{105} & & & & & & & \\ 0 & \frac{11\ell}{210} & 0 & 0 & 0 & \frac{\ell^2}{10} & & & & & & \\ \frac{1}{6} & 0 & 0 & 0 & 0 & 0 & \frac{1}{3} & & & & & \\ 0 & \frac{9}{70} & 0 & 0 & 0 & \frac{13\ell}{420} & 0 & \frac{13}{35} & & & & \\ 0 & 0 & \frac{9}{70} & 0 & -\frac{13\ell}{420} & 0 & 0 & 0 & \frac{13}{35} & & & \\ 0 & 0 & 0 & \frac{r_1^2}{6} & 0 & 0 & 0 & 0 & 0 & \frac{r_1^2}{3} & & \\ 0 & 0 & \frac{13\ell}{420} & 0 & -\frac{\ell^2}{140} & 0 & 0 & 0 & \frac{11\ell}{210} & 0 & \frac{\ell^2}{105} & \\ 0 & -\frac{13\ell}{420} & 0 & 0 & 0 & -\frac{\ell^2}{140} & 0 & -\frac{11\ell}{210} & 0 & 0 & 0 & \frac{\ell^2}{105} \end{bmatrix} \quad \text{Sym.}$$



## APPENDIX B

## SHAPE FUNCTION MATRIX

The transposed shape function matrix  $\mathbf{N}^T$  for Euler-Bernoulli beam elements is derived by Przemieniecki [75] and reads:

$$\begin{aligned}\xi &= \frac{x}{l}; \\ \eta &= \frac{y}{l}; \\ \zeta &= \frac{z}{l}.\end{aligned}$$

where  $l$  corresponds to the length of the element.

$$\mathbf{N}^T = \begin{bmatrix} 1 - \xi & 0 & 0 \\ 6(\xi - \xi^2)\eta & 1 - 3\xi^2 + 2\xi^3 & 0 \\ 6(\xi - \xi^2)\zeta & 0 & 1 - 3\xi^2 + 2\xi^3 \\ 0 & -(1 - \xi)l\zeta & -(1 - \xi)l\eta \\ (1 - 4\xi + 3\xi^2)l\zeta & 0 & (-\xi + 2\xi^2 - \xi^3)l \\ (-1 + 4\xi - 3\xi^2)l\eta & (\xi - 2\xi^2 + \xi^3)l & 0 \\ \xi & 0 & 0 \\ 6(-\xi + \xi^2)\eta & 3\xi^2 - 2\xi^3 & 0 \\ 6(-\xi + \xi^2)\zeta & 0 & 3\xi^2 - 2\xi^3 \\ 0 & -l\xi\zeta & -l\xi\eta \\ -2\xi + 3\xi^2)l\zeta & 0 & (\xi^2 - \xi^3)l \\ (2\xi - 3\xi^2)l\eta & (-\xi^2 + \xi^3)l & 0 \end{bmatrix}^T$$



## APPENDIX C

### ELEMENTARY STIFFNESS MATRIX

The elementary stiffness matrix for 3D Euler-Bernoulli beam elements is developed by Gerardin and Rixen [47]. The elementary stiffness matrix is given by

$$\mathbf{K}_{elm} = \begin{bmatrix} \frac{EA}{\ell} & 0 & 0 & 0 & 0 & 0 & 0 & 0 & 0 & 0 & 0 & 0 \\ 0 & \frac{12EI_z}{\ell^3} & 0 & 0 & 0 & 0 & 0 & 0 & 0 & 0 & 0 & 0 \\ 0 & 0 & \frac{12EI_y}{\ell^3} & 0 & 0 & 0 & 0 & 0 & 0 & 0 & 0 & 0 \\ 0 & 0 & 0 & \frac{GJ_x}{\ell} & 0 & 0 & 0 & 0 & 0 & 0 & 0 & 0 \\ 0 & 0 & \frac{-6EI_y}{\ell^2} & 0 & \frac{4EI_y}{\ell} & 0 & 0 & 0 & 0 & 0 & 0 & 0 \\ 0 & \frac{6EI_z}{\ell^2} & 0 & 0 & 0 & \frac{4EI_z}{\ell} & 0 & 0 & 0 & 0 & 0 & 0 \\ -\frac{EA}{\ell} & 0 & 0 & 0 & 0 & 0 & \frac{EA}{\ell} & 0 & 0 & 0 & 0 & 0 \\ 0 & \frac{-12EI_z}{\ell^3} & 0 & 0 & 0 & \frac{-6EI_z}{\ell} & 0 & \frac{12EI_z}{\ell^3} & 0 & 0 & 0 & 0 \\ 0 & 0 & \frac{-12EI_y}{\ell^3} & 0 & \frac{6EI_y}{\ell^2} & 0 & 0 & 0 & \frac{12EI_y}{\ell^3} & 0 & 0 & 0 \\ 0 & 0 & 0 & \frac{-GJ_x}{\ell} & 0 & 0 & 0 & 0 & 0 & \frac{GJ_x}{\ell} & 0 & 0 \\ 0 & 0 & \frac{-6EI_y}{\ell^2} & 0 & \frac{2EI_y}{\ell} & 0 & 0 & 0 & \frac{6EI_y}{\ell} & 0 & \frac{4EI_y}{\ell} & 0 \\ 0 & \frac{6EI_z}{\ell^2} & 0 & 0 & 0 & \frac{2EI_z}{\ell} & 0 & \frac{-6EI_z}{\ell^2} & 0 & 0 & 0 & \frac{4EI_z}{\ell} \end{bmatrix} \quad \text{Sym.}$$





## APPENDIX D

### NEWMARK INTEGRATION SCHEME

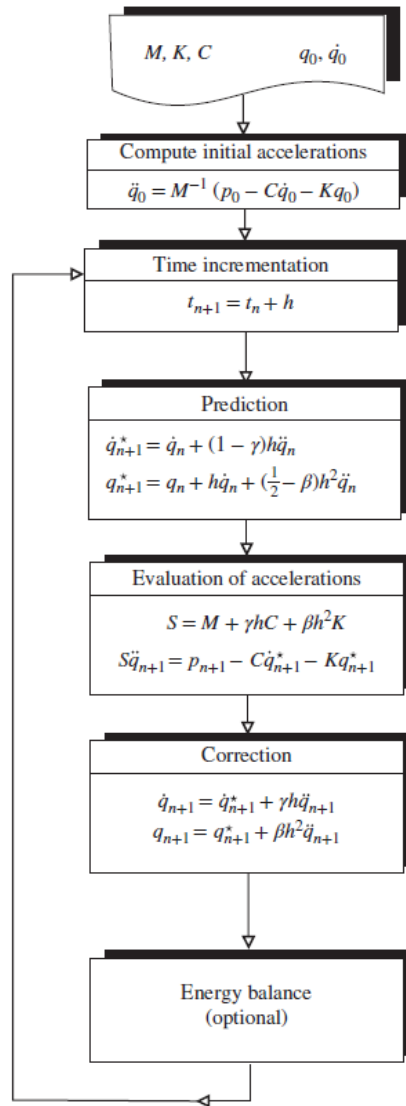


FIGURE D.1 – Flowchart of the Newmark integration scheme for linear systems. Taken from [47].



## APPENDIX E

### GAUSS LEGENDRE INTEGRATION

The different integrals used in this work are computed using Gauss Legendre integration also know as Gauss quadrature. The Gauss quadrature states that a single variable function can be computed as

$$\int_{-1}^1 f(\kappa) d\kappa \approx \sum_{i=1}^n w_i f(\kappa_i),$$

where  $\kappa_i$  with  $i = 1, \dots, n$  are the  $n$  abscissa location the  $n$  Gauss point. The abscissa and their respective weights are related to the Legendre polynomials. The abscissa  $\kappa_1, \dots, \kappa_n$  are the roots of the  $n$  Legendre polynomial and the weights are computed as:

$$\omega_i = \frac{-2}{(n+1)P'_n(\kappa_i)P_{n+1}(\kappa_i)} = \frac{2}{(1-\kappa_i^2)P'_n(\kappa_i)^2}.$$

Looking at the precision of the integration. If  $n$  refers to the numbers of Gauss point and  $p$  is the degree of the polynomial to be integrated, then the number of Gauss points  $n$  needed to perform exact integration is given by

$$p = 2n - 1.$$

As the highest degree of the polynomial encountered by the product  $\mathbf{N}^T \mathbf{N}$  is 6, it is necessary to have, at least, 4 Gauss points to perform an exact integration of the polynomial. This number of Gauss points is therefore chosen.

The location of the different Gauss points and their respective weights are available in Table E.1

APPENDIX E. GAUSS LEGENDRE INTEGRATION

$n$	Roots $\kappa_i^*$	Weight $w_i$
2	0.5773502692	1.0000000000
	-0.5773502692	1.0000000000
3	0.7745966692	0.5555555556
	0.0000000000	0.8888888889
	-0.7745966692	0.5555555556
4	0.8611363116	0.3478548451
	0.3399810436	0.6521451549
	-0.3399810436	0.6521451549
	-0.8611363116	0.3478548451
5	0.9061798459	0.2369268850
	0.5384693101	0.4786286705
	0.0000000000	0.5688888889
	-0.5384693101	0.4786286705
	-0.9061798459	0.2369268850

TABLE E.1 – Roots and weights of nth Legendre polynomials for  $n = 2, 3, 4$  and  $5$ .

# APPENDIX F

---

## STRUCTURAL COUPLING BETWEEN HUB AND ROTATING COMPONENTS

---

**Algorithm 2** Structural Coupling between Hub and Rotating Components

---

```

1: for each element requiring a time coupling do
2:   Compute the transformation matrix  $Re$ 
3:   Construct the transformation matrix  $Te = \text{diag}(Re, Re, Re, Re)$ 
4:   Calculate the Gauss point position in the rotating frame of reference
5:   Compute the matrices  $B0$ ,  $dB0$ ,  $ddB0$  in the rotating frame of reference for the
   desired time step
6:   Transform these matrices to the element frame using the transformation matrix  $Re$ 
7:   Compute the matrices  $H$ ,  $dH$ ,  $ddH$  for the desired time step
8:   Transform the matrices  $H$ ,  $dH$ ,  $ddH$  to the element frame  $Re$ 
9:   Compute the rotating structure/rotating structure coupling matrix  $M_{rot}$ 
10:  Transform  $Mel$  with  $Te$  and add to  $M_{rot}$ 
11:  Update  $M_{rot}$  matrix:
12:   $M_{rot\_current} \leftarrow M_{rot}(elm\_dof, elm\_dof)$ 
13:   $MeS\_slice \leftarrow MeS(:, :)$ 
14:   $M_{rot\_updated} \leftarrow M_{rot\_current} + MeS\_slice$ 
15:   $M_{rot}(elm\_dof, elm\_dof) \leftarrow M_{rot\_updated}$ 

16:  Compute the hub/rotating structure coupling matrix  $M_1$  for translational dof
17:  Transform  $Mel$  with  $Te$  and add to  $M_1$ 
18:  Update  $M_1$  matrix:
19:   $M1\_current \leftarrow M_1(\text{hub\_dof\_translation}, elm\_dof)$ 
20:   $MeS\_slice \leftarrow MeS(1:3, :)$ 
21:   $M1\_updated \leftarrow M1\_current + MeS\_slice$ 
22:   $Propeller.M_1(\text{hub\_dof\_translation}, elm\_dof) \leftarrow M1\_updated$ 

23:  Compute the hub/rotating structure coupling matrix  $M_1$  for rotational dof
24:  Transform  $Mel$  with  $Te$  and add to  $M_1$ 
25:  Update  $M_1$  matrix:
26:   $M1\_current \leftarrow M_1(\text{hub\_dof\_rotation}, elm\_dof)$ 
27:   $MeS\_slice \leftarrow MeS(4:6, :)$ 
28:   $M1\_updated \leftarrow M1\_current + MeS\_slice$ 
29:   $M_1(\text{hub\_dof\_rotation}, elm\_dof) \leftarrow M1\_updated$ 
30:  Compute the rotating structure/hub coupling matrix  $M_2$  for translational dof
31:  Transform  $Mel$  with  $Te$  and add to  $M_2$ 
32:  Update  $M_2$  matrix:
33:   $M2\_current \leftarrow M_2(elm\_dof, \text{hub\_dof\_translation})$ 
34:   $MeS\_slice \leftarrow MeS(:, 1:3)$ 
35:   $M2\_updated \leftarrow M2\_current + MeS\_slice$ 
36:   $M_2(elm\_dof, \text{hub\_dof\_translation}) \leftarrow M2\_updated$ 
37:  Compute the rotating structure/hub coupling matrix  $M_2$  for rotational dof
38:  Transform  $Mel$  with  $Te$  and add to  $M_2$ 
39:  Update  $M_2$  matrix:
40:   $M2\_current \leftarrow M_2(elm\_dof, \text{hub\_dof\_rotation})$ 
41:   $MeS\_slice \leftarrow MeS(:, 4:6)$ 
42:   $M2\_updated \leftarrow M2\_current + MeS\_slice$ 
43:   $M_2(elm\_dof, \text{hub\_dof\_rotation}) \leftarrow M2\_updated$ 
44: end for

```

---

- [1] C. Reiche, A. P. Cohen, and C. Fernando, “An initial assessment of the potential weather barriers of urban air mobility,” *IEEE Transactions on Intelligent Transportation Systems*, vol. 22, no. 9, pp. 6018–6027, 2021.
- [2] McKinsey and Company, “Urban air mobility (uam) market study 2,” 2018.
- [3] G. Véronique, “L’État gagne son bras de fer contre la mairie de paris pour faire voler les premiers taxis volants dans la capitale,” *Le Figaro*, Jul 2024.
- [4] D. G. Mitchell, D. H. Klyde, M. Shubert, D. Sizoo, and R. Schaller, “Testing for certification of urban air mobility vehicles,” 12 2021.
- [5] ArcherIR, “Archer receives FAA certification to begin operating commercial airline.” <https://investors.archer.com/news/news-details/2024/Archer-Receives-FAA-Certification-to-Begin-Operating-Commercial-Airline/default.aspx>, Jul 2024. Online accessed August 1, 2024.
- [6] Archer, “Archer aviation midnight (production aircraft).” <https://evtol.news/archer/>, 2022. Online accessed February 26, 2024.
- [7] Airbus, “Cityairbus nextgen. fully-electric and integrated urban air mobility.” <https://www.airbus.com/en/newsroom/press-releases/2024-03-cityairbus-nextgen-makes-its-debut>, 2024. Online accessed March 8, 2024.
- [8] D. R. Vieira, D. Silva, and A. Bravo, “Electric vtol aircraft: the future of urban air mobility (background, advantages and challenges),” *International Journal of Sustainable Aviation*, vol. 5, no. 2, pp. 101–118, 2019.
- [9] A. Quintana, *Bifurcation Analysis and Characterization of Whirl Flutter in Rotor-Nacelle Systems*. PhD thesis, New Mexico State University, 2023.
- [10] J. Čečrdle, *Whirl flutter of turboprop aircraft structures*. Elsevier, 2023.
- [11] E. S. TAYLOR and K. A. BROWNE, “Vibration isolation of aircraft power plants,” *Journal of the Aeronautical Sciences*, vol. 6, pp. 43–49, 12 1938.
- [12] W. H. Reed III, “Propeller-rotor whirl flutter: A state-of-the-art review,” *Journal of Sound and Vibration*, vol. 4, no. 3, pp. 526–544, 1966.



## BIBLIOGRAPHY

- [13] B. T. F. Abbott, H. N. Kelly, and K. D. Hampton, “Nasa tn investigation of propeller-power-plant autoprecession boundaries for a dynamic-aeroelastic model of a four-engine turboprop transport airplane turboprop transport airplane\*,” 1960.
- [14] CFM, “Cfm rise whitepaper media.” [https://www.cfmaeroengines.com/wp-content/uploads/2021/07/CFM\\_RISE\\_Whitepaper\\_Media.pdf](https://www.cfmaeroengines.com/wp-content/uploads/2021/07/CFM_RISE_Whitepaper_Media.pdf), 2021. Online accessed March 18, 2024.
- [15] E. Commision, “Progress report 2023 climate action climate action,” 2023.
- [16] AIE, “World energy outlook 2020 summary,” 2020.
- [17] WindEurope, “Wind energy in europe,” 2022.
- [18] W. H. Reed, “A state-of-the-art rexiew. presented at the symposium on the noise and loading actions on helicopter v/stol aircraft and ground effect machines,” 9 1965.
- [19] J. C. HOUBOLT and W. H. REED, “Propeller-nacelle whirl flutter,” *Journal of the Aerospace Sciences*, vol. 29, pp. 333–346, 3 1962.
- [20] R. L. Bielawa, *Rotary wing structural dynamics and aeroelasticity*. American Institute of Aeronautics and Astronautics, 2006.
- [21] M. Gemmaretti, *Fundamentals of Aeroelasticity*. Springer, 2024.
- [22] D. Strong, R. Kolonay, L. Huttzell, and P. Flick, “Flutter analysis of wing configurations using pre-stressed frequencies and mode shapes,” in *46th AIAA/ASME/ASCE/AHS/ASC Structures, Structural Dynamics and Materials Conference*, p. 2173, 2005.
- [23] C. B. Hoover and J. Shen, “Whirl flutter analysis of a free-flying electric-driven propeller aircraft,” vol. 56, pp. 831–836, American Institute of Aeronautics and Astronautics Inc., 2019.
- [24] H. Yeo and A. R. Kreshock, “Whirl flutter investigation of hingeless proprotors,” *Journal of Aircraft*, vol. 57, pp. 586–596, 2020.
- [25] C. Koch, “Parametric whirl flutter study using different modelling approaches,” *CEAS Aeronautical Journal*, vol. 13, pp. 57–67, 1 2022.
- [26] R. M. Bennett and S. R. Bland, “Experimmental and analytical investigation of propeller whirl flutter of a power plant on a flexible wing,” 1964.
- [27] N. Böhnisch, C. Braun, S. Koschel, M. Vincenzo, and P. Marzocca, “Dynamic aeroelasticity of wings with distributed propulsion system featuring a large tip propeller,” in *International Forum on Aeroelasticity and Structural Dynamics, Madrid, Spain*, 2022.
- [28] N. Bohnisch, C. Braun, S. Koschel, and P. Marzocca, *A Building-Block Approach to Study Aeroelastic Instabilities for Unconventional Aircraft Configurations*. Engineers Australia, 2021.
- [29] C. Quanlong, H. Jinglong, and Y. Haiwei, “Effect of engine thrust on nonlinear flutter of wings,” *Journal of Vibroengineering*, vol. 15, no. 4, pp. 1731–1739, 2013.

- [30] G. P. Guruswamy, “Dynamic aeroelasticity of wings with tip propeller by using navier–stokes equations,” *AIAA Journal*, vol. 57, pp. 3200–3205, 2019.
- [31] H. S. Ribner, *Propellers in yaw*. National Advisory Committee for Aeronautics, 1943.
- [32] R. Zwaan and H. Bergh, “Restricted report, f.228,” 2 1962.
- [33] C. HAMMOND, H. RUNYAN, and J. MASON, “Application of unsteady lifting surface theory to propellers in forward flight,” American Institute of Aeronautics and Astronautics (AIAA), 4 1974.
- [34] J. P. Giesing, T. P. Kalman, and W. P. Rodden, “Subsonic steady and oscillatory aerodynamics for multiple interfering wings and bodies,” *Journal of Aircraft*, vol. 9, pp. 693–702, 1972.
- [35] R. Srivastava and T. Reddy, “Prop3d: A program for 3d euler unsteady aerodynamic and aeroelastic (flutter and forced response) analysis of propellers. version 1.0,” tech. rep., 1996.
- [36] R. J. Higgins and G. N. Barakos, “Whirl and stall flutter simulation using cfd,” 2017.
- [37] MSC Software Corporation, “Msc nastran.” Computer software, 2023.
- [38] A. Dugeai, Y. Mauffrey, and F. Sicot, “Aeroelastic capabilities of the elsa solver for rotating machines applications,” in *International Forum on Aeroelasticity and Structural Dynamics, Paris*, 2011.
- [39] Y. Zuo, J. Li, K. Feng, and Z. Jiang, “A 3-d finite element modeling method for time-varying rotor-support system based on rotating-fixed coordinates,” *Journal of Sound and Vibration*, vol. 568, p. 117977, 2024.
- [40] R. P. Coleman, “Theory of self-excited mechanical oscillations of hinged rotor blades,” tech. rep., 1943.
- [41] G. Bir, “Multi-blade coordinate transformation and its application to wind turbine analysis,” *46th AIAA Aerospace Sciences Meeting and Exhibit*, 1 2008.
- [42] P. F. Skjoldan, “Aeroelastic modal dynamics of wind turbines including anisotropic effects,” 2011.
- [43] G. Floquet, “Sur les équations différentielles linéaires à coefficients périodiques,” in *Annales scientifiques de l’École normale supérieure*, vol. 12, pp. 47–88, 1883.
- [44] A. H. Nayfeh and B. Balachandran, *Periodic Solutions*, pp. 147–172. 1995.
- [45] R. RIVA, “Analytical and numerical periodic stability analysis of wind turbines,” 2012.
- [46] C. L. Bottasso and S. Cacciola, “Model-independent periodic stability analysis of wind turbines,” *Wind Energy*, vol. 18, no. 5, pp. 865–887, 2015.
- [47] M. Géradin and D. J. Rixen, *Mechanical vibrations: theory and application to structural dynamics*. John Wiley & Sons, 2015.
- [48] H. M. Hilber, T. J. R. Hughes, and R. L. Taylor, “Improved numerical dissipation for time integration algorithms in structural dynamics,” 1977.

## BIBLIOGRAPHY

- [49] J. Chung and G. Hulbert, “A time integration algorithm for structural dynamics with improved numerical dissipation: The generalized alpha method,” *Journal of Applied Mechanics*, vol. 60, pp. 371–375, 6 1993.
- [50] V. Gufler, E. Wehrle, and R. Vidoni, “Sensitivity analysis of flexible multibody dynamics with generalized alpha time integration and baumgarte stabilization,” in *Advances in Italian Mechanism Science*, pp. 147–155, Springer International Publishing, 2022.
- [51] J. R. Dormand and P. J. Prince, “A family of embedded runge-kutta formulae,” *Journal of Computational and Applied Mathematics*, vol. 6, 1980.
- [52] O. A. Bauchau and J. I. Craig, “Euler-bernoulli beam theory,” 2009.
- [53] T. H. G. Megson, *Aircraft structures for engineering students*. Butterworth-Heinemann, 2016.
- [54] “The code aster: a product for mechanical engineers; le code aster: un produit pour les mecaniciens des structures.”
- [55] EDF, “Sslv104-poutre en rotation,” 12 2011.
- [56] MATLAB, “Version 23.2.0.2515942 (r2023b) update 7,” 2023.
- [57] I. ANSYS, “ANSYS Workbench,” 2023. Simulation Software.
- [58] H. A. H. Al-Khazali and M. R. Askari, “The experimental analysis of vibration monitoring in system rotor dynamic with validate results using simulation data,” *ISRN Mechanical Engineering*, vol. 2012, pp. 1–17, 6 2012.
- [59] M. Pastor, M. Binda, and T. Harčarik, “Modal assurance criterion,” in *Procedia Engineering*, vol. 48, pp. 543–548, Elsevier Ltd, 2012.
- [60] L. Meirovitch, *Leonard Meirovitch - Analytical Methods in Vibrations-Pearson (1967)*. MacMilan series in applied mechanics.
- [61] A. Vollar and L. Komzsik, *Computational techniques of rotor dynamics with the finite element method*. CRC press, 2012.
- [62] C. E. Hammond, L. Directorate, U. S. Army, A. Moblity, and R. Laboratory, “An application of floquet theory to prediction of mechanical instability,” *Journal of the American Helicopter Society*, vol. 19, pp. 14–23, 1973.
- [63] S. Tezиков, “Computational stability analysis of whirl flutter with application to civil urban mobility,” 2023.
- [64] J. A. I. da Silva, D. D. Bueno, and G. L. de Abreu, “On the controllers’ design to stabilize ground resonance helicopter,” *Journal of Vibration and Control*, vol. 25, pp. 2894–2909, 12 2019.
- [65] M. Goland, “The flutter of a uniform cantilever wing,” 1945.
- [66] A. Akpınar, “Structural and aeroelastic flutter analysis of wing store systems and structural modification approach in aeroelasticity a thesis submitted to the graduate school of natural and applied sciences of middle east technical university,” 2021.

- [67] T. Theodorsen, “General theory of aerodynamic instability and the mechanism of flutter,” tech. rep., 1979.
- [68] E. C. Yates Jr, “Calculation of flutter characteristics for finite-span swept or unswept wings at subsonic and supersonic speeds by a modified strip analysis,” tech. rep., 1958.
- [69] H. J. Hassig, “An approximate true damping solution of the flutter equation by determinant iteration,” *Journal of Aircraft*, vol. 8, pp. 885–889, 1971.
- [70] H. Güner, D. Thomas, G. Dimitriadis, and V. Terrapon, “Unsteady aerodynamic modeling methodology based on dynamic mode interpolation for transonic flutter calculations,” *Journal of Fluids and Structures*, vol. 84, pp. 218–232, 2019.
- [71] W. Rodden and T. Rose, “Propeller/nacelle whirl flutter addition to msc/nastran,” in *Proceedings of the 1989 MSC World User’s Conference*, 1989.
- [72] V. Q. L. Xu, “Propeller-wing whirl flutter an analytical study,” 7 2020.
- [73] S. Timoshenko, “Lxvi. on the correction for shear of the differential equation for transverse vibrations of prismatic bars,” *The London, Edinburgh, and Dublin Philosophical Magazine and Journal of Science*, vol. 41, no. 245, pp. 744–746, 1921.
- [74] R. R. Craig Jr and M. C. Bampton, “Coupling of substructures for dynamic analyses.,” *AIAA journal*, vol. 6, no. 7, pp. 1313–1319, 1968.
- [75] J. S. Przemieniecki, *Theory of Matrix Structural Analysis*, vol. 1. McGraw-Hill Book Compagny, 1968.